ICFO
Institut de Ciencies Fotoniques

A thesis submitted in partial fulfillment of the requirements
for the degree of Doctor

N-type bismuth sulfide colloidal nanocrystals and their application to solution-processed photovoltaic devices

Luis Martínez

This thesis has been submitted the August 21, 2014.
Under the supervision of Gerasimos Konstantatos

Photovoltaics has become a technology of increasing importance during the last decades as a platform to satisfy the energy needs of today without compromising future generations. Traditional silicon-based solar cells suffer from high material and fabrication costs. Alternative technologies such as organic photovoltaics offer promising low-cost material and processing advantages, however at the cost of chemical instability. Inorganic colloidal nanocrystals have attracted significant attention, due to the unique combination of chemical robustness, panchromatic solar harnessing and low-cost solution processability. However, the state-of-the-art nanocrystalline semiconductors raise some concerns regarding their suitability for industrial applications due to the presence of highly toxic heavy metals (such as lead or cadmium). Moreover, most of these materials are *p*-type, and are usually employed together with large bandgap *n*-type semiconductors that do not contribute to photocurrent generation. The field on non-toxic, electron-acceptor nanocrystalline semiconductors with appropriate energy levels, high optical absorption and bandgap suited to optimal solar harnessing still remains unexplored. The aim of this thesis is to investigate the potential of bismuth sulfide nanocrystals to be employed as environmental-friendly *n*-type nanomaterials for efficient solar harnessing.

Chapter 2 presents an in-depth physicochemical and optoelectronic characterization of bismuth sulfide colloidal nanocrystals. Bismuth sulfide nanocrystals are *n*-type semiconductors and have the appropriate bandgap and energy levels for efficient solar harnessing. Therefore, bismuth sulfide nanocrystals have the potential to be employed as the electron accepting material in heterojunction-based solar cells with most high-performing materials investigated for third-generation photovoltaics.

Bismuth sulfide nanocrystals are employed in Chapter 3 as electron accepting materials in hybrid organic-inorganic solar cells. Typical electron accepting materials and semiconducting polymers used in organic photovoltaics do not harness infrared radiation, thus limiting their solar harnessing potential. Bismuth sulfide nanocrystals can be used as electron accepting materials in hybrid organic-inorganic solar cells and extend the sensitivity range of P3HT-based solar cells into near-infrared wavelengths.

Chapter 4 investigates the nanomorphology and photovoltaic performance of hybrid solar cells based on bismuth sulfide nanocrystals and thiol-functionalized semiconducting polymers. This novel class of functionalized polymers binds to the surface of bismuth sulfide nanocrystals, thus preventing nanocrystal agglomeration, shows deeper ionization potential levels and exhibits improved electronic interaction within the organic-inorganic nanocomposite.

In Chapter 5, bismuth sulfide nanocrystals are employed together with lead sulfide quantum dots in *p*-*n* junction-based all-inorganic solution-processed photovoltaic devices. This system opens the possibility of fabricating all-inorganic

solution-processed bulk heterojunctions, a device architecture where requirements on carrier lifetime are eased. This way, a broader range of inorganic nanocrystalline materials can be explored in the quest for novel non-toxic third-generation photovoltaics.

Acknowledgements

This research project would not have been possible without the support of many people. First and foremost, I would like to express my gratitude to Professor Gerasimos Konstantatos, who gave me the freedom to pursue my own goals while at the same time provided the tuition to chase them. I would like to express him my very great appreciation for the guidance and support provided and also for the useful critiques of this research work.

Dr Maria Bernechea Navarro deserves my most sincere gratitude for the continuous chemistry lessons she provided me with as well as for introducing me to the world of colloidal chemistry. Also many thanks for the complete chemical studies on our nanomaterials and their optimization. Her work was a cornerstone that underpinned the development of this project.

Dr Alexandros Stavrinadis is gratefully acknowledged for providing the baseline nanocrystal material for the realization of the present work.

I am highly indebted to Dr Arup Kumar Rath for his active support in photovoltaic device fabrication and characterization techniques. The limits of nanocrystalline solar cell performance are now a bit closer because of your work.

Dr Silke Diedenhofen provided me with very valuable advice about the present work and about science itself. I am particularly thankful for the rigorous methodology she employs in scientific text revision. Her outstanding ability to perform FIB measurements has been fundamental for unveiling the mysteries of nanomorphology in solar cells based on nanocrystalline materials.

I would like to thank Dr Fiona Jean Beck and David So for reviewing and correcting this thesis in such a timed manner and also for fruitful discussions, both about scientific behaviour and writing style.

Francisco Pelayo Garcia de Arquer deserves my gratitude for providing optical modelling of the structures employed and for the amazing 3D pictures.

I am particularly grateful for the assistance given by Dr Agustin Mihi in the countless hours spent developing low-cost nanofabrication methods. Our experiments have not been as successful as we both would have liked to, but they were big fun.

Professor Keisuke Tajima and Sosuke Higuchi are also greatly acknowledged for providing cutting-edge polymers employed in this work and for providing a different perspective for the analysis of the results. I also would like to express my gratitude for their kind advices about Japan. I hope I'll be able to pay you back one day.

I would also like to thank my colleagues at the Emerging Functional Polymers

group at Riken and the Hashimoto Lab at University of Tokyo, for their teachings about semiconducting polymers and for letting me share their progress and their facilities. My sincerest gratitude to Akaike-hakase, Inori-san, Izawa-san, Zhou-san, Cong-san, Zhong-san, Ma-san, Ethan and Mitsuzawa-san for the amazing time I could share with all of you.

The patience of Domink Kufer is also greatly appreciated. I know our office has not been as quiet as he would have liked to.

All of the Solution-Processed Nanophotonic Devices group are gratefully acknowledged for creating the best-possible research environment. Xiaojie, Tania, Nicky, Yiming, Olga, Guillem, Ariana... thank you for making this possible.

The members (both from scientific and management units) of the Institute of Photonic Sciences deserve my very great appreciation in making such a pleasant working atmosphere. I cannot list all of you here although I would to emphasize my thankfulness to Luis, Javi, Magda, Xavi, Luis and Carlos.

Although this work has not involved much clean-room work, I cannot forget the countless hours of big fun I have shared in ICFO's cleanroom. Davide, Sarah, Johann, Jan, Olga, Stephanie, Danny, Anne... you are all responsible for such awesome experiences. Thanks.

I would like to acknowledge the people that contributed significantly to my reenlisting into acting. Daan, Mariale, Candan, Fabian and Mark, I just wanted to tell you that I finally got a paper! I couldn't think of a better way to spend the weekends at work than the way we did it together.

Many, many thanks to my siblings Nuria and Xavi for being a perfect model to imitate. The biggest of all kisses and hugs.

Per acabar, voldria agraïr als meus pares Olga i Gregorio, pel seu suport durant tants anys. Sé que a vegades pot ser difícil entendre els extranys motius que poden portar a un fill a fer un doctorat, però vosaltres no només els heu entès, sinó que els heu recolzat. Cantava Serrat:

> A menudo los hijos se nos parecen, así nos dan la primera satisfacción

Jo només voldria assemblar-me més a vosaltres.

Finally, I cannot find thankful enough words to express my most profound gratitude to Vanessa Lostal. You not only shared my journey here but also shone the light I needed to see the path under my feet in the darkest moments of this PhD. It is only because of you that I could find the courage to pursue this work.

Contents

Chapter 1

Introduction

The Sun is the largest source of energy available in our Solar System, irradiating an average power density of 20 GW/(m^2 sr) to the Earth surface. The amount of solar energy reaching the surface of the Earth in one year is about twice as much as the energy that will ever be obtained from coal, oil, natural gas, and mined uranium combined [1]. Highly efficient and cost-competitive ways to harvest the incoming solar radiation are therefore of interest. Low-cost, efficient solar harnessing schemes could become part of the solution for a fifth of the world population that, as stated by the United Nations Industrial Development Organization, still has no access to electricity [2]. Therefore, cost-effective and highly efficient solar harnessing platforms are not only interesting for researchers, but also for governments whose economies are strongly bound to the oil market.

Ever since the discovery of the photovoltaic effect in 1839 by Alexandre-Edmond Becquerel, power conversion efficiencies of laboratory-scale photovoltaic devices have steadily increased, reaching close to their theoretical maximum as a result of decades of intensive research. Nowadays, highly efficient solar cells are routinely being incorporated in almost all space applications, where cost is not a major issue [3]. However, for large-scale terrestrial applications, there are several criteria that could ease off deployment constraints of photovoltaics [4]:

- A production cost per Watt lower than $0.4\$/W$ to minimize the capital investment and payback time[1].
- Power conversion efficiencies (PCE) larger than or on the order of 10%.

[1] The estimated time the photovoltaic module should be operated to balance its fabrication and installation cost.

- Environmental-friendly semiconductors that comply with the regulatory framework.
- Stable performance over a period of time larger than the payback time.

A technological platform that satisfies all of the aforementioned conditions at the same time has yet to be demonstrated. The works on third generation solar cells aim tackling these challenges.

1.1 Introduction to solar cells

A solar cell is an optoelectronic transducer that converts incoming optical radiation into electrical energy. If the energy of the light is sufficiently high compared to the semiconductor bandgap (E_g), it results in the promotion of an electron from the valence band to the conduction band, thus leaving a hole (absence of an electron) in the valence band. These electrons and holes are originally bound carriers (excitons). The exciton is bound with a certain binding energy within a certain distance, i.e. the exciton Bohr radius (r_B). Beyond the exciton Bohr radius, which is characteristic of a given material, they no longer sense the presence of each other. In traditional inorganic semiconductors, with crystal sizes much larger than the exciton Bohr radius and large dielectric constants, a minor energy input such as thermal energy is sufficient to exceed the exciton binding energy, splitting it into free carriers. In contrast, the exciton binding energy in organic semiconductors can be as high as 1.4 eV as a result of their lower dielectric constants [5]. In such cases, thermal energy is insufficient to dissociate the excitons and alternative exciton dissociation mechanisms have to be employed [6]. Upon splitting of the exciton into free carriers, these are physically separated by a built-in field (V_{bi}), bringing the photogenerated electrons toward the n-side (electron acceptor) and photogenerated holes towards the p-side (electron donor). The collecting electrodes situated at the end of those regions extract the carriers from the semiconductor and inject them into an external electrical circuit. All these processes (charge separation, transport, collection and injection into an external circuit) have to take place before the charges undergo undesired recombination.

1.1.1 Solar cell characterization

The photogenerated and collected carriers are extracted to an external electrical circuit, giving rise to an electrical current and delivering power to the external load. A solar cell is an active element, therefore it has to provide both current

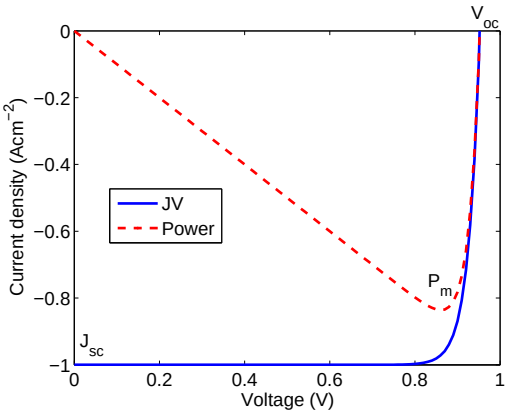

Figure 1.1: Characterization of a solar cell. The current-voltage curves reveal the fundamental parameters for solar cell characterization (J_{sc}, V_{oc} and P_m).

and voltage at the same time. The highest current that the solar cell can provide is the short-circuit current (I_{sc}) (or short-circuit current density (J_{sc}) expressed in mAcm^{-2}, when I_{sc} is normalized to the device active area) and corresponds to the situation where both terminals of the solar cell are connected through an ideal non-resistive wire. On the other hand, when the two terminals are isolated from each other (i.e. open-circuit conditions), the solar cell is delivering the maximum voltage at its terminals, known as the open-circuit voltage (V_{oc}). Therefore, varying the load connected to the solar cell's terminals, the current-voltage characteristics of the solar cell can be obtained (Figure 1.1).

The maximum power point (P_m) is defined as the point where the solar cell is delivering the maximum power density to the external circuit. The delivered electrical power density is defined as:

$$P = VJ \tag{1.1}$$

The maximum power point is reached at a given voltage (V_m) and current density (J_m). The fill factor (FF) is then defined as the ratio between the maximum power that the solar cell can deliver (maximum power point) and the maximum power that it could deliver under ideal lossless conditions, according to the formula:

$$FF = \frac{P_m}{J_{sc}V_{oc}} = \frac{J_m V_m}{J_{sc}V_{oc}} \tag{1.2}$$

These three parameters (J_{sc}, V_{oc} and FF) are the basis for calculating the main figure of merit in solar cell characterization, the power conversion efficiency

(PCE or η). PCE gives information on how much electrical power the solar cell can deliver for a given optical power density (P_i):

$$\eta = \frac{J_m V_m}{P_i} = \frac{J_{sc} V_{oc} FF}{\int_{-\infty}^{+\infty} P_i(\lambda)\, d\lambda} \tag{1.3}$$

While the power conversion efficiency provides information on the total sunlight-to-electricity conversion, it is sometimes interesting to monitor the photon-to-electron conversion efficiency at a given wavelength. Wavelength-dependent phenomena such as reflection, light trapping or interference (since some solar cells are double-pass elements) can be studied using monochromatic techniques. The External Quantum Efficiency (EQE) provides information on how many of the incoming photons are converted into electrons and extracted under short-circuit conditions, according to the expression:

$$EQE(\lambda) = \frac{hc}{q\lambda} \frac{J(\lambda) - J_d}{P_i(\lambda)} \tag{1.4}$$

where h, c and q are the Planck's constant, speed of light in vacuum and elementary charge, respectively; λ is the wavelength, $J(\lambda)$ is the short-circuit current density at that wavelength and J_d is the current density in dark conditions.

If we take into account the absorbed photons ($A(\lambda)$), we define the Internal Quantum Efficiency (IQE), given by the equation:

$$IQE(\lambda) = \frac{EQE(\lambda)}{A(\lambda)} = \frac{EQE(\lambda)}{1 - R(\lambda) - T(\lambda)} \tag{1.5}$$

where $R(\lambda)$ and $T(\lambda)$ stand for the sample's reflection and transmission, respectively.

Monitoring the monochromatic quantum efficiencies also allows for an estimation of the short-circuit current density under solar power densities (P_{sun}), since in an ideal solar cell [7]:

$$J_{sc} = \frac{hc}{q} \int_{-\infty}^{+\infty} \frac{EQE(\lambda) P_{sun}(\lambda)}{\lambda}\, d\lambda \tag{1.6}$$

1.2 Harvesting the Solar Energy

The bandgaps of the semiconductors employed to efficiently harness solar energy semiconductors have to be carefully chosen in order to provide for the highest

possible power conversion efficiency. The various types of materials and device architectures that have been studied for solar harnessing is simply too broad to cover in detail (Fig. 1.2). For this purpose, the reader is referred to the periodic review works performed by M.A. Green [8]. Herein, however, we will very briefly discuss silicon solar cell technology, and some of the key alternative technologies for third-generation photovoltaics.

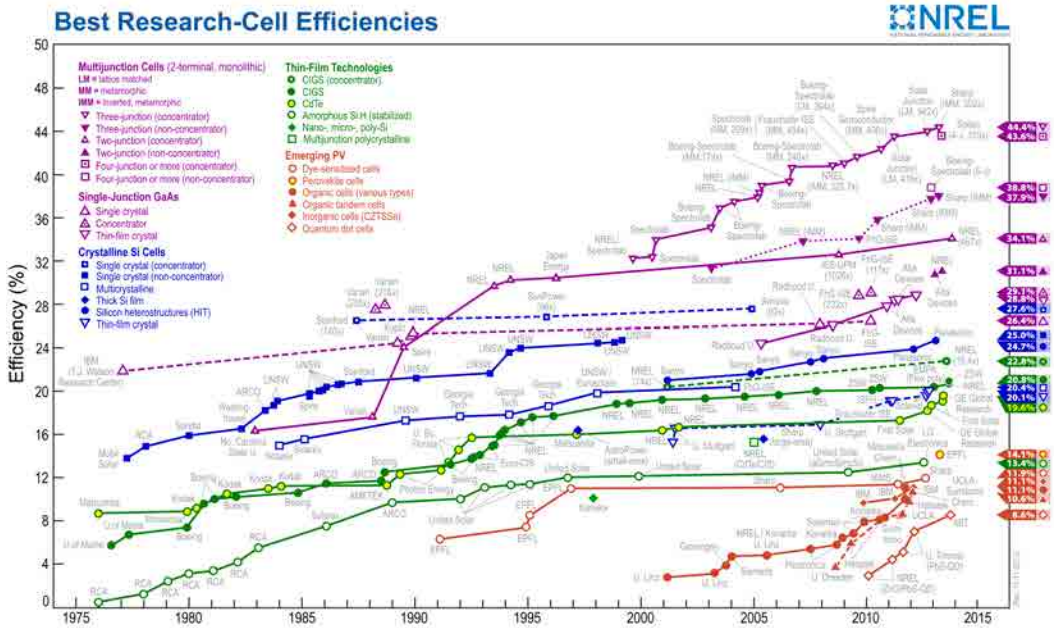

Figure 1.2: Evolution of the efficiency of different types of solar cells, reproduced with permission of [9].

1.2.1 Crystalline silicon

Since Chapin et al. reported a 6 % power conversion efficiency in a *p-n* silicon junction in 1954 [10], silicon has been the primary material employed in photovoltaics. Nowadays, silicon-based photovoltaic modules are commercially available and their power conversion efficiencies in laboratory solar cells can reach or exceed the 24 % level. However, the implementation of crystalline silicon photovoltaic systems is still moderate, due to the following reasons:

- While silicon is the second most abundant element in the earth's crust [11], it primarily appears as silicon dioxide (silica or SiO_2). The process involved in processing silicon dioxide into high purity crystalline silicon is far from cheap and requires large energy inputs [12].
- Silicon has been the primary material for the electronics industry, which has further restricted the availability of silicon for the photovoltaic market.
- Silicon is an indirect bandgap semiconductor, which implies lower absorption coefficients compared to its direct bandgap counterparts. Consequently, silicon-based solar cells' require a larger amount of material to efficiently absorb the incident radiation, with the subsequent cost increase [13].
- The fabrication processes typically associated with silicon technologies are based on high-vacuum techniques and high temperature processes, which are more expensive than roll-to-roll techniques and not compatible with light weight flexible substrates [6, 14].

Organic photovoltaics and solar cells based on colloidal nanoparticles are new technological platforms aiming at overcoming some of the aforementioned drawbacks of silicon photovoltaics [15].

1.2.2 Organic solar cells

In view of the high cost associated with high purity inorganic crystalline bulk semiconductors, a novel class of materials has been introduced, based on organics: semiconducting conjugated polymers and small molecules. High-quality conjugated polymers are solution-processable and compatible with large scale manufacturing processing techniques such as roll-to-roll [16].

Polymer-based solar cells have seen tremendous progress in the last decade and efficiencies in the order of $\sim$ 8% are now routinely reported [17]. This is a result of a joint effort to develop new conjugated semiconducting polymers, to

tailor their optoelectronic properties and to carefully control the device fabrication conditions. Despite the remarkable progress achieved in organic solar cell technology, there are several challenges that are still to be tackled:

- The bandgaps of most conjugated polymers (donor) and fullerene derivatives (acceptor) are typically $\sim 1.7 - 2$ eV. This implies that a significant proportion of the solar spectrum is left unharnessed. Novel low bandgap polymers and novel device architectures (i.e. tandem cells) are under investigation to overcome this limitation [18].
- Exciton diffusion length in most conjugated polymers is only ≈ 10 nm. Accordingly, an accurate control over the nanomorphology of the photovoltaic devices that ensures the presence of neighbouring dissociating interfaces within the exciton diffusion length is required [14].
- Carrier mobilities are usually low in conjugated polymers compared to inorganic semiconductors. This imposes an upper limit upon the active layer thickness, which limits the light absorption and thus the generated current [19].
- Exposure to ultraviolet light, air and moisture degrades the performance of the organics, thus requiring encapsulation [20].

Solution-processed inorganic photovoltaics have been recently developed, which aim at combining the benefits of the chemical robustness and solar harnessing potential of inorganic semiconductors and the solution processability of conjugated semiconducting polymers. In the following section we will introduce solution-processed colloidal nanocrystals, a particular type of which will be the central topic of this thesis.

1.2.3 Colloidal nanocrystals and quantum dots

Inorganic nanocrystals (NCs) are tiny pieces of highly crystalline inorganic semiconductors, with sizes ranging from few to tens of nanometers. Some nanocrystal materials can be synthesized via a colloidal approach, i.e. dispersed evenly throughout a solvent. Colloidal synthesis of nanoparticles allows for accurate control over composition, size and shape of the highly crystalline nanoparticles. Nanospheres, nanobelts, nanorods or tetrapods can be obtained using colloidal synthesis [21]. Solution-processing of nanomaterials allows for the incorporation of this technology into roll-to-roll fabrication processes which aim to reduce photovoltaic module manufacturing costs. The incorporation of these nanomaterials onto flexible and light-weight substrates is also within reach due to their low-temperature processing [15].

Quantum dots (QDs) are a particular type of nanocrystals, with dimensions comparable to or smaller than their exciton Bohr radius. Beyond the Bohr radius, both electron and hole, no longer sense the presence of each other, thus becoming free carriers. In quantum dots, the exciton remains confined inside the nanoparticle, leading to interesting quantum confined phenomena, such as bandgap tunability via modification of the quantum dot size. The energy levels of the material can no longer be regarded as continuous, but have to be considered as discrete levels, with some broadening due to the QD size distribution.

Regardless of the size regime of the nanoparticles (NCs or QDs), they share the same steps in their colloidal synthesis, namely: nucleation, growth, isolation, redispersion and post-treatments. In the method employed in this thesis, their syntheses are performed using a Schlenk line under an inert argon atmosphere. Size control is typically achieved through temperature variation or performed by quenching the growth of the nuclei by incorporation of a precipitating agent like methanol or cooling of the solution. To prevent NC agglomeration and subsequent precipitation from solution, the nanoparticles are capped using long organic molecules (ligands). The ligands form a protective cover for the NCs against binding to other NCs or oxygen, thus stabilizing the NCs in solution. However, the original capping ligands are usually non-conductive and far too long for charges to hop or tunnel through. In order to extract the photogenerated carriers in the NCs, the capping molecules must be removed or replaced by shorter ones. There are two main ways to exchange the ligands (the so-called ligand exchange process): in solution and in solid state. The former involves adding the new ligands to the colloidal solution and leaving the mixture to react under specific conditions of temperature, moisture and time. Finally, the ligand-exchanged NCs are spincoated onto the substrate. However, during solution-based ligand exchange, some nanocrystals might be temporally exposed to adjacent NCs, agglomerating and finally precipitating. Contrarily, the solid-state ligand exchange method takes place once the colloidal solution has been deposited onto a substrate. First, the colloidal solution is dropped onto a substrate. Then, several drops of the new ligand are dispensed. Next, the film is flushed with the ligand solvent to remove the unreacted ligands and finally, the NCs solvent is also dispensed to remove the unexchanged nanoparticles. This is the most commonly used method for growing solution-processed inorganic nanocrystalline solids (the so-called layer-by-layer method or LBL), since the exchanged particles are no longer soluble in their original solvent. Accurate control over the film thickness can be achieved via repetition of the LBL process [22].

Table 1.1: Restriction of Hazardous Substances limits.

Material	Trace
Cadmium	100 ppm
Lead	1000 ppm
Mercury	1000 ppm

Toxicity of nanocrystals

Toxicity of nanomaterials is a matter of debate within the scientific and regulatory communities. To date, there is no clear understanding of the threat posed by nanomaterials to human health. At the moment, a case-by-case study is advised by the European Commission as stated in the second regulatory review on nanomaterials [23]. There is however, a regulatory framework adopted by the members of the European Union which restricts the use of some hazardous elements in electronic and electrical devices, known as the Restriction of Hazardous Substances (RoHS) [24]. This directive limits the amount of lead, mercury and cadmium[2], among other materials, that can be found in any electronic and electrical device. The permitted traces for the aforementioned materials are summarized in Table 1.1.

Unfortunately, the record-holding solution-processed inorganic materials heavily rely on lead or cadmium derivatives. The limitation in the use of lead and cadmium by the RoHS is a clear obstacle for the industrial deployment of these materials. For this reason, it is of increasing importance to investigate alternative, more environmentally friendly, solution-processed nanomaterials for solar harnessing applications.

Solar cells from colloidal nanocrystals - State-of-the-art

Different platforms have been employed for fabricating solar cells based on colloidal nanocrystals and quantum dots, both from the device architecture (Schottky, bilayer and bulk heterojunction) and the material points of view. The field of solar cells based on colloidal nanoparticles is broad and rapidly progressing, with new publications appearing on a weekly basis. A detailed analysis of the progress in colloidal nanocrystal synthesis and solar cell device fabrication is beyond the scope of this thesis, as it would require an in-depth study of the different material systems, their associated limitations and the possible routes to overcome them. The reader is instead referred to recent reviews on the field of solar cells based on colloidal nanoparticles for a complete understanding of the

[2]There is a granted exception for cadmium telluride detectors.

Table 1.2: Summary of the Schottky solar cells.

Material	$V_{oc}(V)$	$J_{sc}(mAcm^{-2})$	FF (%)	$\eta(\%)$
PbS [29]	0.51	14.0	51	3.6
PbSe [30]	0.24	21.4	40	2.1
PbS_xSe_{1-x} [31]	0.45	14.8	50	3.3

Table 1.3: Summary of the bilayer devices.

Material	$V_{oc}(V)$	$J_{sc}(mAcm^{-2})$	FF (%)	$\eta(\%)$
PbS/TiO_2 [32]	0.51	16.2	58	5.1
PbS/aSi [33]	0.2	4.13	39	0.9
$CuS_2/CdSe$ [34]	0.6	5.63	47	0.4
CdTe/CdSe [35]	0.45	13.2	49	2.9
Cu_2ZnSnS_4/CdS [36]	0.321	1.95	37	0.23
$HgTe/TiO_2$ [37]	0.35	0.8	60	0.168
P3HT/PbS [38]	0.35	0.3	35	0.04
PbS/C_{60} [39]	0.22	0.24	29	0.0151
HgTe-P3HT/TiO_2 [37]	0.4	1.4	36	0.2

evolution of the power conversion efficiency in these systems [25–27]. We will focus on strategies where the nanoparticles are directly used as nanocrystalline solids, thus benefiting from their low-temperature solution processability.

Solution-processed Schottky junction-based photovoltaic devices have been reported employing lead-based colloidal quantum dots, as shown in Table 1.2. The presence of trap states in the material's bandgap cause Fermi level pinning, which complicates the formation of a Schottky barrier between some colloidal nanoparticles and metals [28]. Also, most of the nanocrystalline semiconductors exhibit low carrier mobilities and short carrier lifetimes, thus limiting their solar harnessing potential.

Bilayer heterojunction solar cells have been fabricated from different colloidal nanoparticle materials. This is partly due to the aforementioned limitations of the Schottky junction but also because the bilayer platform allows for hybrid organic-inorganic solar cells, due to the simple device fabrication process. Table 1.3 presents a summary of the reported planar heterojunctions where at least one of the two layers is based on a film of colloidal nanocrystals or quantum dots.

The bulk heterojunction approach has been widely explored by the organic

Table 1.4: Summary of the reported bulk heterojunction devices.

Material	$V_{oc}(V)$	$J_{sc}(mAcm^{-2})$	FF (%)	$\eta(\%)$
PbS-MEHPPV [41]	0.36	0.01[3]		
PbSe-P3HT [42]	0.35	1.08	37	0.14
OC_1C_{10}PPV-CdSe [43]	0.65	7.3	35	1.8
MEHPPV-CdS [44]	0.85	2.96	47	1.17
MDMO-PPV-ZnO [45]	0.814	2.4	59	1.6
P3HT-ZnO [46]	0.75	5.2	52	2.0
P3HT-TiO_2 [47]	0.78	4.33	65	2.20
PbS-PDTQx [48]	0.38	4.2	34	0.55
P3HT-FeS_2 [49]	0.44	0.85	42	0.16

Table 1.5: Summary of the reported ordered bulk heterojunction devices employing colloidal quantum dots or nanocrystals

Material	$V_{oc}(V)$	$J_{sc}(mAcm^{-2})$	FF (%)	$\eta(\%)$
ZnO nanowires-Cu_2O [52]	0.15	1.43	25	0.053

photovoltaic community as a method to overcome the short exciton diffusion length of most semiconducting polymers [6]. It was also the first technological platform employed to demonstrate colloidal quantum dots of CdSe as electron transporting materials in hybrid organic-inorganic solar cells [40]. Table 1.4 presents a summary of the reported bulk heterojunctions employing colloidal nanocrystals or quantum dots.

Traditional fabrication techniques for solution-processed solar cells yield randomly distributed phases in the active layer. Although ordered heterostructures are more complicated to fabricate than disordered blends, they have significant potential. First, all carriers can be photogenerated close to (within the material's diffusion length) a neighbouring dissociating interface. Also, continuous percolation pathways to the collecting electrodes can be guaranteed. Finally, ordered structures are easier to simulate and model [50]. At the same time, prescribed morphologies can allow for tailored optical light trapping schemes [51]. Table 1.5 presents the figures of merit of a photovoltaic device based on ZnO nanowires and cuprous oxide colloidal nanocrystals.

Among the different possible solar cells based on colloidal nanoparticles reported, we observe that the highest power conversion efficiencies have been obtained using toxic heavy metals such as cadmium and lead. Contrarily, alterna-

[3]Incident power 207mW.

tive environmental-friendly materials have attained more modest power conversion efficiencies. Also, cadmium derivatives and large bandgap semiconductors have been main *n*-type electron accepting materials employed in all-inorganic heterojunctions and hybrid organic-inorganic solar cells. Large bandgap semiconductors do not contribute to the photocurrent generation and are only used as electron transporting materials. As an alternative, we proposed bismuth sulfide nanocrystals as an abundant, environmental-friendly and electron-rich nanocrystalline material [11].

1.3 Thesis objectives

Colloidal nanocrystals hold great promise as a material for third-generation photovoltaics. In particular, *n*-type environmentally-friendly materials with appropriate bandgap for solar harnessing that can be processed in solution, using low-temperature techniques, can pave the way for new device concepts and architectures. This thesis explores the potential of bismuth sulfide colloidal nanocrystals as a novel photoactive solar cell material. The objectives of this thesis are:

- To develop and characterize a solution-processable *n*-type electron acceptor nanomaterial with optimal bandgap for solar harnessing based on environmentally friendly elements.
- To develop a hybrid polymer-nanocrystal solar cell using non-toxic highly absorbing inorganic nanocrystals as electron acceptor.
- To demonstrate a solution-processed all-inorganic solar cell based on *n*-type metal chalcogenide nanocrystals, employing low temperature fabrication techniques and in which the *n*-type material contributes in solar harnessing.

1.4 Thesis outline

The remainder of this thesis is organized as follows:

- Chapter 2 presents a detailed physicochemical and optoelectronic characterization of bismuth sulfide colloidal nanocrystals. This chapter investigates the suitability of this novel nanomaterial as a solar harnessing element and identifies the advantages and limitations of this technology.

- Chapter 3 demonstrates non-toxic hybrid organic-inorganic solar cell devices based on bismuth sulfide nanocrystals and the state-of-the-art semiconducting polymer, P3HT (poly(3-hexylthiophene). We show that bismuth sulfide nanocrystals not only form a photovoltaic junction with P3HT but also actively contribute to the photocurrent generation. We demonstrate that the P3HT-Bi_2S_3 junction is a highly efficient charge dissociation interface and develop bilayer and bulk heterojunction device architectures. We thus show the potential of this hybrid organic-inorganic platform to overcome some of the limitations of the materials currently employed by the organic photovoltaic community.

- Chapter 4 addresses the incorporation of bismuth sulfide nanocrystals into new organic polymers with chemical modifications to overcome some of the limitations identified in Chapter 3. These novel functionalized polymers ensure a better electronic interaction between the organic-inorganic nanocomposite and more appropriate structural and optoelectronic properties for solar harnessing. These hybrid organic-inorganic systems give rise to new physical processes.

- Chapter 5 demonstrates all-inorganic solar cell devices based on bismuth sulfide nanocrystals and lead sulfide colloidal quantum dots. We show that Bi_2S_3 serves a dual role in creating a built-in potential and contributing to the carrier photogeneration. We also present a novel device architecture for solar harnessing that has been possible due to the advent of *n*-type bismuth sulfide colloidal nanocrystals. This new architecture can be easily implemented by mixing different semiconductor nanocrystals in solution. It can allow the use of nanocrystalline materials with shorter carrier lifetimes, thus broadening the range of candidate materials for third generation photovoltaics.

Chapter 2

$n-$type bismuth sulfide nanocrystals

Despite the several reports of environmentally benign p-type electron donor nanocrystal materials (such as cuprous oxide, copper sulfide and copper zinc tin sulfide and QDs such as silicon) the scarcity of reports on non-toxic $n-$type electron acceptor nanocrystals opens a new window of opportunity for their development. Besides wide bandgap metal oxides (i.e. titania or zinc oxide) that do not contribute to absorption, cadmium-based quantum dots have been the mainly reported n-type materials in solar cell devices. It is therefore important to identify alternative nanocrystalline semiconductors with n-type behaviour, appropriate (≈ 1.3 eV) bandgap for solar harnessing and minor associated toxicity issues. These materials can be employed as electron acceptors in hybrid polymer nanocrystal solar cells, as well as in solution-processed inorganic solar cells.

Bismuth(III) sulfide (Bi_2S_3) is an interesting semiconductor for photovoltaic devices because of its direct band gap of 1.3 eV [53]. Colloidal Bi_2S_3 nanoparticles were first successfully synthesized by Riley et al [54], thus providing a new route to employ this material as a low-cost solar cell active medium, where both high purity and crystallinity, as well as size and shape control, could be achieved. Despite the theoretical suitability of Bi_2S_3 NCs for solar harnessing, very little information can be found in literature about the optoelectronic properties of this semiconductor. Few reports have been published where bismuth sulfide nanocrystals have been incorporated onto optoelectronic devices, such as electrochemical solar cells [55] and photodetectors [56]. Most importantly, photovoltaic devices based on bismuth sulfide colloidal nanocrystals have not been reported hitherto.

2.1 Chemistry of bismuth sulfide NCs

2.1.1 Synthesis of colloidal bismuth sulfide NCs

The synthesis of colloidal Bi_2S_3 nanoparticles was performed using a modification of a previously reported procedure [56]. Briefly, 5.4 mmol of bismuth acetate $(Bi(OAc))_3$, 34 mmol of oleic acid (OA) and 34 mmol of 1-octadecene (ODE) were pumped overnight at 100°C. After this time, the reaction temperature was raised to 170°C. When the reaction flask reaches this temperature 1.2 mmol of Hexamethyldisilathiane (HMS) mixed with 10 mL of ODE were quickly injected to the flask and the heating temperature was lowered to 100°C. After 2 h at 100°C the reaction was quenched by removing the heating mantle and adding 20 mL of cold toluene and 40 mL of cold methanol (MeOH). The oleate caped Bi_2S_3 nanoparticles were isolated after centrifugation. Purification of the nanoparticles was performed by successive dispersion and precipitation in toluene and MeOH, respectively. Finally, the nanoparticles were dispersed in the desired solvent, usually chloroform or toluene [57].

2.1.2 Structural properties of bismuth sulfide NCs

Transmission electron microscopy (TEM) studies were performed to investigate the physical dimensions and the crystallinity of the synthesized colloidal Bi_2S_3 nanoparticles. The TEM picture presented in Figure 2.1 shows the typical rod-shape structure of Bi_2S_3 NCs. These micrographs confirm the crystallinity of the NCs, as evidenced by the lattice planes. We measured the length and the width of 45 randomly selected nanoparticles in several micrographs, revealing an average length of the rods of 17.8 ± 2.4 nm and the average width of 10.4 ± 1.8 nm (Figure 2.2).

X-Ray Diffraction (XRD) measurements were carried out to determine the crystalline structure of the colloidal Bi_2S_3 nanoparticles. We observe a good agreement between the XRD measurements and the JCPDS card number 00-006-0333 Bi_2S_3 orthorhombic model (Fig. 2.3).

Semiquantitative analysis of the energy-dispersive X-ray spectrum (EDX) of the Bi_2S_3 NCs indicates a bismuth rich stoichiometry with a measured Bi:S atomic ratio of 0.943 : 1. The excess of bismuth is expected due to the excess of bismuth precursor used in the reaction. This is a common approach for synthesizing colloidal nanocrystals intended for solar cell fabrication, since a metal rich NC surface allows for increased ligand passivation and hence colloidal stability [58, 59].

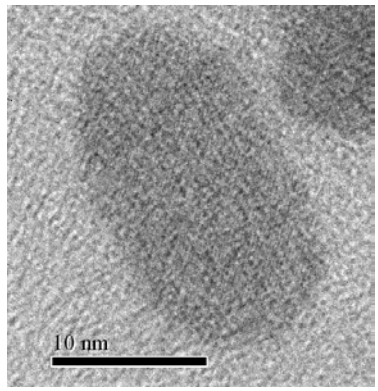

Figure 2.1: Transmission electron microscopy image of Bi_2S_3 NCs. The nanoparticles have a rod-like shape and are crystalline, as evidenced by the lattice planes.

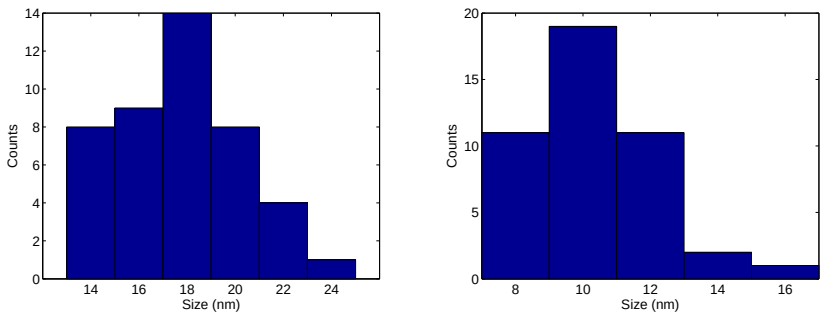

(a) (b)

Figure 2.2: Size distribution of the Bi_2S_3 NCs. The average length of the rods (a) is 17.8 ± 2.4 nm and the average width (b) is 10.4 ± 1.8 nm.

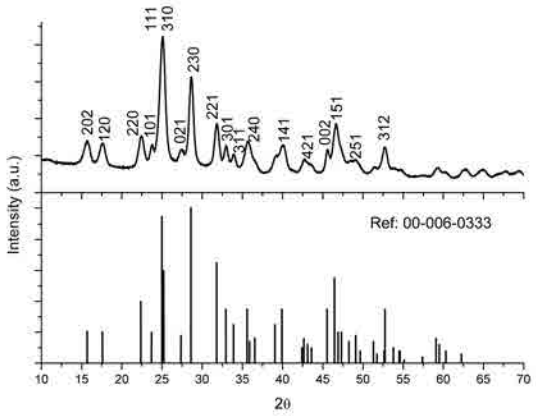

Figure 2.3: X-Ray diffraction measurements of Bi_2S_3 NCs and comparison with the JCPDS card number 00-006-0333 Bi_2S_3 orthorhombic model.

2.2 Optoelectronic properties of bismuth sulfide NCs

A semiconductor must fulfil a number of optical and electrical requisites to be considered a promising candidate for solar harnessing applications. We therefore investigated the optoelectronic properties of the synthesized colloidal Bi_2S_3 nanoparticles.

2.2.1 Optical properties of bismuth sulfide NCs

The optimum bandgap for single junction solar cells is in the $1.1 - 1.3$ eV range. Figure 2.4(a) shows the absorbance in toluene solution of the Bi_2S_3 NCs. We observe an absorbance onset at $\approx$ 950 nm and no apparent free-carrier absorption at NIR wavelengths. To calculate the absorption coefficient of bismuth sulfide (Figure 2.4(b)) we first measured the total reflection and transmission of a film of known thickness (d) using an integrating sphere to account both for specular and diffuse components. We then calculated the total absorption ($A(\lambda)$) and finally, the material absorption coefficient ($\alpha(\lambda)$) was obtained as:

$$\alpha(\lambda) = \frac{-\ln\left(1 - A(\lambda)\right)}{d} \tag{2.1}$$

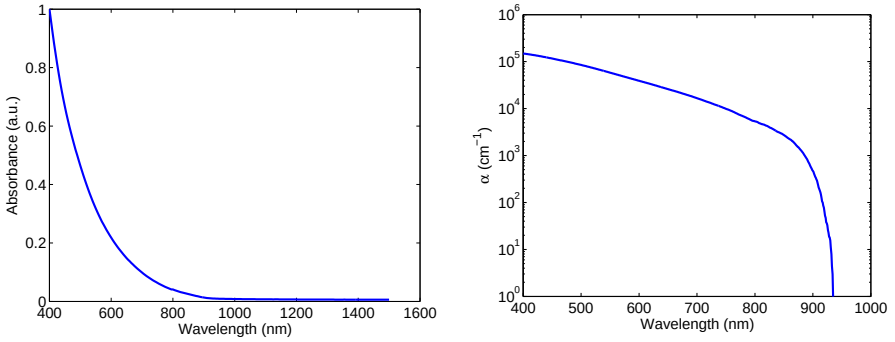

(a) (b)

Figure 2.4: Optical absorption of Bi_2S_3 NCs. (a) Absorbance in solution. (b) Absorption coefficient of Bi_2S_3.

Bi_2S_3 NCs demonstrate an absorption onset at 950 nm (1.3 eV) and high optical absorption coefficient ($10^4 - 10^5$ cm^{-1}), thus fulfilling the ideal optical requisites for solar harnessing. Moreover, it is worth noting that we do not observe any quantum confinement features in the absorption profile, which indicates that the Bohr radius of bismuth sulfide nanoparticles is smaller than their physical dimensions. Henceforth, the bismuth sulfide nanoparticles will be referred as nanocrystals, given their crystalline structure and the absence of quantum confinement related features.

2.2.2 Electronic properties of bismuth sulfide NCs

Solar cells, and particularly heterojunction-based solar cells, require not only of the existence of electron donating and accepting phases, but also the formation of a type-II heterojunction [41]. It is therefore important to investigate the majority carrier type, ionization potential, electron affinity and the Fermi level of the materials to be employed.

n-type nature, electron mobility and Fermi level

Bulk bismuth sulfide is known to be an *n*-type semiconductor [53]. However, its nanoscale counterpart does not have to share this condition due to the strong

influence of surface states in nanomaterials. Since nanocrystals have a large surface to volume ratio, their surface properties become a key aspect in their overall performance [21]. We have previously discussed that Bi_2S_3 NCs have an excess of bismuth. These off-stoichiometric binary metal chalcogenides with excess metal, are usually found to be *n*-type. For instance, lead sulfide (PbS) CQDs with an exciton peak at 900 nm (size $\approx$ 3.5 nm) are known to be originally *n*-type [60]. However, after oxygen exposure, they first become ambipolar and finally *p*-type materials. Many solution-processed PbS-based Schottky devices fabricated and characterized in air have been reported, showing a *p*-type behaviour [58,61]. It is then important to determine experimentally the type of majority carriers in Bi_2S_3 NCs.

Bottom gated field effect transistors (FETs) were fabricated as shown in Fig. 2.5(a). We deposited a thin ($\approx$ 60 nm) layer of bismuth sulfide nanocrystals in between a channel of silver electrodes and a silica-coated silicon substrate. The formation of an electron-channel at positive gate-source potentials (Fig. 2.5(b)) is indicative of *n*-type materials. It is worth noting that the Bi_2S_3 FET devices were both fabricated and characterized in air.

Carrier mobility is another key parameter for the performance of optoelectronic devices. Under constant carrier lifetime conditions, materials with higher carrier mobilities allow for a longer diffusion length, larger thickness and thus, increased optical absorption. Electron mobility was estimated using the aforementioned FET measurements, by fitting the transconductance with the following expression [21]:

$$\frac{\partial I_{DS}}{\partial V_{GS}} = \frac{W C_i V_{DS}}{L} \mu_E \tag{2.2}$$

where W and L are respectively the width (1 mm) and length (10 μm) of the channel and C_i is the capacitance per area of the silicon dioxide buffer layer (11.5 nF/cm^2 [62]). The calculated electron mobility is $\mu_E = 1.2 \times 10^{-5}$ cm^2/Vs.

Further evidence of the *n*-type nature of Bi_2S_3 nanocrystals can be inferred from the position of the Fermi level relative to the material's electron affinity. The position of the Fermi level in *p*-type materials is close to the valence band edge while in *n*-type semiconductors, it is close to the conduction band. The Fermi level of Bi_2S_3 nanocrystals was measured using ultraviolet photoemission spectroscopy (UPS) and the results are presented in Figure 2.6. We applied an external -5 V electrical bias to the sample and monitored the cut-off region of the binding energy (E_B) spectra. The photoelectron kinetic energy was calculated as $E_K = 21.21$ eV$-E_B - 5$ eV, and the Fermi level was obtained from the interception of the extrapolated onset with the baseline of the spectra [63], which yielded $E_F \approx 4.4$ eV.

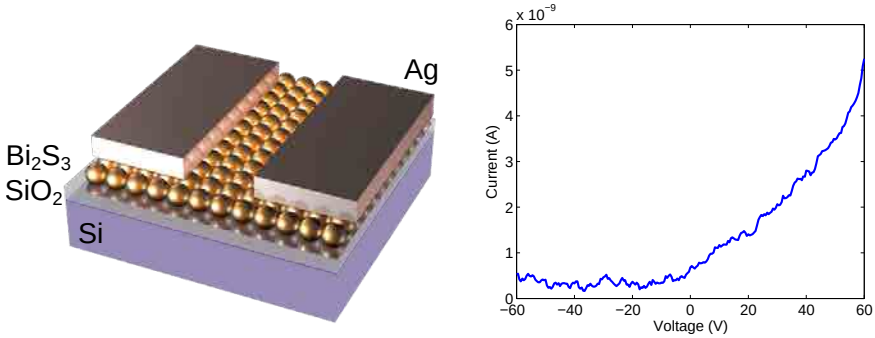

(a) (b)

Figure 2.5: Field effect transistors made of Bi_2S_3 NCs. (a) 3D representation of the FET and (b) transconductance of the bismuth sulfide FET devices.

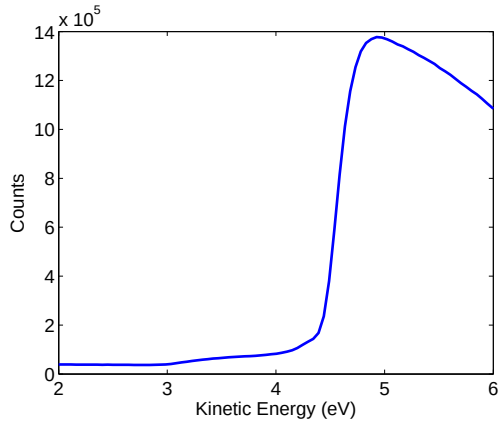

Figure 2.6: Measurement of the Fermi level in Bi_2S_3 NCs by UPS.

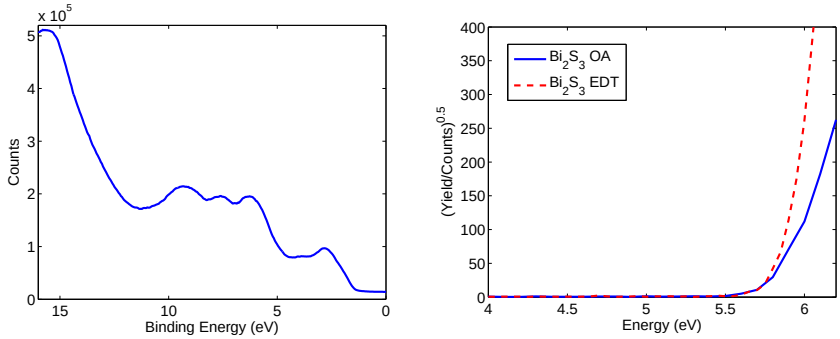

Figure 2.7: Ionization potential of Bi_2S_3 NCs. (a) Ultraviolet photoelectron spectroscopy of the valence band of Bi_2S_3 NCs. (b) Photoelectron spectroscopy in air measurements of Bi_2S_3 NCs capped with oleic acid (solid line) and EDT (dashed line). The valence band edge is positioned at ≈ 5.7 eV.

Ionization potential

Electron affinity determines the position of the conduction band edge whereas ionization potential locates the edge of the valence band. Since the bandgap of Bi_2S_3 NCs has already been calculated from the optical absorption measurements, only one of the two aforementioned energy levels is required to fully-determine the band structure of Bi_2S_3 NCs.

The position of the valence band edge of bismuth sulfide NCs was determined with ultraviolet photoelectron spectroscopy (UPS) and photoelectron spectroscopy in air measurements (Figure 2.7). As shown in Figure 2.7(a), UPS measurements of Bi_2S_3 NCs show a highest occupied molecular orbital (HOMO) cut-off at $\approx$ 1.3 eV below the Fermi level of the material. Taking the Fermi level value obtained before, we conclude that the valence band edge level is at ≈ 5.7 eV [63]. We obtained the same ionization potential value using photoelectron spectroscopy in air measurements (Figure 2.7(b)). The ionization potential level of ≈ 5.7 eV entails a conduction band edge level at ≈ 4.4 eV. We thus conclude that Bi_2S_3 NCs are n-type semiconductors, since the position of the E_F is very close to the conduction band edge.

Carrier density

Having calculated the electron mobility in the Bi_2S_3 NC film we can then estimate the electron carrier density. We fabricated a photoconductor sandwitch-

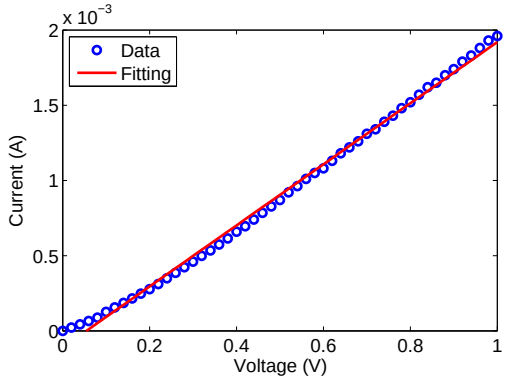

Figure 2.8: Current-voltage characteristics of an ITO/Bi_2S_3/Ag photoconductor in dark conditions.

ing the semiconductor between two ohmic type contacts and we measured the current density under dark conditions. From the results shown in Figure 2.8, majority carrier density (N) can then be estimated as:

$$N = \frac{J}{\mu q E} \tag{2.3}$$

Where J is the current density, μ is the majority carrier mobility and E is the applied electric field. Solving Equation 2.3 using the value for electron mobility obtained from FET devices, we obtain an electron density of $N \approx 8 \times 10^{16}$ cm^{-3}. Compared to other inorganic solution-processed materials, we observe that the carrier density in bismuth sulfide nanocrystals is significantly larger ($\approx 2 \times 10^{16}$ cm^{-3} in PbS QDs [32]). While convenient for maximizing the V_{oc} in photovoltaic devices, a large carrier density might also imply a short depletion region, which ultimately would limit the active layer thickness.

2.2.3 Carrier lifetime

To allow for thick devices and accordingly, increased absorption and higher shortcircuit currents in photovoltaic devices, the semiconductor carrier lifetime has to be long enough so that carriers can reach the electrodes before recombining. The current record holding photovoltaic devices are based on lead sulfide quantum dots. This is in part due to the long carrier lifetimes attained in these systems as a result of favourable shallow traps [64].

We investigated the carrier lifetime of Bi_2S_3 by time-resolved fluorescence spectroscopy (Figure 2.9). A carrier lifetime of 5 ns was calculated by fitting the long-lived component of the PL decay with a monoexponential function. We observe that the carrier lifetime of Bi_2S_3 NCs is short compared to other nanocrystals or quantum dots [65]. This short carrier lifetime can be a limiting factor for the performance of bismuth sulfide-based solar cells.

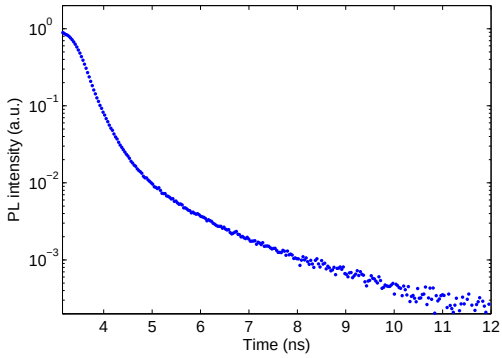

Figure 2.9: Photoluminescence dynamics of bismuth sulfide NCs.

2.3 Summary of the properties of bismuth sulfide NCs

We have identified colloidal bismuth sulfide nanocrystals as an environmentally-friendly direct 1.3 eV bandgap semiconductor with n-type characteristics, even after exposure to oxygen/moisture. The associated energy levels allow for a favourable type-II heterojunction with most of the reported p-type materials and semiconducting conjugated polymers [32,66]. Together, these features make bismuth sulfide nanocrystals interesting candidate materials for third-generation photovoltaics. However, the low electron mobilities and short carrier lifetimes observed in bismuth sulfide nanocrystals, point towards a thin diffusion length in nanocrystalline bismuth sulfide solids. Also, the high electron density in bismuth sulfide nanocrystalline solids is indicative of thin depletion regions. Ultimately, the short diffusion length and short depletion region impose an upper limit on the maximum thickness of the bismuth sulfide layer before carrier recombination exceeds charge transport.

The main electrical characteristics of colloidal Bi_2S_3 nanocrystals are summarized in the following table:

Parameter	Value
Band gap	1.3 eV (955 nm) [53, 56, 57]
Electron Affinity	≈ -4.4 eV
Ionization Potential	≈ -5.7 eV
Fermi Level	≈ -4.4 eV
Doping type	n-type
Carrier density	$N_N \approx 8 \times 10^{16}$ cm^{-3}
Electron mobility	$\mu_N \approx 7 \times 10^{-5}$ cm^2/(Vs)
Carrier lifetime	5 ns
Bulk relative dielectric constant	120 [53]

Chapter 3

Hybrid organic-inorganic solar cells based on bismuth sulfide

The field of organic photovoltaics (OPVs) has seen tremendous progress over the last two decades since the first report of a polymer-fullerene derivative bulk heterojunction device [20, 67]. Despite these advances, the solar harnessing potential of single-junction polymer-based devices has typically been limited to 50% of the total incident solar energy, since their optical bandgap is ≈ 2 eV [68]. The best performing devices show internal quantum efficiencies (IQE) approaching 100%. Therefore, their main limiting factor is incomplete light absorption [19, 69]. A reason for this limited absorption lies in the use of PCBM (phenyl-C_{61}-butyric acid methyl ester) as the electron acceptor phase. PCBM has been the most extensively studied electron accepting material due to its electron-transporting properties, its favourable HOMO-LUMO energy levels as well as the efficient exciton dissociation and ultrafast charge transfer mechanisms observed when employed with most conjugated polymers [20]. However, PCBM is a poor light absorber. Most efforts to enhance polymer solar cell performance have been focused on developing novel polymers with narrower bandgaps and on improving the nanomorphology of the polymer-PCBM blend to achieve efficient exciton dissociation and reduced recombination [20]. An alternative route to improve the power conversion efficiency (PCEs) is the development of new electron acceptor materials with favourable optoelectronic properties, such as increased optical absorption, larger hole mobilities and deeper HOMO-LUMO levels. Recent efforts have been focused on novel fullerene derivatives (such as

$PC_{70}BM$) [70], $n-$type conjugated semiconducting polymers [71] and inorganic nanocrystals [40].

NCs have been proposed as an alternative to the currently used electron accepting materials in organic photovoltaics, i.e. fullerene derivatives. Colloidal inorganic nanomaterials offer chemical stability, high optical absorption and compatibility with low-cost processing techniques [40,66]. Moreover, the bandgap of colloidal quantum dots (CQDs) can be easily tuned via modification of the particle size. The simplicity of bandgap tuning led to their employment as electron acceptor materials in polymer-nanocrystal hybrid solar cells [72]. Since the first demonstration of hybrid solar cells based on the CdS QD and polymer heterojunction [73], various materials and nanocrystal shapes (nanorods, tetrapods...) have been reported in hybrid devices [74]. Hybrid solar cells based on the state-of-the-art semiconducting polymer, poly(3-hexylthiophene) (P3HT), and CdS QDs have reached PCEs of 4.1% [75], lower than but close to those attained in all-organic photovoltaic devices based on the same electron donating material [76]. PbS QDs have also been employed to extend the polymer sensitivity into the infrared [41], achieving PCEs of the order of 3.78% [77].

Both lead-based and cadmium-based QDs contain toxic heavy metals that may prevent their large-scale deployment due to environmental concerns and regulatory acceptance. There has recently been increasing interest in non-toxic materials which has led to the development of a variety of non-toxic nanocrystals. These materials include, among others, Cu_2S [34], CZTS [78], Cu_2O [79] all of which are $p-$doped semiconductors. Metal oxides (i.e. TiO_x and ZnO) is a class of materials that fulfils the requirements for non-toxic, n-type semiconductors. Several reports on polymer-titania [80–83] and polymer-ZnO [84] solar cells exist, however these are high-bandgap semiconductors and therefore do not contribute to solar harnessing.

In Chapter 2 we have presented a set of structural and optoelectronic properties of bismuth sulfide NCs, demonstrating its potential as a solar cell material. In this Chapter we present hybrid organic-inorganic devices based on bismuth sulfide and commercially available semiconducting polymers, employing different device architectures: bilayer and bulk heterojunction devices.

3.1 Bilayer heterojunction devices

Bismuth sulfide NCs form a favourable type-II heterojunction with the widely employed semiconducting polymer P3HT, as shown in Fig. 3.1(a). In this system, electrons are transferred to the Bi_2S_3 phase due to its deeper conduction band, and holes are transferred to the P3HT phase. Also, given the ≈ 2 eV bandgap of P3HT (Figure 3.1(b)), the employment of bismuth sulfide as an

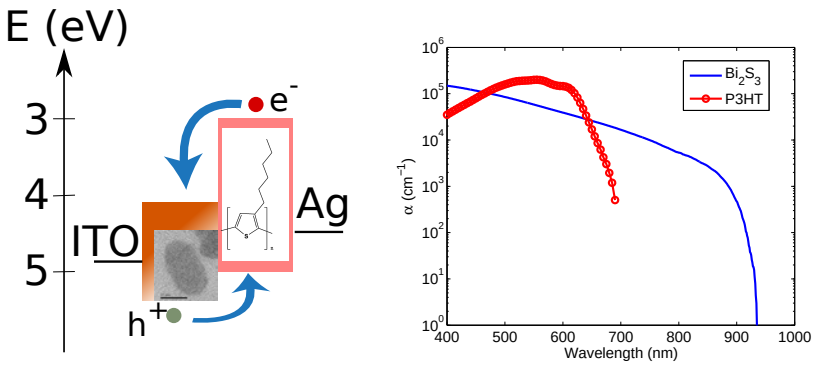

(a) (b)

Figure 3.1: Bi_2S_3-P3HT planar heterojunction. (a) Band diagram and charge transfer mechanism. Electrons from the dissociated exciton are transferred to the Bi_2S_3 whereas holes are injected into the polymer film. (b) Absorption coefficients of Bi_2S_3 (solid blue line) and P3HT (red line with circles).

electron acceptor, can extend the spectral harnessing potential of the hybrid solar cell to NIR wavelengths.

Encouraged by the favourable optoelectronic properties of bismuth sulfide nanocrystals, we have fabricated hybrid organic-inorganic bilayer heterojunction devices employing Bi_2S_3 and P3HT, as sketched in Figure 3.2(a). A cross-sectional scanning electron micrograph of this bilayer architecture is given in Fig. 3.2(b), showing a distinct interface between the two layers. The device fabrication process is detailed in Appendix A.

3.1.1 Photovoltaic performance of the bilayer devices

We fabricated bilayer devices varying the thickness of the Bi_2S_3 layer and measured their current-voltage (I-V) characteristics and spectral quantum efficiency in order to assess as well as to optimize the performance of Bi_2S_3 as an electron acceptor in polymer-NC solar cells. Typical I-V characteristics under simulated AM1.5 and dark conditions are shown in Figure 3.3(a). Devices with various thicknesses of Bi_2S_3 NC layer consistently yielded PCE ranging from $0.3 - 0.46\%$, with maximal PCE achieved employing a 60 nm thick Bi_2S_3 layer. The I-V characteristics of this device resulted in $J_{sc} = 3$ mAcm^{-2}, $FF = 0.49$ and $V_{oc} = 0.32$ V.

Figure 3.3(b) shows the external quantum efficiency (EQE) of the planar het-

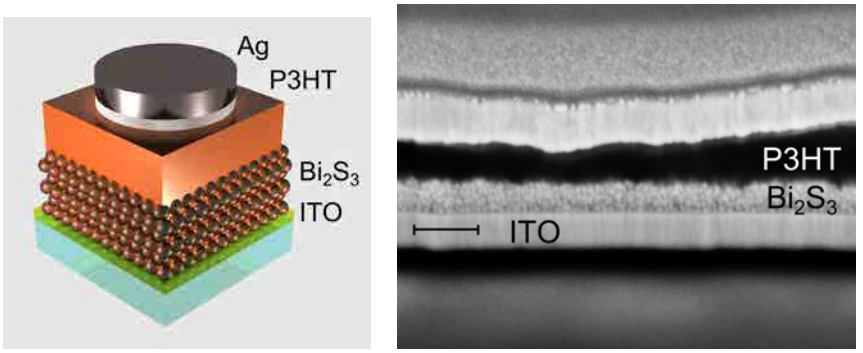

(a) (b)

Figure 3.2: (a) Schematic representation of a bilayer device architecture, where Bi_2S_3 colloidal nanocrystals are deposited onto an ITO-coated substrate, being subsequently covered by the P3HT film and silver electrode (b) Cross-sectional SEM image revealing the nanomorphology of the Bi_2S_3-P3HT bilayer devices. Scale bar 200 nm.

erojunction devices. The absorption of P3HT and Bi_2S_3 are also shown to demonstrate the NIR-sensitization of P3HT-based solar cells. Due to absorption in the Bi_2S_3 film at wavelengths $650 < \lambda < 900$ nm, where P3HT does not absorb, EQE up to 10% is achieved. We performed absolute absorption measurements employing an integrating sphere to plot the internal quantum efficiency (IQE) of our devices in Fig. 3.3(c). The IQE spectra shows two different regions of quantum efficiency: at NIR wavelengths, where absorption occurs solely in Bi_2S_3, IQE of up to $\approx 80\%$ has been achieved for 40 nm thick Bi_2S_3 layers. At shorter wavelengths the IQE drops substantially to $\approx 20\%$. This is due to the fact that only the 10 nm of P3HT which lie at the interface with Bi_2S_3 actually contributes to photocarrier generation due to the short exciton diffusion length of P3HT. Most of photogenerated excitons generated in the bulk of the P3HT film are lost by recombination.

3.1.2 FDTD simulations of the optical absorption profile

In order to estimate the limits of IQE that can be achieved in this novel nanocomposite we employed optical modelling. We used Lumerical, a commercial FDTD software, to model the light absorption profile in our structures. In Fig. 3.4 we plot two-dimensional graphs of the absorption depth profile of light as function of wavelength for the three different thicknesses of Bi_2S_3. We first focus on the NIR window, where Bi_2S_3 is the sole absorbing material. As

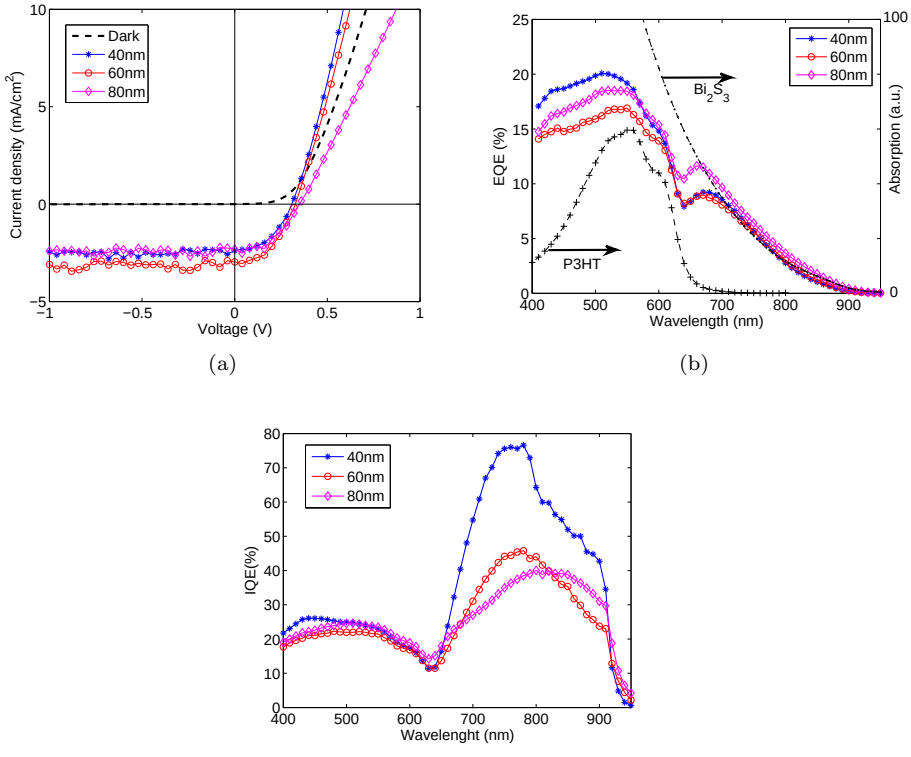

Figure 3.3: Electrical characteristics of Bi_2S_3/P3HT bilayer devices (a) I-V characteristics under simulated AM1.5 and dark conditions of devices with 40 nm (blue solid line with stars), 60 nm (red solid line with circles) and 80 nm (magenta solid line with diamonds) of Bi_2S_3 and P3HT thickness of $\approx$ 120 nm. (b) EQE overlapped with the absorption of Bi_2S_3 (black dotted line) and P3HT (black crosses). (c) Internal Quantum Efficiency (IQE).

evidenced in Fig. 3.4, absorption of light from $650 - 900$ nm takes place close to the interface of Bi_2S_3 with P3HT. The decrease in IQE with increasing Bi_2S_3 thickness in this part of spectrum, as shown in Fig. 3.3(c), suggests that IQE is limited by electron diffusion from the interface to the ITO contact for thickness exceeding 40 nm. For wavelengths longer than 800 nm, IQE drops to $\approx 50\%$, even for 40 nm of Bi_2S_3.

In the visible part of spectrum absorption between $500 - 650$ nm takes place mainly in the P3HT phase, given its higher absorption coefficient compared to Bi_2S_3 (Figure 3.1(b)). However, from the total absorption in P3HT, only light absorbed within 10 nm close to the interface contributes to photocurrent. A local minimum in the EQE spectra appears at ≈ 650 nm as a result of exciton photogeneration far from the dissociation interface.

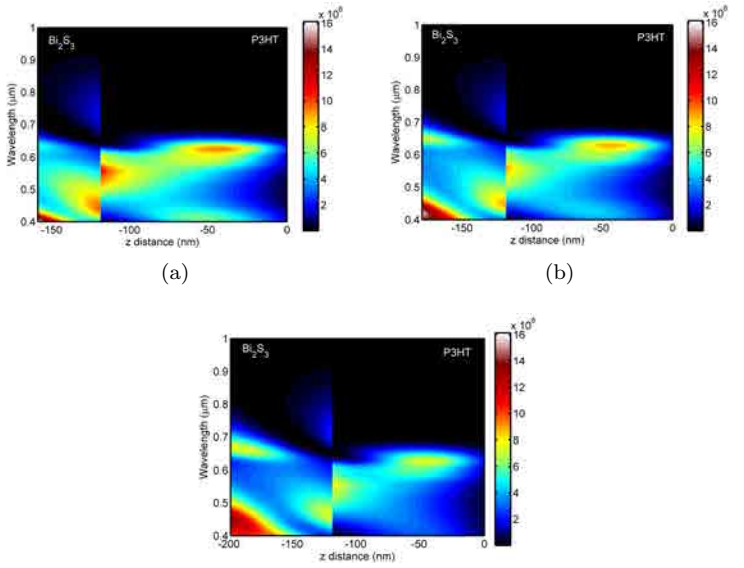

Figure 3.4: FDTD simulations of the optical absorption profile of the respective phases of devices containing 120 nm of P3HT and (a) 40 nm of Bi_2S_3 (b) 60 nm of Bi_2S_3 (c) 80 nm of Bi_2S_3.

3.1.3 Intensity depence of the J_{sc} and V_{oc}

In order to investigate the limiting mechanism of the bilayer device, we performed intensity dependent measurements of the short-circuit current (Fig. 3.5(a)).

In the case of a generation-limited device, we expect a linear relationship between short-circuit current density (J) and incident light intensity (I), thus $J \propto I^{\alpha}$ with α equal to unity. Contrarily, a 3/4 root relationship ($\alpha = 0.75$) is predicted in the case of space-charge limited photocurrent [85]. We obtain an $\alpha = 0.68$, which is indicative of an unbalanced charge transport and recombination limited devices, possibly due to the formation of space-charge regions arising from the dissimilar carrier mobilities.

The presence of trap-states has also been shown to affect the carrier lifetimes of nanocrystal-based devices [61]. Open-circuit voltage decay measurements were performed at different light intensities as a measure of the carrier lifetime (τ). Fig. 3.5(a) shows $1/\tau$, which is proportional to the recombination rate, as a function of light intensity. Increased carrier recombination rate with increasing light intensity has already been reported in lead sulfide-based solar cells, where long carrier lifetimes occur due to shallow trap states [29]. The increased recombination rate, and therefore reduced carrier lifetime, points to a progressive filling of trap states with increasing light intensity. This in turn leads to a shorter carrier diffusion length and thereby larger deviation from the $J \propto P$ at high light intensities.

The intensity dependence of the open-circuit voltage can be fit with a first order polynomial in the semi logarithmic plot. The gradient of the fit gives $S = 2V_t$, where V_t is the thermal voltage (25 mV at room temperature). This steep gradient is indicative of a Shockley-Read-Hall (SRS) trap-assisted recombination process, previously reported in polymer solar cells [86]. In our case, this effect indicates the existence of deep electron trap states that act as recombination centers, leading to poor V_{oc} at low light intensities.

3.2 Bulk heterojunction devices

Colloidal Bi_2S_3 NCs have a short carrier diffusion length and a reduced lifetime compared to other nanocrystalline materials. These two parameters impose an upper limit to the thickness of the bismuth sulfide layer for high internal quantum efficiencies, which we have estimated to be $\approx$ 60 nm based on the performance of planar heterojunctions. In short exciton diffusion length systems (such as most conjugated polymers), a distributed donor-acceptor interface is preferred to maximize exciton dissociation efficiency [67]. We posited that improved photovoltaic performance can be achieved using a hybrid bulk heterojuncion (BHJ) architecture.

Bismuth sulfide NCs and P3HT were mixed together, employing chloroform as the common solvent, and the final product was spincasted on top of the electron transport layer (ETL) as depicted in Figure 3.6(a). The ETL consisted of either

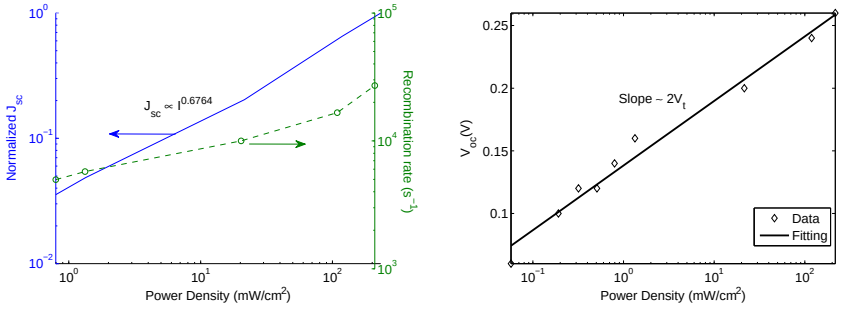

(a) (b)

Figure 3.5: Normalized figures of merit under monochromatic (λ = 635 nm) incident light (a) Normalized short-circuit current density (solid) and charge recombination rate (circles) (b) Open circuit voltage (diamonds) and fitting with a first order polynomial in the semi logarithmic plot (solid line).

a film of Bi_2S_3 NCs or a layer of ZnO. Since there is no preferred direction for the carrier flow in a bulk heterojunction architecture, the role of the electron/-hole transport layers (or equivalently hole/electron blocking layers) is to allow injection of only one type of carrier into the electrode, preventing undesired back recombination. A thin layer of pure P3HT was spincasted on top of the active layer as a hole transport layer (HTL). To complete the device, a top molybdenum oxide (MoO_3) and silver electrode was thermally evaporated through a shadow mask. Details on the fabrication process are given in Appendix A. A cross-sectional scanning electron microscopy (SEM) image is provided in Figure 3.6(b), revealing that Bi_2S_3 NCs tend to form large ($\approx$ 150 nm) agglomerates within the film, whereas the P3HT regions are typically smaller.

3.2.1 Ligand Exchange of bulk heterojunction devices

The importance of replacing the original long insulating capping molecules by shorter ones that allow for carrier hopping between adjacent nanocrystals has been discussed in previous Chapters. It has also been stated that one of the most common methods employed is the LBL method, a very efficient process which yields a dense film of nanocrystals. However, this method is unsuitable for hybrid bulk heterojunctions since the washing steps usually etch away the underlying polymer film. Instead, we dipped the active layer into a bath containing ethanedithiol (EDT), a bidentate molecule that has been widely reported to improve the carrier mobility of metal chalcogenide NCs [87]. This process has

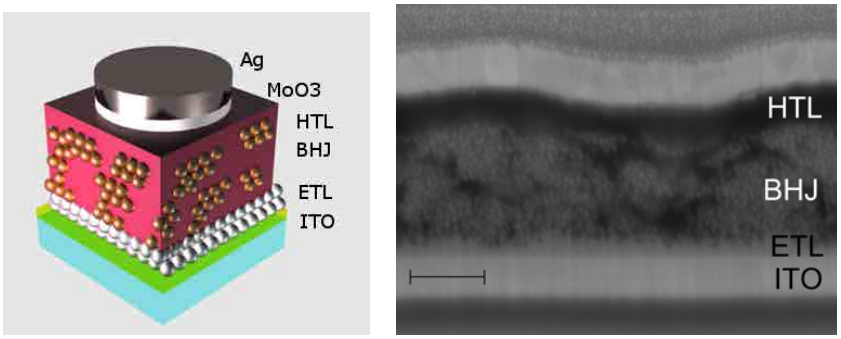

(a) (b)

Figure 3.6: Bulk heterojunction architecture, where a blend of Bi_2S_3 and P3HT is deposited onto the ETL layer and ITO-coated substrate, being subsequently covered by a pure P3HT film (HTL) and MoO_3/Ag electrode. (a) Schematic 3D representation (b) Cross-sectional scanning electron microscopy of the blend devices.

a two-fold role. First, the inter-NC spacing is greatly reduced, favouring charge hopping between adjacent NCs. Second, the thiol group passivates midgap trap states at the metal chalcogenide NC surface, which would otherwise act as recombination centers [61]. To address the effectiveness of the ligand exchange process, Fourier transform infrared spectrometry (FTIR) experiments were carried out. Figure 3.7 shows the FTIR transmission spectra of Bi_2S_3, P3HT and blends both before and after ligand exchange with EDT. The most characteristic features of the oleate-capped-Bi_2S_3 sample are the dips at $\approx$ 1525 cm^{-1} and $\approx$ 1400 cm^{-1}, which are attributed to -COO- stretching. Some thiophene bands in the $1535 - 1515$ cm^{-1} range overlap with the $\approx$ 1525 cm^{-1} band of oleate-capped Bi_2S_3. However, the oleate-capped-Bi_2S_3 band at $\approx$ 1400 cm^{-1} is still visible after mixing Bi_2S_3 with P3HT. Blend films that underwent ligand exchange with EDT show the disappearance of the peak at $\approx$ 1400 cm^{-1}, pointing to a nearly complete removal of the original oleate ligands and their substitution by the shorter EDT molecules.

3.2.2 Photovoltaic performance of the bulk heterojuncion devices

Figures of merit of the solar cells are shown in Table 3.1. Photovoltaic devices that did not undergo the ligand exchange process showed poor performance (0.1%) limited by the low J_{sc}. The insulating oleic acid molecules that allow

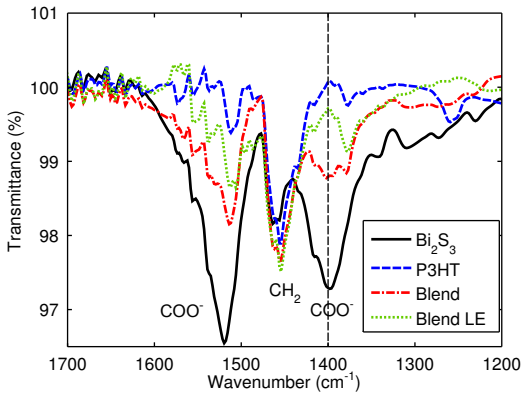

Figure 3.7: Fourier transform infrared spectrometry (FTIR) measurements of oleic acid capped bismuth sulfide nanocrystals (solid black line), P3HT (dashed blue line) and blend before (dashed-dotted red line) and after EDT ligand exchange (dotted green line). The disappearance of the band at ≈ 1400 cm^{-1} after the ligand exchange process is attributed to the removal of the original oleate capping ligands and their replacement by the shorter EDT molecules. The line at 1400 cm^{-1} is provided as a guide to the eye.

for solution processing of NCs but prevent charge transfer between the Bi_2S_3 NCs and the P3HT. After the ligand exchange process with EDT, the performance of the hybrid solar cells is strongly enhanced , due to an over ten-fold increase in J_{sc}. In Figure 3.8(a) we present the current-voltage characteristics of BHJ devices employing two different electron transport layers (Bi_2S_3 and ZnO) and those of a bilayer device as a control. Compared to the control bilayer device, we observe a two-fold increase in power conversion efficiency due to a 2.5-fold increase in the short-circuit current density in EDT ligand-exchanged BHJ devices. The BHJ devices reach EQE levels up to 30% at wavelengths of $700 - 950$ nm where Bi_2S_3 is the only absorbing phase (Figure 3.8(b)). This is a three-fold increase compared to the bilayer device, indicating very efficient charge transfer and carrier transport through the EDT-exchanged Bi_2S_3 due to NCs cross-linking role of EDT.

To determine the effect of the ETL, we compare EDT-exchanged bulk heterojunction devices using Bi_2S_3 and ZnO as ETL. The figures of merit are summarized in Table 3.1. Devices employing a Bi_2S_3 ETL fabricated by an LBL approach yielded PCE levels of 0.9% whereas ZnO-based devices showed similar V_{oc} and FF but a larger J_{sc} (9.2 mAcm^{-2}), with a PCE of 1.0%. The origin for the larger J_{sc} can be seen in Figure 3.8(b). The EQEs of both samples with

Table 3.1: Summary of the hybrid bulk heterojunction devices based on Bi_2S_3 and P3HT

	$V_{oc}(V)$	$J_{sc}(mAcm^{-2})$	$FF(\%)$	$\eta(\%)$
Bi_2S_3 ETL /BHJ unexchanged	0.34	0.6	48	0.1
Bi_2S_3 ETL /BHJ exchanged	0.28	8.0	40	0.9
ZnO ETL /BHJ exchanged	0.30	9.2	36	1.0

different ETLs are similar in the NIR range, reaching as high as 30% at 700 nm. However, the device with ZnO ETL outperforms at UV-VIS wavelengths. Carriers photogenerated in Bi_2S_3 ETL, are likely to recombine due to the low carrier diffusion length in Bi_2S_3. This is because the ETL is not in intimate contact with a neighbouring dissociating interface. Integration of the EQE with the solar spectrum yields a predicted J_{sc} of 9.9 mAcm^{-2} at one-sun intensity, in good agreement with the directly measured AM1.5 J_{sc} value (9.2 mAcm^{-2}) for the device with a ZnO ETL. Taking into account the number of absorbed photons, we have calculated the IQE of the BHJ device with the ZnO ETL (Figure 3.8(c)). Bismuth sulfide nanocrystals contribute to the overall J_{sc}, largely in the NIR, as indicated by IQE of up to 45% at these wavelengths.

3.2.3 Nanocrystal loading

The ideal nanomorphology should provide continuous percolation paths to the collecting electrodes through corresponding donor and acceptor phases. The minimum number of dead-ends is expected to occur at an optimal content of nanocrystals inside the polymer matrix. Below this level, discontinuous pathways in the NC phase might appear whereas above this level, carriers travelling through the polymer phase might get trapped in a dead-end. The IV-characteristics of solar cells with varying nanocrystal loading are presented in Fig. 3.9 and their figures of merit are summarized in Table 3.2. From these results we conclude that the optimal nanocrystal loading is $\approx$ 70% by weight. Above this concentration of NCs, holes experience the formation of dead ends in the polymer while there are discontinuous pathways for electrons below this concentration.

3.2.4 Carrier transport in bulk heterojuncion devices

To investigate the limiting mechanism in our devices and to compare it to the limitations in the bilayer case, we have measured the J_{sc} of the devices at different illumination intensities at a wavelength of 635 nm (Figure 3.10). The

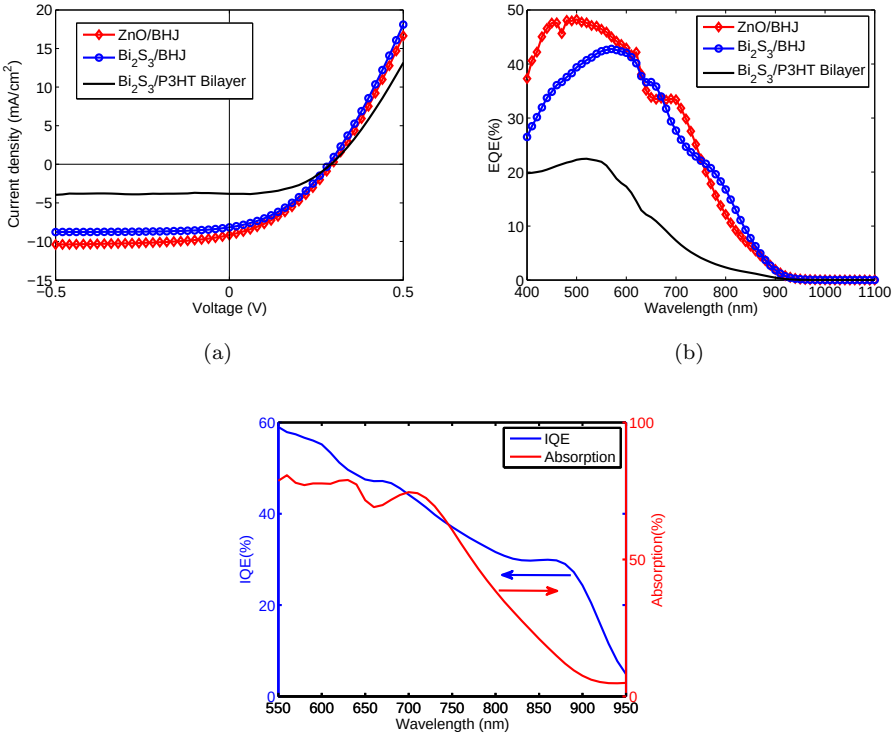

(a) (b)

(c)

Figure 3.8: Photovoltaic performance of the BHJ devices. (a) I-V characteristics of the devices with ZnO (red line with diamonds) and Bi_2S_3 (blue line with circles) as the ETL. The performance of a control bilayer device (black solid line) is provided for comparison. (b) EQE of bilayer and BHJ devices employing ZnO and Bi_2S_3 as ETLs. (c) Internal quantum efficiency (blue solid line) and absorption (red line with circles) spectra of a BHJ device employing ZnO as ETL.

Table 3.2: Optimization of the NC loading.

NC:P3HT wt. ratio	$V_{oc}(V)$	$J_{sc}(mAcm^{-2})$	$FF(\%)$	$\eta(\%)$
60%	0.28	6.0	38	0.6
70%	0.30	6.7	36	0.7
80%	0.28	3.7	35	0.4
90%	0.28	3.3	42	0.4

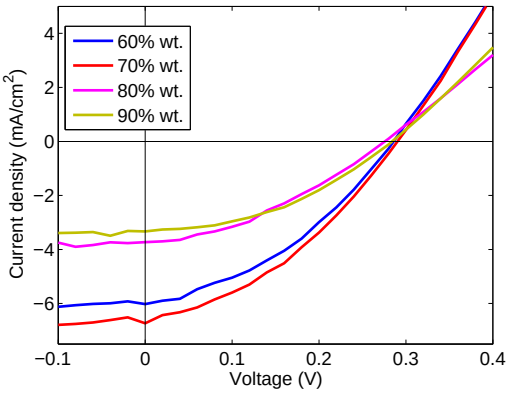

Figure 3.9: Current-Voltage characteristics of hybrid bulk heterojunction devices at different NCs loading. Optimum performance occurs at a $\approx$ 70% by weight NC:polymer concentration.

performance of the Bi_2S_3-P3HT bilayer device is limited by the build-up of space charge regions, as indicated by the J_{sc} dependence on illumination intensity of $J \propto I^{0.64}$. For the bulk heterojunction device of thickness of 150 nm, the power dependence is $J \propto I^{0.91}$ indicative of a generation-limited device. This suggests that by increasing light absorption by using a thicker active layer, the J_{sc} could be improved with minimal loss in the FF and V_{oc}. Indeed, the 150 nm thick device showed a V_{oc} of 0.34 V, J_{sc} of 6.7 mA cm^{-2}, FF of 0.32, for a final PCE of 0.7% while a 350 nm thick device showed a slightly lower V_{oc} (0.30 V), a similar FF (0.36) but a significantly larger J_{sc} (9.2 mA cm^{-2}). Further increasing the BHJ thickness did not improve the J_{sc}, but showed a detrimental effect on the FF and the V_{oc} of the devices, indicating that recombination process has taken over charge transport.

Despite the 2-fold increase in power conversion efficiency in blend devices, the overall PCE attained is still modest. Bismuth sulfide-P3HT heterojunction devices suffer from low fill factors and open-circuit voltages. The former could be overcome by improving the carrier transport, i.e. increasing the carrier mobility, in Bi_2S_3 nanocrystalline solids. Hybrid ligand schemes similar to those demonstrated in PbS CQDs [59] could help in passivating the midgap states in bismuth sulfide nanocrystals which are believed to be responsible for the short carrier lifetime and reduced mobility. Higher V_{oc} levels could be achieved employing semiconducting polymers with deeper energy levels.

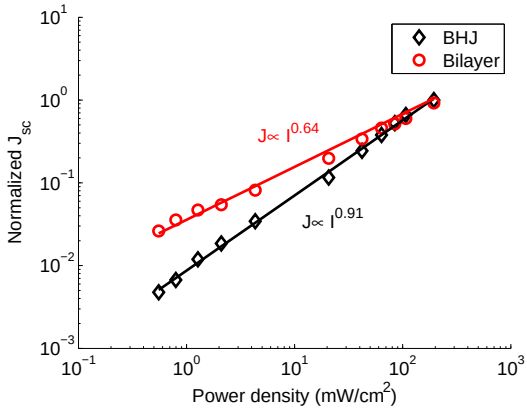

Figure 3.10: Intensity dependence of short-circuit current density under 635 nm laser illumination for bilayer (red circles) and bulk heterojunction (black diamonds) devices. Solid lines correspond to the best fittings of the data with a power-law dependence.

3.3 Novel polymers

Recent advances in the OPV community have led to the demonstration of new semiconducting polymers with tailored optoelectronic properties, such as narrower bandgap, larger hole mobilities and deeper HOMO levels [20]. These novel polymers aim at overcoming the limitations of P3HT as a solar harnessing material. Hybrid organic-inorganic solar cells employing bismuth sulfide as the electron acceptor could also benefit from these recent novel polymer advances, particularly as Bi_2S_3-P3HT heterojunctions exhibit low opencircuit voltages. Higher operating voltages can be expected replacing P3HT with a deeper HOMO polymer to increase the HOMO-LUMO separation of the donor-acceptor interface.

3.3.1 HOMO dependence of the open-circuit voltage in hybrid bilayer devices based on bismuth sulfide NCs

We investigated the performance of devices based on bismuth sulfide nanocrystals in conjunction with several novel semiconducting polymers with different HOMO levels as electron donors. Details on the semiconducting polymers employed and their optoelectronic properties are given in Appendix B. For sim-

plicity, we employed a bilayer architecture. The highest V_{oc} attained with every polymer-nanocrystal combination as a function of donor HOMO is presented in Figure 3.11. Although the polymer HOMO can usually be obtained from the manufacturer, we employed cyclic-voltammetry to determine the HOMO level of all the polymers employed in this study, thus reducing the uncertainty associated with different experimental techniques. Deeper HOMO polymers provide for larger operating voltages in agreement with the results obtained in similar studies, where the relationship $V_{oc} \propto m\text{HOMO}$ was obtained [88]. Contrary to the results obtained in all-organic solar cells where PCBM was used as the electron accepting media (gradient $m = 1$), we obtain a gradient $m = 0.5$. The origin of this difference is still unclear and further experiments are to be performed to clarify it. One possible explanation is that the presence of midgap trap states in the bismuth sulfide pins its Fermi level, ultimately limiting the V_{oc}. Given the structural differences in the polymers employed, it is possible that some of them allow for better coordination with the surface of the bismuth sulfide nanocrystals, effectively passivating some of these interface states.

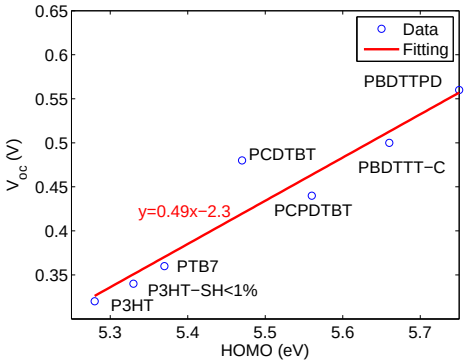

Figure 3.11: Relationship between V_{oc} and donor HOMO in hybrid planar heterojunctions based on bismuth sulfide nanocrystals.

3.3.2 Photovoltaic performace

Encouraged by the larger opencircuit voltages obtained with deeper HOMO polymers, we measured the PCE of the hybrid organic-inorganic bilayer heterojunctions. From the results presented in Table 3.3, it is difficult to draw conclusions as to the effect on the HOMO level on the overall solar cell performance since it is not the only variable changing from one polymer to another.

Table 3.3: Photovoltaic performance of bilayer devices based on bismuth sulfide NCs and novel polymers with deeper HOMO-LUMO levels.

Polymer	V_{oc}	$J_{sc}(mAcm^{-2})$	$FF(\%)$	$\eta(\%)$
P3HT	0.32	3.0	49	0.46
PTB7	0.36	2.18	58	0.46
PCDTBT	0.48	0.59	45	0.13
PCPDTBT	0.44	0.28	24	0.03
PBDTTT-C	0.50	0.66	61	0.2
PBDTTPD	0.56	0.11	34	0.02

Table 3.4: Optoelectronic propierties of the novel polymers with deeper HOMO-LUMO levels.

Polymer	HOMO (eV)	BG (eV)	μ_H (cm^2/Vs)
P3HT	5.28	1.9	7×10^{-3}
PTB7	5.37	1.6 [89]	5×10^{-3}
PCDTBT	5.47	1.9 [90]	5×10^{-6} [91]
PCPDTBT	5.56	1.45 [92]	9×10^{-4}
PBDTTT-C	5.66	1.6 [69]	1×10^{-3}
PBDTTPD	5.75	1.9 [93]	5×10^{-5}

As shown in Table 3.4, other parameters such as the hole mobility and bandgap also need to be taken into account. It is clear from the results in Table 3.3, that none of the semiconducting polymers tested outperform P3HT despite achieving larger operating voltages.

We attempted to employ these novel polymers in a bulk heterojunction architecture to maximize the photovoltaic performance. However, these polymers are not readily miscible with Bi_2S_3 NCs, possibly due to steric hindrance. We generally observed a large degree of vertical phase segregation in the nanomorphology of the BHJ devices based on polymers other than P3HT, where bismuth sulfide NCs appeared to be spun out of the active layer (Figure 3.12). Alternative strategies to increase the electronic interaction of these novel polymers with Bi_2S_3 NCs are to be sought. One possible strategy is to incorporate functional groups in the polymer chain that anchor the polymer onto the NCs surface.

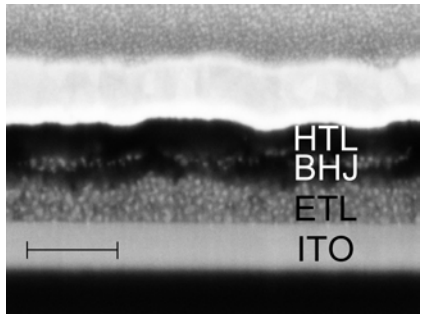

Figure 3.12: Cross-sectional SEM image of a Bi_2S_3:PCDTBT bulk heterojunction solar cell. Scale bar 200 nm.

3.4 Summary

In this work we have demonstrated bismuth sulfide nanocrystals as electron acceptors in hybrid organic-inorganic solar cells based on state-of-the-art commercially available semiconducting polymers. We have optimized the thickness of the bismuth sulfide layer in bilayer devices, which we found to be approximately 60 nm. It is a result of the low carrier mobility combined with the fast recombination observed in nanocrystalline bismuth sulfide solids. The low carrier density in Bi_2S_3 also causes unbalanced charge transport in the planar photovoltaic devices, which limit carrier extraction due to the formation of space charge regions. Furthermore, the presence of trap states is also limiting photovoltaic performance.

To overcome the short diffusion length of both bismuth sulfide and P3HT, we have developed hybrid organic-inorganic bulk heterojunction solar cells. Solar cells based on a distributed dissociating interface allow for thicker devices and accordingly increased optical absorption and short-circuit current. After optimizing the relative quantities of the two constituents, continuous percolation pathways that can effectively extract the photogenerated carriers are obtained. We observed that hybrid bulk heterojunction devices are limited by the agglomerated NCs nanomorphology, by the reduced open-circuit voltage and by the trap states that limit the carrier mobility and accelerate recombination.

We have also shown that novel semiconducting polymers with deeper HOMO levels allow for larger operating voltages when combined with bismuth sulfide NCs. However, these polymers were not readily miscible with the NCs, generally leading to vertically phase-seggregated films. We propose that incorporation of functional groups in the polymer chain could help in anchoring the polymer onto the NCs surface and increase their electronic interaction.

Chapter 4

Hybrid solar cells based on bismuth sulfide and a thiol-functionalized block copolymer

Identifying the optimal processing conditions (including among others solvent, loading ratio, concentration, spinning rate and post-processing treatments) for maximizing the photovoltaic performance of bulk heterojunction organic solar cells has been one of the major research lines in the organic photovoltaic community. The main reason being that this simple fabrication process leads to the formation of disordered nanostructures; the random nature of which can be the main cause of repeatability and reproducibility issues [94]. Identifying the right combination of processing parameters that provides for a nanoscale morphology with domains smaller than the exciton diffusion length is not straightforward. Hybrid solar cells based on colloidal nanocrystals and semiconducting polymers also face these nanomorphology challenges. Moreover, they face other challenges such as enabling efficient charge transport through NC-based solids via ligand engineering while preserving the interaction of the NCs with the polymers. We presented in Chapter 3 hybrid bulk heterojunction solar cells based on bismuth sulfide and P3HT and showed that the original capping ligands had to be replaced by shorter molecules in order to allow for charge transfer and transport. The nanomorphology of such devices relied on a random distribution of nanoparticles inside the semiconducting polymer matrix, which after exposure to a bidentate molecule such as EDT, tend to form agglomerates with typical

dimensions of some hundreds of nanometers. Polymer regions were found to be typically smaller, but probably still too large to provide for almost unity exciton dissociation efficiencies.

Recently, an alternative approach to the random formation of nanodomains has been proposed, which benefits from the strong interaction observed between amine, carboxyl or thiol functional groups and metal chalcogenide nanocrystals [95]. In the seminal work by Fréchet et al, the semiconducting polymer was modified to incorporate an amine functional group close to the polymer backbone. More recently, block copolymers employing an ester functional group were proposed and demonstrated [96]. The authors reported an improved nanomorphology, although no improvement in the photovoltaic performance with respect to the bare polymer was observed. A plausible explanation is that the block copolymer ratio employed (30%) led to an excessive covering of the nanocrystals' surface, thus hindering NC-NC interaction. Alternatively, it could be due to a poor electronic interaction between the ester-functionalized block copolymer and the nanocrystals which hinders charge transfer between the polymer and NCs. We have adopted a similar strategy, incorporating thiols as the functional group as they have a strong binding ability to metal chalcogenide NCs [97], but we employed much lower block copolymer ratios. Also, thiol groups have been demonstrated to passivate NC midgap states [61]. We posited that thiol-functionlaization could lead to better electrical interaction between the polymer and the NCs' surface and reduce undesired trap assisted carrier recombination due to passivation of available dangling bonds present at the surface of metal chalcogenide nanocrystals.

4.1 Characterization of the block copolymer

A new block copolymer functionalized with a thiol group, based on hexylthiophenes (namely P3HT-SH) was synthesized via the quasi-living Grignard metathesis reaction (GRIM) polymerization method reported by McCullough and Yokozawa [98, 99]. The chemical structure of the synthesized block copolymer is depicted in Figure 4.1(a) and details on its synthesis and structural characterization are given in Appendix C. Thiol groups were attached at the end of the side chains which are located on the 3-position of thiophene rings of the second block. We synthesized several block copolymers with different block ratios, defined as $\frac{m}{m+n}$, as depicted in Figure 4.1(a). The block copolymer ratios employed were as low as $< 1\%$, limited by nuclear magnetic resonance (^{1}H NMR) resolution. The ^{1}H NMR of the different thiol-functionalized block copolymers is presented in Figure C.3.

Figure 4.1(b) shows the optical absorption of films of P3HT and P3HT-SH,

showing that P3HT-SH is slightly more amorphous than P3HT. P3HT-SH shows a slight blue-shift of the absorption peak and slightly less pronounced shoulder at around 600 nm, compared to P3HT (Figure 4.1(b)). The differences observed are subtle, in view of the large spectral differences between highly crystalline and amorphous P3HT [100]. We performed grazing incidence x-ray diffraction (GI-XRD) to further assess the polymer order. Figure 4.1(c) shows the two-dimensional GI-XRD images and Figure 4.1(d) shows the out-of-plane x-ray diffraction patterns of both P3HT and P3HT-SH demonstrating a prominent (100) peak at $Q_z = 0.38$ Å^{-1}. The relative intensities between the (100) peak and the secondary and tertiary diffraction peaks are comparable for P3HT and P3HT-SH, which indicates similar extents of crystallinity in the two polymers. Figure 4.1(e) shows the radial integration of the π-stacking peak at $Q \approx 1.7$ Å^{-1}. The center of this peak is slightly shifted to smaller Q for P3HT-SH compared to P3HT. Fitting the curves with Lorentzian functions also revealed a wider peak for P3HT-SH (FWHM=0.167 Å^{-1}) compared to P3HT (FWHM=0.149 Å^{-1}). The shift and increased width indicate that the polymer packing is slightly disturbed by the presence of the thiol group in the thiol-functionalized block copolymer. Nevertheless, the structural results indicate that both polymers have a similar degree of crystallinity and optical bandgap, making P3HT-SH a viable semiconducting polymer for solar applications in combination with metal chalcogenide nanocrystals.

4.1.1 Energy levels

We performed cyclic-voltammetry measurements to determine the position of the highest occupied molecular orbital (HOMO) in P3HT-SH. From the onset of the first oxidation peak at ≈ 5.5 eV (Figure 4.2(a)), we found that the HOMO level of P3HT-SH (5.33 eV) is approximately 50 meV deeper than that of regioregular P3HT (5.28 eV). The absolute position of the P3HT HOMO level with respect to vacuum was found to be close to that already reported for P3HT employing cyclic-voltammetry measurements [101]. A similar 50 meV HOMO offset between the two semiconducting polymers was observed employing photoelectron spectroscopy in air (Figure 4.2(b)).

We have shown that the presence of the thiol functional group in the polymer chain causes perturbations in the packing of the polymer film, thus leading to the formation of a slightly less crystalline phase, as already pointed out by the slight blue shift in optical absorption. Given the low amount of thiol moieties employed in this study, we expect a minor influence on the polymers' long-range electrical properties. The observed HOMO change is much smaller than the 300 meV HOMO difference reported between crystalline and amorphous P3HT films [100], which indicates that there is still a large degree of long-range

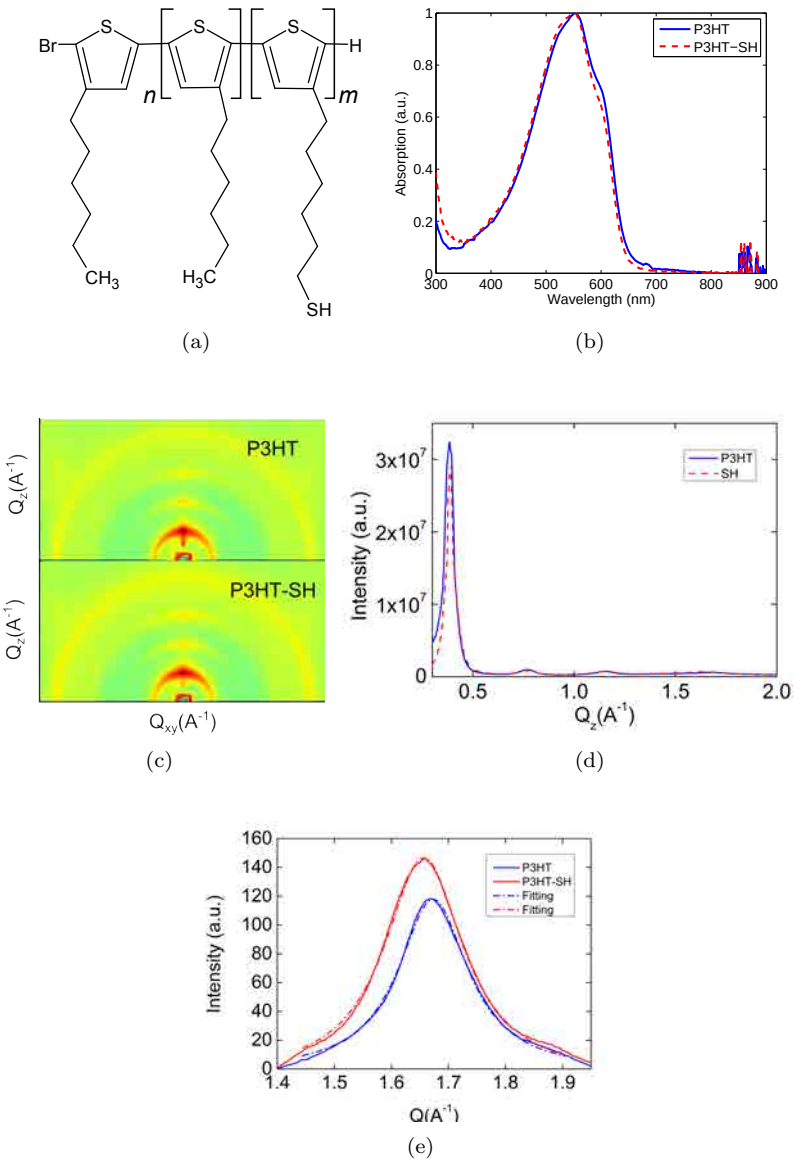

Figure 4.1: (a) Chemical structure of P3HT-SH and (b) normalized absorption of P3HT (blue solid line) and P3HT-SH (red dashed line) in spincoated films on glass (c) 2D GI-XRD pattern of P3HT and P3HT-SH (d) GI-XRD diffraction pattern along the out-of-plane direction of P3HT (blue solid line) and P3HT-SH (red dashed line)(e) Radial integration of the π-stacking peak at $Q \approx 1.7$ $\AA^{-1}$ from (c).

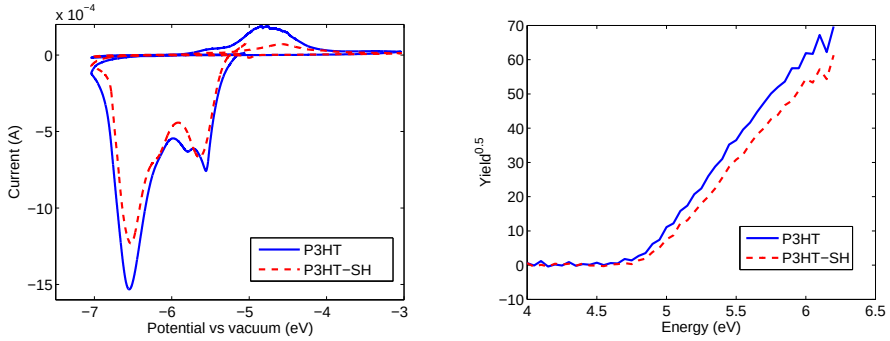

(a) (b)

Figure 4.2: (a) Cyclic-voltammetry measurements of P3HT (blue solid line) and P3HT-SH (red dashed line) (b) Photoelectron spectroscopy in air of P3HT (blue solid line) and P3HT-SH (red dashed line).

ordering in the thiol-functionalized P3HT.

4.1.2 Carrier mobility

Bottom gated field effect transistor (FET) devices were fabricated on silicon substrates coated with 200 nm of thermally grown silicon dioxide using gold as top drain and source electrodes. Hole mobilities were calculated from the slope of the transconductance (Figure 4.3) according to the following expression [21]:

$$\mu = \frac{L \frac{\partial I_{ds}}{\partial V_{gs}}}{W C_i V_{ds}} \tag{4.1}$$

where L and W stand for the channel length and width, respectively, V_{ds} is the drain-source voltage applied (15 V) and C_i is the capacitance per unit area of the insulator (17 nFcm^{-2} [62]). Calculated hole mobilities are 7×10^{-3} and 1×10^{-2} cm^2/Vs for P3HT and P3HT-SH$<$ 1%, respectively. The similar hole mobilities observed for P3HT and P3HT-SH (also comparable to those obtained for highly regioregular P3HT [102]) provide further evidence of a highly crystalline polymer phase in P3HT-SH.

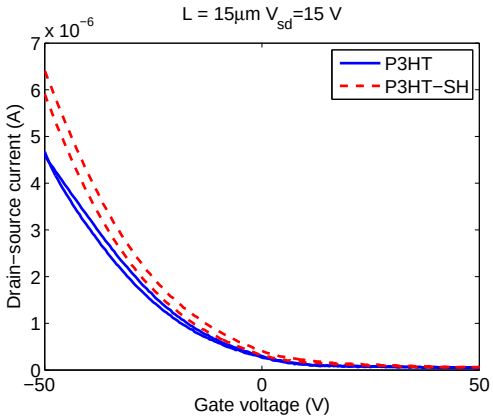

Figure 4.3: Field effect transistor measurements on P3HT and P3HT-SH. Hole mobilities were calculated from the slope of the transconductance in the linear regime.

4.2 Exciton dissociation and charge transfer

To investigate the affinity of the thiol-functionalized P3HT (P3HT-SH) to the nanocrystal surface and the corresponding degree of electronic interaction between P3HT-SH and Bi_2S_3, we performed photoluminescence (PL) quenching studies in solution. Photoluminescence quenching is a standard technique to monitor the electronic interaction, i.e. charge transfer, between two molecules or between polymer and semiconductor nanocrystals [40]. Even highly efficient photovoltaic systems such as P3HT:PCBM do not show any significant photoluminescence quenching in solution [103], indicating no specific intermolecular interaction between the two molecules. Photoluminescence is dramatically quenched after film formation [104]. We compared the intensity of the PL spectra of P3HT and P3HT-SH both before and after blending with Bi_2S_3 nanocrystals. Figure 4.4(a) shows the PL spectrum of P3HT-SH from which a strong quenching (50% reduction in counts) after blending with Bi_2S_3 can be observed. This PL quenching is much larger than that observed for the Bi_2S_3:P3HT solution ($\approx$ 20%) as shown in Figure 4.4(b). This suggests efficient charge transfer between the functional block copolymer and the NCs of Bi_2S_3 compared to P3HT and Bi_2S_3, as a result of anchoring of the P3HT-SH on the surface of Bi_2S_3 NCs, via the thiol moiety. It is noteworthy that no ligand exchange method has been employed to remove the original insulating oleic acid molecules from the surface of the bismuth sulfide nanocrystals. The slight ($\approx$ 20%) PL quenching observed in the Bi_2S_3:P3HT system can be attributed to an incom-

plete capping of the NCs' surface by the sterically large oleic acid molecule [60], since in this latter system there is no thiol or functional group to replace the oleic acid molecule. Unpassivated bismuth atoms in the nanocrystal surface, can then weakly interact with the sulfur atom in the thiophene ring. Figure 4.4(c) shows the PL spectra of thin-films of pristine P3HT and P3HT-SH, both before and after blending with Bi_2S_3 nanocrystals. We observe an almost complete PL quenching in solid state for both polymers after blending with Bi_2S_3 NCs. Since the high degree of PL quenching prevents us from comparing the charge separation efficiency between P3HT and P3HT-SH in solid state, an alternative method is required.

Transient absorption spectroscopy (TAS) can be employed to monitor the exchange of excited carriers between two different materials [105]. In this pump-probe technique, long lived ($\approx \mu$s) excited species are generated after illumination at the pump wavelength and the change in optical absorption at the probe wavelength is monitored as a function of excitation wavelength or time. Following excitation with visible light, a broad transient absorption peak centered around $\lambda = 1000$ nm is observed after 1 μs for both P3HT and P3HT-SH (Figure 4.5(a)) which has been attributed to the P3HT hole polaron [106]. As this peak is similar for both polymer systems we are able to study the transient decay of the peak at $\lambda = 1000$ nm wavelength for all polymer-nanocrystal blend films. The hybrid organic-inorganic films were excited either with a visible laser pulse of $\lambda = 510$ nm, thus exciting both polymer and the nanocrystals, or with a near-IR pulse of $\lambda = 700$ nm, exciting only the nanocrystals. Considering first the near-IR excitation (Figure 4.5(b)), where only the nanocrystals are absorbing the excitation light, the magnitude and lifetime of the signals in the P3HT and P3HT-SH samples are approximately the same. This suggests that the addition of the thiol group onto the P3HT alkyl chain has little effect on the hole transfer from the Bi_2S_3 nanocrystals to the polymer or on the recombination dynamics. Considering the visible excitation (Figure 4.5(c)), where both the polymer and nanocrystals are excited, the intensity of the TAS signal of the P3HT-SH samples is higher in comparison to the pristine P3HT. This suggests that the effect of the addition of the thiol group is to increase the amount of electron injection from polymer to nanocrystal, while the hole transfer remains unchanged. This is attributed to morphological changes of the composite. Blends of P3HT and Bi_2S_3 NCs result in aggregated films, with domain sizes of the order of some hundreds of nanometers (Figure 4.6(a)). A large number of excitons are thus generated far away from a dissociating interface. When P3HT-SH is blended with Bi_2S_3 NCs a finer dispersion of NCs is observed (Figure 4.6(b)), with much smaller domain sizes. The smaller nanodomains observed when employing thiol functionalized block copolymer ensure that excitons are formed much closer to a dissociation interface throughout the whole active layer, increasing the exciton dissociation probability. The morphology improvements observed with P3HT-

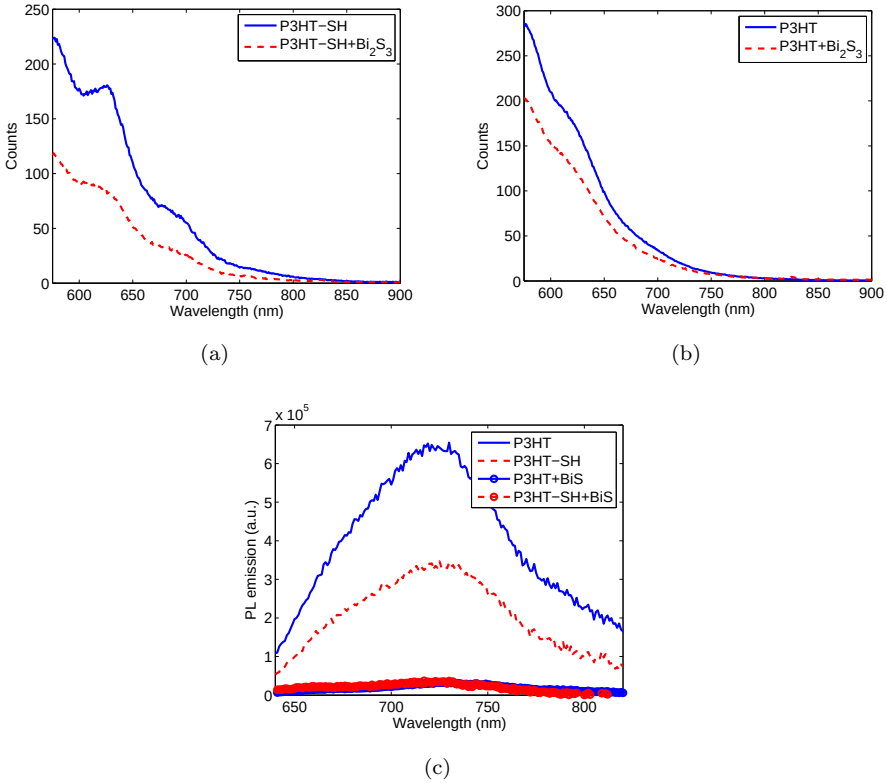

Figure 4.4: Photoluminescence (PL) spectra of (a) chloroform solutions of pristine P3HT-SH (solid blue line) and of a blend of P3HT-SH:Bi_2S_3 (red dashed line) (b) chloroform solutions of pristine P3HT (solid blue line) and of a blend of P3HT:Bi_2S_3 (red dashed line) and (c) PL spectra of P3HT (blue solid lines) and P3HT-SH (red dashed lines) in pristine films (solid lines) and in blend films with Bi_2S_3(lines with circles). The PL spectrum for each sample has been normalized to the sample absorption at the excitation wavelength.

Table 4.1: Photovoltaic performance of hybrid bulk heterojunction devices employing thiol-functionalized block copolymer

Polymer type	V_{oc} (V)	J_{sc} (mAcm^{-2})	FF (%)	η (%)
P3HT	0.31 ± 0.01	7.71 ± 0.25	35.6 ± 0.8	0.85 ± 0.02
P3HT-SH< 1%	0.29 ± 0.01	1.64 ± 0.14	47.5 ± 5.2	0.22 ± 0.02
P3HT:P3HT-SH< 1%	0.34 ± 0.007	7.19 ± 0.30	41.0 ± 1.3	1.01 ± 0.04

SH are preserved in ternary blends of P3HT, P3HT-SH and Bi_2S_3, as shown in Figure 4.6(c). A device sketch is shown in Figure 4.6(d), shows conceptually the different layers employed and shown in the cross-sectional SEM pictures.

Both after visible and near-IR excitation a blend of Bi_2S_3 with both P3HT and P3HT-SH yields the largest amount of charges, as evidenced by the stronger TAS signal. Since the nanomorphology is similar for both Bi_2S_3:P3HT-SH and a blend of Bi_2S_3 and P3HT and P3HT-SH (Figure 4.6(b) and Figure 4.6(c)), we believe this effect is most likely due to an energy cascade like that depicted in Figure 4.7. This energy cascade arises from the different HOMO levels observed in P3HT and P3HT-SH and drives charges away from the interface. This hypothesis is further supported by the increased electronic and chemical interaction between P3HT-SH and the nanocrystals observed in PL quenching and cross-sectional SEM.

4.3 Photovoltaic performance of bulk heterojunction devices

Encouraged by the stronger electronic interaction between P3HT-SH and Bi_2S_3 NCs observed in PL quenching and TAS measurements and from the improved nanomorphology, we fabricated photovoltaic devices. The device structure was ITO/ZnO/BHJ/P3HT/MoO3/Ag, where BHJ is a mixture of Bi_2S_3 nanocrystals and the polymers (P3HT and/or P3HT-SH). Table 4.1 summarizes the performance of the solar cells and details on the device fabrication and characterization are given in Appendix A.

Solar cells based on Bi_2S_3 and P3HT-SH showed a poor photovoltaic performance (PCE= 0.22%), as a result of very low short-circuit current densities. This is attributed to an excessive covering of the NC surface by the thiol-functionalized block copolymer, which hinders carrier hopping between adjacent nanocrystals. This effect could also be the reason why previous works employing functionalized polymers in conjunction with inorganic nanocrystals

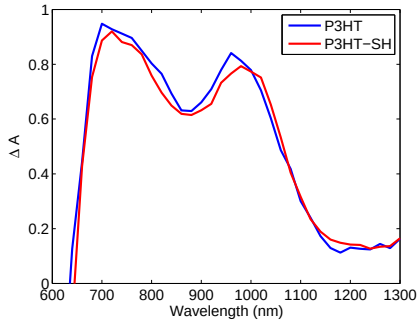

(a)

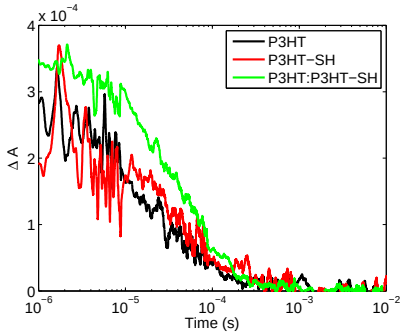

(b)

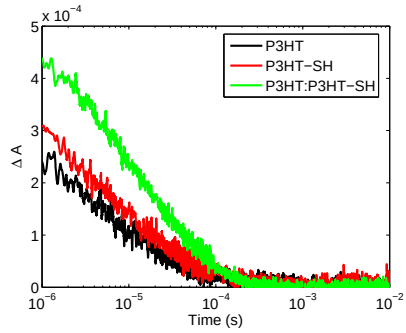

(c)

Figure 4.5: Transient absorption spectroscopy (TAS) (a) Normalized transient absorption spectra of pristine P3HT (black line) and pristine P3HT-SH (red line). Transient absorption dynamics after (b) IR excitation (700 nm) and (c) visible excitation (510 nm) of blends of: Bi_2S_3 and P3HT (black line), Bi_2S_3 and P3HT-SH (red line) and Bi_2S_3 and P3HT and P3HT-SH (green line) after ligand exchange with EDT.

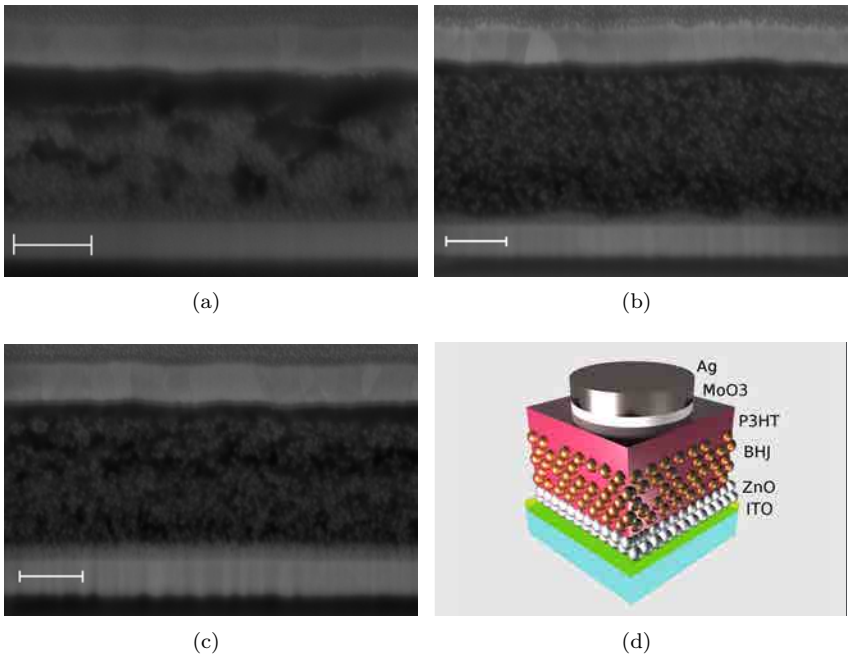

Figure 4.6: Cross-sectional scanning electron micrograph of (a) blends of Bi_2S_3:P3HT (b) Bi_2S_3:P3HT-SH and (c) Bi_2S_3 and a 70 : 30 wt. mixture of P3HT and P3HT-SH. Scale bars: 200 nm. (d) Schematic representation of Bi_2S_3/P3HT-SH bulk heterojunction devices.

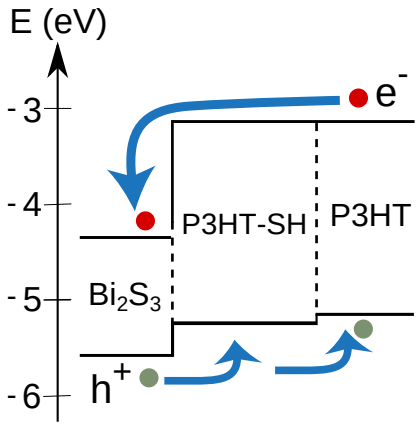

Figure 4.7: Energy diagram of the ternary hybrid organic-inorganic nanocomposites.

Table 4.2: Figures of merit of the hybrid solar cells based on bismuth sulfide and employing different P3HT to functionalized P3HT ratios.

P3HT to P3HT-SH ratio (%wt)	V_{oc} (V)	J_{sc} (mAcm^{-2})	FF (%)	η (%)
60 : 40	0.36	6.5	42	0.97
70 : 30	0.34	7.6	42	1.1
80 : 20	0.34	7.1	36	0.87

have not achieved higher power conversion efficiencies and have been unable to benefit from the observed improved nanomorphology [96]. In view of the optimal morphology and increased degree of polaron formation observed in TAS measurements, we decided to employ a mixture of P3HT and P3HT-SH as the electron donating material. Table 4.2 summarizes the figures of merit of the devices with different P3HT:P3HT-SH ratios.

At a P3HT to P3HT-SH weight ratio of 70 : 30 the highest power conversion efficiency (1.1%) is achieved due to a higher J_{sc} (7.6 mAcm^{-2}). The charge separation mechanism in these devices drives the photogenerated holes into the polymer while electrons are injected into the bismuth sulfide nanocrystal phase and can reach the collecting electrode via the hopping mechanism [25]. The photovoltaic performance increases with a decrease in the thiol moiety content. The figures of merit of the solar cells based on 4%, 1% and $< 1\%$ block

Table 4.3: Figures of merit of the hybrid solar cells based on bismuth sulfide and employing different block copolymer ratios at a P3HT:P3HT-SH ratio of 70 : 30.

Block copolymer ratio	V_{oc} (V)	J_{sc} (mAcm^{-2})	FF (%)	η (%)
$< 1\%$	0.34	7.6	42	1.1
1%	0.36	6.3	45	1.0
4%	0.32	6.1	38	0.7

copolymer ratios are presented in Table 4.3. The increasing photovoltaic performance with decreasing thiol content in the polymer network is consistent with the aforementioned excessive covering of the NCs' surface by the P3HT-SH at high block copolymer ratios, isolating the nanocrystals and ultimately hindering the carrier hopping mechanism. Our best device showed V_{oc} of 0.34 V, J_{sc} of 7.6 mAcm^{-2} and FF of 42% with a PCE of 1.1%, about 15% higher than that obtained with only P3HT. The current-voltage characteristics of the solar cells based on pristine P3HT, pristine P3HT-SH and the optimized P3HT:P3HT-SH ratio are shown in Figure 4.8(a), statistics are given in Table 4.1 and external quantum efficiency (EQE) measurements are presented in Figure 4.8(b).

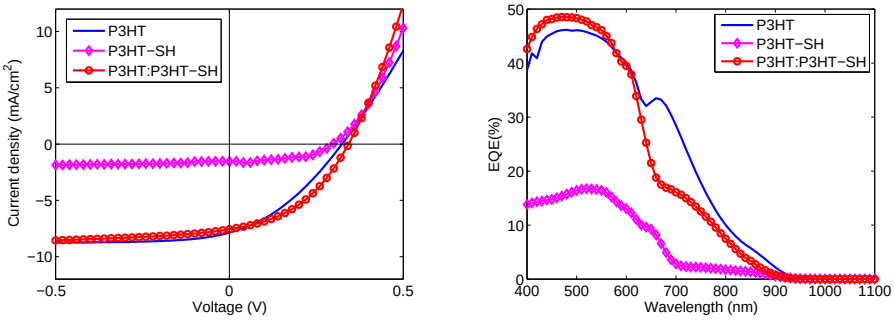

(a) (b)

Figure 4.8: Photovoltaic performance of hybrid bulk heterojunction devices employing thiol-functionalized block copolymer. (a) Current-voltage characteristics and (b) External quantum efficiency of the devices with only thiol-functionalized P3HT (magenta line with diamonds) and a 70 : 30 wt mixture of regular P3HT and P3HT-SH (red line with circles) compared to that of devices based on regular P3HT (blue solid line).

Integration of the EQE convoluted with the power density of the solar spectrum

predicts a short-circuit current density of 8.2 $mAcm^{-2}$, that is $\approx$ 10% larger than the J_{sc} value of 7.6 $mAcm^{-2}$, obtained under simulated AM1.5 conditions. The reduction of the measured J_{sc} in comparison to the expected J_{sc} is attributed to trap-assisted recombination which causes a sublinear photocurrent response with light intensity, slightly overestimating the EQE as we have previously discussed for hybrid organic inorganic systems based on Bi_2S_3 and P3HT.

4.4 Summary

In this work we have addressed the aggregation of nanocrystals that we had previously observed in photovoltaic devices based on blends of colloidal bismuth sulfide nanocrystals and P3HT. We have shown that incorporating a thiol moiety in the polymer alkyl chain and close to the polymer backbone, allows for polymer binding to the nanocrystal surface, ultimately preventing their agglomeration. The presence of the thiol functional group slightly distorts the polymer packing although it preserves most of its long-range crystalline ordering, optical bandgap and hole mobility properties. As a result, P3HT-SH has a slightly deeper HOMO level than that observed in regioregular P3HT. We have also demonstrated that employing P3HT-SH improves exciton dissociation and electron injection processes from the semiconducting polymer to the nanocrystals as a result of a finely dispersed nanomorphology. However, we have observed that NC-NC interactions can be hindered when using P3HT-SH, possibly due to an excessive covering of their surface by the thiol-functionalized block copolymer. We have shown this can be overcome by employing ternary blends of P3HT, P3HT-SH and bismuth sulfide. On top of improved morphology, devices based on ternary blends also benefit from further improved charge transfer compared to regioregular P3HT, possibly through the formation of an energy cascade that opposes back recombination.

After careful optimization of the device processing conditions, 15% higher power conversion efficiencies were obtained employing a ternary blend consisting of Bi_2S_3:P3HT-SH:P3HT as a result of the improved nanomorphology and higher open-circuit voltages due to deeper energy levels. Further efficiency improvements can be expected if functional groups can be incorporated in novel semiconductor polymers with deeper HOMO levels, such as PCPDTBT or PTB7. Additional improvements can be made by employing functionalized hetero-block copolymers where each block is only responsible and optimized for the roles of charge dissociation or charge transport.

Chapter 5

All-inorganic solution processed photovoltaics based on bismuth sulfide nanocrystals

High-performing solution-processed inorganic thin-film solar cells consist of either nanocrystalline bulk semiconductors or nanocrystalline quantum-confined systems. Examples of nanocrystalline bulk semiconductors are copper indium gallium selenide (CIGS) [107] or copper zinc tin sulfide (CZTS) [78]. Examples of quantum-confined systems are Pb(S,Se) [41, 108, 109] and Cd(Se,S,Te) [110] quantum dots. Quantum dots have been exploited as solar harnessing materials due to the simplicity of bandgap tuning via modification of the nanoparticle size [111]. The number of materials reported corresponds to only a fraction of the available semiconductor materials that could be exploited for the development of third-generation thin-film solar cells. This is primarily due to the short carrier lifetime of most nanocrystalline semiconductors, which is not long enough to allow efficient carrier extraction before recombination. In the case of solution-processed quantum dot devices, Pb(S,Se) quantum dots outperform any other material investigated to date, due to the long carrier lifetime enabled by favourably shallow traps [112]. Quantum confined lead sulfide is a *p*-type semiconductor, mainly employed for solar harnessing in conjunction with large bandgap *n*-type semiconductors such as TiO_2 and ZnO.

5.1 Bilayer heterojunction devices

Bismuth sulfide can be employed as the n-type material in PbS-based solution processed solar cells due to its high electron concentration. Compared to the widely employed large bandgap n-type semiconductors, bismuth sulfide nanocrystals offer the potential to harness the VIS-NIR portion of the solar spectrum employing room temperature fabrication methods.

A cross-sectional scanning electron microscopy picture of a planar heterojunction device based on PbS (bandgap of 1.42 eV) and Bi_2S_3 is presented in Figure 5.1(a). The different layers employed are depicted in the schematic representation provided in Figure 5.1(b) for clarity. The band alignment at the interface between $p-$type PbS QDs and $n-$type Bi_2S_3 nanocrystals (Figure 5.1(c)) allows the formation of a built-in field that drives photogenerated electrons to the $n-$type Bi_2S_3 and holes to the $p-$type PbS QDs.

Current-voltage measurements of a PbS-Bi_2S_3 bilayer heterojunction device are presented in Figure 5.2(a), demonstrating a power conversion efficiency of 1.62%. Figure 5.2(b) shows that similar open-circuit voltage levels ($V_{oc} \approx 0.45$V) are obtained employing the inverted configuration (i.e. ITO/Bi_2S_3/PbS/Au) which suggests that its origin is determined by the Fermi level difference between the two semiconductors and it is not driven by the metals employed as collecting electrodes. Normal structures (i.e. ITO/PbS/Bi_2S_3/Ag) show higher short-circuit currents as a result of higher EQEs, especially at short wavelengths (Figure 5.2(c)). Short-wavelength photons of $400-500$ nm are mainly absorbed in the first layer of the solar cell, which is in PbS for normal structures and Bi_2S_3 for inverted structures, due to the high absorption coefficient of both semiconductors at visible wavelengths [57]. As will be discussed later, Bi_2S_3 has a much shorter depletion width (≈ 60 nm compared to ≈ 140 nm for PbS) as a result of higher carrier concentration. Therefore photogenerated carriers near the ITO side are more efficiently extracted in the case of PbS due to its larger depletion width.

So far we have discussed the employment of Bi_2S_3 as the n-type material to form a heterojunction with p-type PbS QDs. Since both Bi_2S_3 NCs and the PbS QDs employed are strong absorbers in the VIS-NIR region, the active role of Bi_2S_3 in photogeneration of carriers is still unclear. We have incorporated Bi_2S_3 NCs together with PbS QDs with first exciton peak at ≈ 650 nm in order to demonstrate the two-fold role of Bi_2S_3 (i.e. to form a p-n junction while efficiently contributing to the overall photocurrent). Figure 5.3 shows the spectral photoresponse of a planar heterojunction device employing PbS with an exciton peak at $\lambda \approx 650$ nm and Bi_2S_3 along with the absorption spectra of both semiconductors. From photoresponse spectra there are two clear regions. In the region $400 < \lambda < 700$ nm, both materials absorb while at $700 < \lambda < 950$ nm,

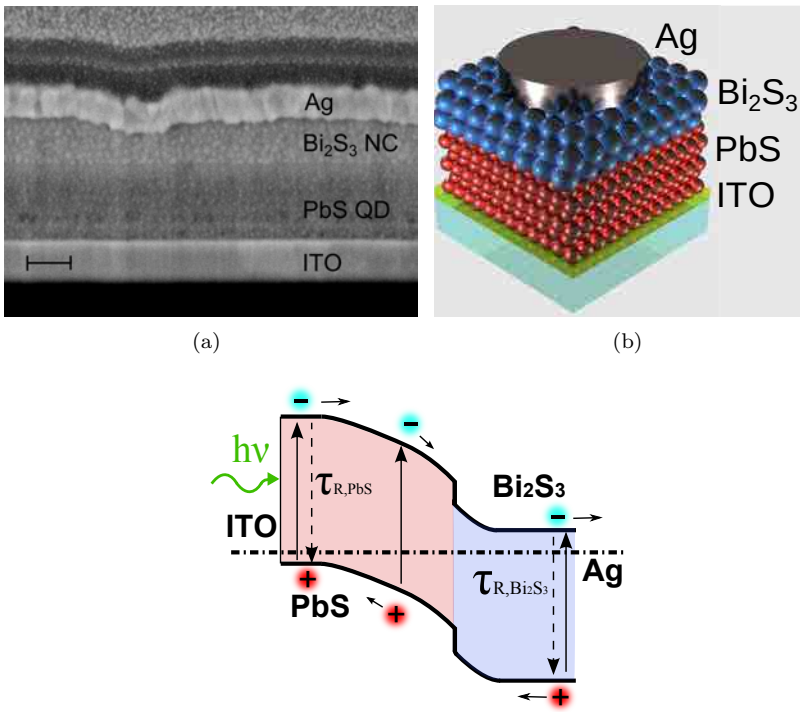

Figure 5.1: Bilayer heterojunctunction devices based on Bi_2S_3 NCs and PbS QDs. (a) Cross-sectional scanning electron microscopy image of the planar heterojunction device (b) schematic for the junction (c) band diagram of the PbS-Bi_2S_3 bilayer *p-n* junction.

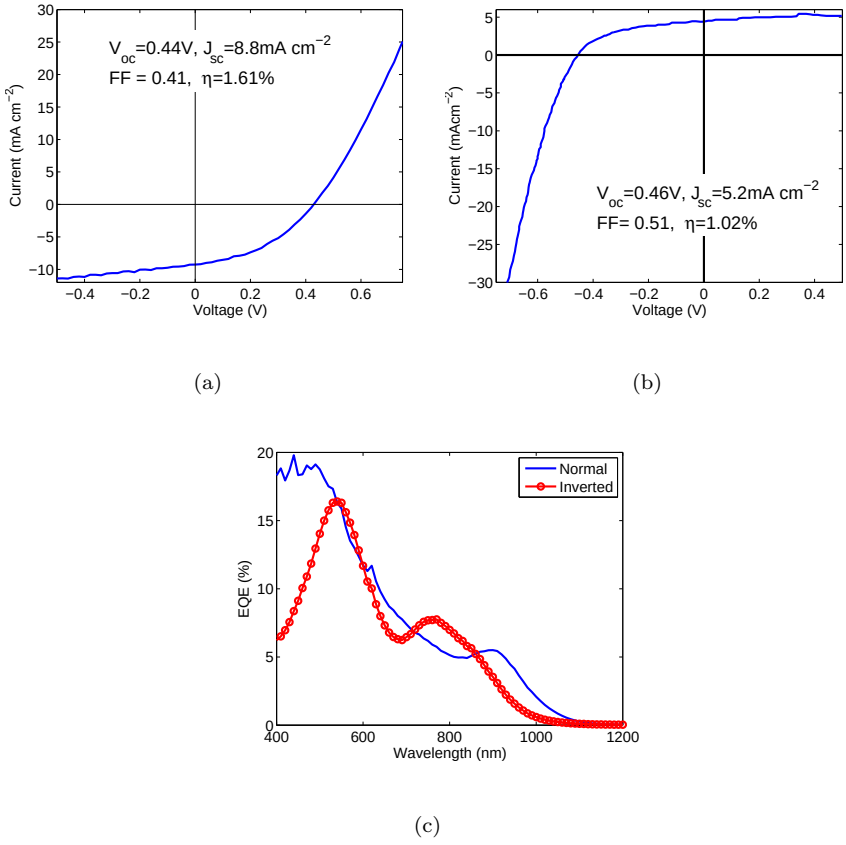

Figure 5.2: Electrical characteristics of PbS/Bi_2S_3 bilayer devices. Current-voltage characteristics of the Bi_2S_3-PbS bilayer *p-n* junction in (a) normal and (b) inverted architectures. (c) External Quantum Efficiency (EQE) of a bilayer device employing Bi_2S_3 and PbS quantum dots in normal (blue solid line) and inverted (red line with circles) configuration.

Bi_2S_3 is the only absorbing material. From this, it is clear that responsivity extends beyond PbS absorption, demonstrating the two-fold role of Bi_2S_3 NCs.

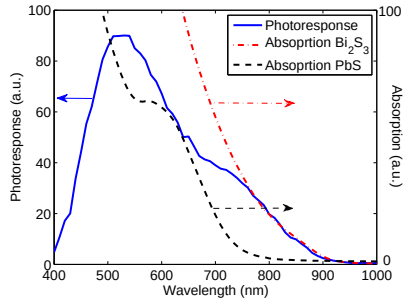

Figure 5.3: External quantum efficiency of a planar heterojunction device based on PbS QDs (exciton peak $\approx$ 650 nm) and Bi_2S_3 NCs.

The formation of a built-in potential and the depletion width can be estimated using capacitance-voltage measurements (C-V). Two sets of samples with constant PbS and varying Bi_2S_3 thickness and viceversa were fabricated to investigate the fundamental limitations of the planar heterojunction structure. Their EQE and C-V performances are presented in Fig. 5.4. Keeping Bi_2S_3 thickness constant, and employing different thickness of PbS, we expect to see a saturation of the capacitance under reverse bias as the device becomes fully depleted (film thickness smaller than or equal to the depletion width) as has been previously observed in similar devices [58]. The dependence of the capacitance on the PbS thickness suggests that the PbS layer is fully-depleted near 140 nm, since a progressive saturation of capacitance for increasing thickness of the PbS layer beyond 140 nm can be observed (Figure 5.4(b)). Extraction of short wavelength photons also becomes less efficient beyond 140 nm PbS thickness as evidenced by the EQE in this wavelength regime, shown in Figure 5.4(a). From structures with constant PbS thickness of 105 nm and varying Bi_2S_3 thickness, the capacitance of the structures remains constant for thicknesses beyond $\approx$ 60 nm (Figure 5.4(d)). This depletion width in Bi_2S_3 nanocrystalline solids is also consistent with the accelerated drop in EQE observed for thicknesses larger than 60 nm shown in Figure 5.4(c). Capacitance-voltage measurements also reveal a built-in field of $V_{bi} \approx 0.5$V in accordance with the measured $V_{oc} \approx 0.45$V.

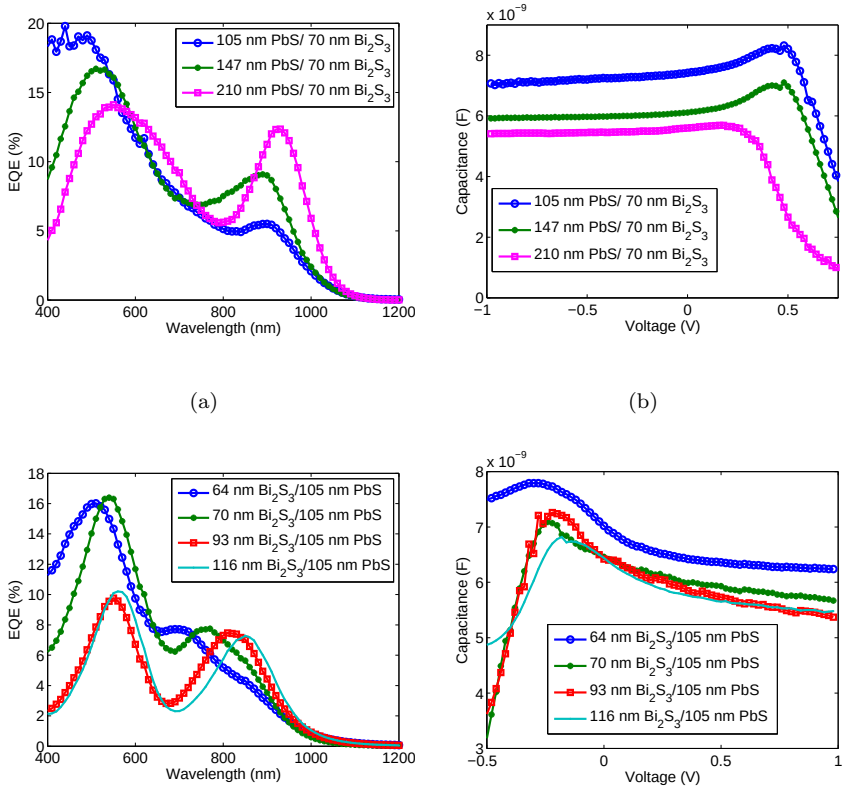

(a) (b)

(c) (d)

Figure 5.4: Spectral EQE and capacitance-voltage characteristics of normal ((a) and (b)) and inverted structures ((c) and (d)) with variable thicknesses of PbS and Bi_2S_3 layers respectively. In normal structures ((a) and (b)) we observe strong suppression of EQE at short wavelengths and saturation of the capacitance for PbS thickness larger than $\approx$ 100 nm whereas in inverted structures these effects occur at Bi_2S_3 thickness larger than 60 nm.

5.2 Bulk heterojunction devices

Lead sulfide quantum dots have been exploited in a variety of solar cell structures where carrier photogeneration and bipolar transport occur in the same medium. Tailoring of PbS carrier mobility and doping concentration has allowed a steady increase in power conversion efficiency from 2% [30] up to 8.5% [109] over recent years. However, to date, this elaborate control of carrier doping has been demonstrated mainly in PbS quantum dots, a well-studied material thanks to its favourably long carrier lifetime.

Bismuth sulfide nanocrystal-based solar cells have been limited due to the short carrier lifetime and diffusion lengths of Bi_2S_3 nanocrystalline solids. The bulk heterojunction architecture has been employed in polymer and hybrid solar cells to overcome similar lifetime and diffusion length limitations. In bulk heterojunction devices, exciton dissociation and diffusion compete favourably with ultrafast recombination and short exciton diffusion length, due to the spatial separation of electrons and holes in the two different media [46]. To expand the range of available materials in the quest for low-cost non-toxic solar cells, we posited we would first have to develop an analogous architecture, employing all-inorganic solution-processed semiconductors. Bismuth sulfide nanocrystals blended with PbS QDs could also benefit from the prolonged carrier lifetimes offered by the bulk heterojunction structure. The success of this platform could pave the way for employing novel nanocrystalline materials with shorter carrier lifetimes.

Figure 5.5(a) presents a schematic of the bulk nano heterojunction (BNH) consisting of a nanocomposite of PbS quantum dots and Bi_2S_3 nanocrystals at a 1 : 2 vol. ratio. The motivation for employing this ratio with be discussed later. The BNH is sandwiched between a hole-blocking layer of neat Bi_2S_3 nanocrystals and an electron-blocking layer of PbS quantum dots. A cross-sectional scanning electron microscopy (SEM) images of the device is shown in Figure 5.5(b), revealing the three different layers employed: a bottom layer of PbS quantum dots, an intermediate layer of nanocomposite and a top layer of Bi_2S_3 nanocrystals. The bilayer structure is based on the formation of a $p-n$ junction at the distinct interface of the materials [57], while the BNH device is based on a distributed dissociating interface throughout the active layer as sketched in Figure 5.6.

The current-voltage characteristics of the bulk and bilayer heterojunction devices under AM1.5 simulated intensity are shown in Figure 5.7(a). The bulk heterojunction devices show a short-circuit current density (J_{sc}) in excess of 24 $mAcm^{-2}$, representing a more than three-fold improvement over the bilayer devices. The resultant PCE of the best-performing bulk heterojunction device is 4.87%. Figure 5.7(b) presents the external quantum efficiency of the bulk and

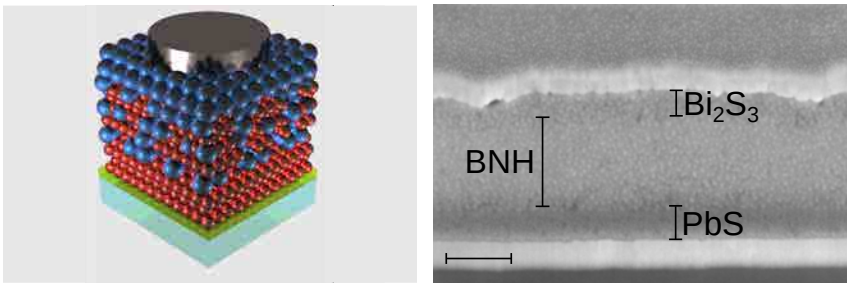

(a) (b)

Figure 5.5: 5.5(a) Schematic of BNH device structure consisting of ITO/PbS quantum dots/PbS:Bi_2S_3 nanocomposite layer/Bi_2S_3 nanocrystals/Ag layers. 5.5(b) Cross-sectional SEM image. Scale bar: 200 nm.

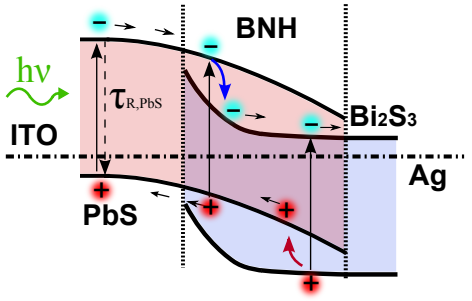

Figure 5.6: Band alignment in bulk heterojunction solar cells based on a PbS:Bi_2S_3 blend.

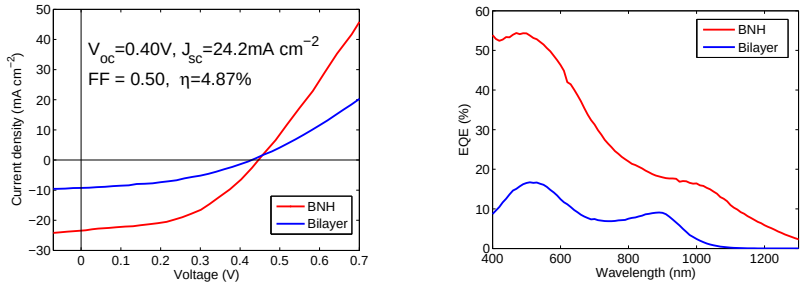

(a) (b)

Figure 5.7: Solar cell characterization of bilayer and BNH devices. (a) IV characteristics under AM1.5 illumination for the BNH (red line) and bilayer (blue line) devices. The BNH figures of merit are also provided. (b) EQE of a bilayer device (blue line) and BNH device (red line).

planar heterojunction devices. EQE improvement correlates with the observed increase in J_{sc} for the BNH device, showing an over three-fold increase.

To elucidate the origins of the efficiency improvement, we measured the carrier lifetime in both BNH and bilayer devices. We employed the transient photovoltage method at various illumination intensities at a wavelength of 630 nm (Figure 5.8(a)). Although both devices show long lifetimes at low intensity, at higher intensities the bilayer device shows a pronounced reduction of the carrier lifetime as previously reported in PbS quantum dot-based solar cells [29, 113]. The bulk heterojunction device on the other hand exhibits longer carrier lifetimes at high illumination intensities. At a power equivalent to one-Sun, the BNH device has a carrier lifetime three times longer than that of the bilayer device. Further evidence of carrier lifetime prolongation in the BNH structures was also provided by all-optical measurements. We monitored the photoluminescence lifetime in neat PbS, Bi_2S_3 and blends of different concentrations as shown in Figure 5.8(b). Carrier lifetime increases for different ratios of PbS:Bi_2S_3, up to a maximum of 35 ns at a 1 : 2 ratio.

5.3 Summary

In this Chapter we have demonstrated that bismuth sulfide colloidal nanocrystals serve a two-fold role in *p*-*n* junction devices with *p*-type PbS quantum dots. The relative Fermi level difference between Bi_2S_3 and PbS allows the formation

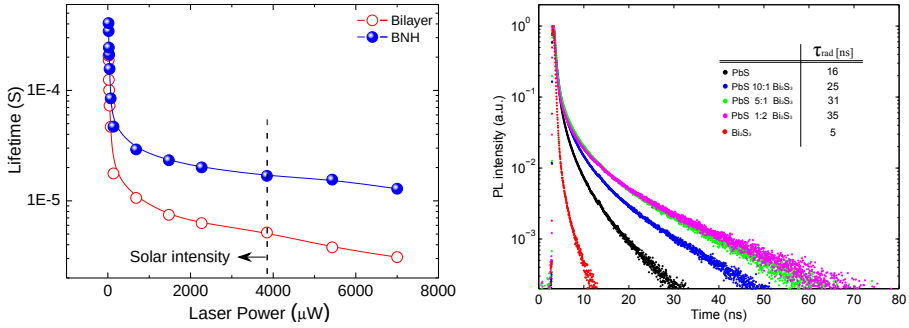

Figure 5.8: Carrier lifetime in BNH devices. (a) Carrier lifetime dependence on illumination intensity at a wavelength of 635 nm for a control bilayer and a BNH device. The BNH device demonstrates a longer carrier lifetime than the bilayer device due to recombination inhibition in the BNH. (b) Photoluminescence dynamics of PbS, Bi_2S_3 and three different BNH device ($10:1$, $5:1$ and $1:2$ PbS to Bi_2S_3 ratio) normalized to their maximum values. The inset table shows the extracted values of the lifetimes from the curves.

of built-in potential across the *p*-*n* junction; and bismuth sulfide nanocrystals contribute to the overall photogeneration of carriers.

We have developed the first inorganic solution-processed bulk nanoheterojunction-based solar cells. This architecture takes advantage of the common surface chemistry between bismuth sulfide nanocrystals and lead sulfide quantum dots and allows nanoscale charge separation into the preferred media of photogenerated carriers. Bulk heterojunction devices based on bismuth sulfide NCs and PbS QDs showed a three-fold increase in carrier lifetime compared to the bilayer counterpart. The increase in carrier lifetime correlates with the three-fold increase in power conversion efficiency observed in photovoltaic devices. This increase is mainly achieved from an increased short-circuit current density. We have shown that the BNH architecture has the potential to relax requirements for long carrier lifetimes, which have limited the exploration of novel nanocrystalline materials.

Summary

The work presented in this thesis demonstrates the employment of n-type bismuth sulfide colloidal nanocrystals as photoactive materials in solar cells in a variety of technological platforms and device architectures. It also shows the potential of this technology to be employed as electron accepting materials in hybrid organic-inorganic solar cells based on the state-of-the-art semiconducting polymers. The use of bismuth sulfide nanocrystals can extend the sensitivity range of these hybrid solar cells into near infrared wavelengths. Due to the advent of colloidal bismuth sulfide nanocrystals, an all-inorganic solution-processed bulk nano heterojunction solar cell has been be achieved for the first time. This architecture loosens the carrier lifetime requirement for the semiconductors to be employed, via charge separation into distinct media at the nanoscale.

Bismuth sulfide nanocrystals were characterized from the structural, chemical and physical points of view. The nanocrystals are highly crystalline and have the appropriate bandgap for single-junction solar harnessing along with high extinction coefficient. The energy levels of the conduction and valence band edges allow for a favourable type-II heterojuncion with most of the best-performing materials investigated for third-generation photovoltaics. We have observed that colloidal bismuth sulfide nanocrystals maintain the electron-rich behaviour typical of metal chalcogenide materials with excess metal, even after exposure to oxygen and moisture. We have identified the low electron mobility and short carrier lifetime as two possible limiting mechanisms on the thickness of the nanocrystalline bismuth sulfide active layer, thus limiting the absorption of the incident light. We have also observed high electron density levels in colloidal bismuth sulfide nanocrystals, which imply a short depletion region that ultimately limits the active layer thickness.

Semiconducting polymers such as P3HT, have a large bandgap and therefore are unable to harness NIR photons. By combining P3HT with Bi_2S_3 NCs we were able to extend the photocurrent generation into NIR wavelengths. Planar heterojunction devices were reported with modest power conversion effi-

ciencies, which were found to be limited by the short exciton diffusion length in P3HT, the short carrier diffusion length in bismuth sulfide nanocrystalline solids and dissimilar carrier mobilities. The short exciton and short carrier diffusion lengths were greatly overcome by developing a hybrid organic-inorganic bulk heterojunction architecture with a larger donor-acceptor interface. This in turn allowed for thicker photovoltaic devices, providing for almost complete absorption of the incoming light. These devices were limited by the low operating voltages, low carrier mobilities and by the agglomerated nanomorphology. We have investigated novel semiconducting polymers with deeper HOMO level to overcome the low open-circuit voltages obtained with P3HT. Despite providing for larger V_{oc}, the performance of planar heterojunction devices based on these novel polymers still remains modest. Moreover, some of these novel polymers are not readily miscible with colloidal bismuth sulfide nanocrystals, which inhibits the development of hybrid bulk heterojunctions.

We have shown that hybrid bulk heterojunctions do not need to rely on the random formation of nanodomains. Incorporation of a thiol functional group in the polymer chain close to the polymer backbone allows for nanomorphologies with much smaller domain sizes without detriment to the optoelectronic properties of the semiconducting polymer. At the same time, this improved morphology increases the exciton dissociation efficiency and electron injection into the bismuth sulfide nanocrystals. Photovoltaic devices based on this thiol-functionalized bloc copolymer exhibit 15% higher power conversion efficiencies compared to P3HT, as a result of larger V_{oc} and FF and slightly lower J_{sc}.

Bismuth sulfide nanocrystals can also be employed with high-performing lead sulfide quantum dots, to form a *p*-*n* junction where both phases contribute to the overall photocurrent. The common surface chemistry between these two nanomaterials allowed the fabrication of the first all-inorganic bulk heterojunction device. This platform reduces recombination via spatial separation of electrons and holes into different media, prolonging the carrier lifetime. The bulk nano heterojunction opens the possibility to explore new semiconductors with shorter carrier lifetimes as materials for third-generation photovoltaics.

Outlook

The field of solution-processed solar cells based on colloidal nanocrystals, and particularly quantum dots, has experienced a rapid progress over the last decade. Power conversion efficiencies have steadily increased up to 8.5% [109] as a result of elaborate control over carrier density and mobility. In particular, surface trap passivation schemes based on metal halides have provided for a major efficiency breakthrough [22, 59]. Major enhancement of photovoltaic performance in sys-

tems based on bismuth sulfide nanocrystalline solids can be expected if interface trap states can also be effectively passivated. This would allow the formation of thicker active layers, increased optical absorption and improved charge extraction. The latter can also benefit from reduced electron densities employing controlled doping strategies. This would in turn extend the depletion region in the bismuth sulfide nanocrystalline film, also allowing for a more efficient solar harnessing.

List of publications

This thesis has led to the publication of the following research articles:

Martinez, L., Bernechea, M., de Arquer, F.P.G., and Konstantatos, G. Near IR-Sensitive, Non-toxic, Polymer/Nanocrystal Solar Cells Employing Bi2S3 as the Electron Acceptor. *Advanced Energy Materials*, 1(6), 10291035, 2011.

Martinez, L., Stavrinadis, A., Higuchi, S., Diedenhofen, S. L., Bernechea, M., Tajima, K., and Konstantatos, G. Hybrid solution-processed bulk heterojunction solar cells based on bismuth sulfide nanocrystals. *Physical Chemistry Chemical Physics: PCCP*, (15), 54825487, 2013.

Martinez, L., Higuchi, S., MacLachlan, A.J., Stavrinadis, A., Miller, N.C., Diedenhofen, S. L., BernecheaM., Sweetnam, S., Nelson, J., Haque, S.A., Tajima, K., and and Konstantatos, G. Improved electronic coupling in hybrid organic-inorganic nanocomposites employing thiol-functionalized P3HT and non-toxic bismuth sulfide nanocrystals. *Nanoscale*, submitted

Rath, A.K., Bernechea, M., **Martinez, L.**, and Konstantatos, G. Solution-Processed Heterojunction Solar Cells Based on p-type PbS Quantum Dots and n-type Bi2S3 Nanocrystals. *Advanced Materials*, 23, 37123717, 2011.

Rath, A.K., Bernechea, M., **Martinez, L.**, de Arquer, F.P.G., Osmond, J., and Konstantatos, G. Solution-processed inorganic bulk nano-heterojunctions and their application to solar cells. *Nature Photonics*, 6, 529534, 2012.

This research has also lead to filing of the patent:

Konstantatos, G., Rath, A.K., Bernechea, M., **Martinez, L**. Solution processed inorganic bulk nano-heterojunctions: tailoring carrier lifetime and doping and their application to solar cells, 2011. *US patent application 13/442,080.*

Other publications by the author:

Stavrinadis, A., Rath, A.K., de Arquer, F.P.G., Diedenhofen, S.L., Magn, C., **Martinez, L.**, So, D., and Konstantatos, G. Heterovalent cation substitutional

doping for quantum dot homojunction solar cells. *Nature Communications*, 4, 2981, 2013.

Ghosh, D. S., **Martinez, L.**, Giurgola, S., Vergani, P., and Pruneri, V. (2009). Widely transparent electrodes based on ultrathin metals. *Optics Letters*, 34(3), 3257.

Martinez, L., Ghosh, D. S., Giurgola, S., Vergani, P., and Pruneri, V. Stable transparent Ni electrodes. *Optical Materials*, 31, 11151117, 2009.

Giurgola, S., Rodriguez, A., **Martinez, L.**, Vergani, P., Lucchi, F., Benchabane, S., and Pruneri, V. Ultra thin nickel transparent electrodes. *Journal of Materials Science: Materials in Electronics*, 20(S1), 181184, 2007.

Other patents by the author:

Pruneri, V., **Martinez, L.**, Giurgola, S., and Vergani, P. Method to prepare a stable transparent electrode, 2009. *European Patent EP 2133921 B1.*

Appendix A

Experimental

A.1 Material characterization

The structural characterization of the synthesized nanoparticles was performed at CCiT-UB laboratories. Transmission electron microscopy measurements (TEM) were performed using a JEOL J2100 microscope operating at an accelerating voltage of 200 kV. The samples were prepared by placing two drops of a diluted Bi_2S_3 in toluene solution on a holey-carbon-coated grid and allowing the solvent to evaporate in air.

X-Ray Diffraction (XRD) measurements were carried out using a PANalytical X'Pert PRO MPD powder diffractometer with a θ/θ goniometer of 240 millimetres of radius, Ni filtered Cu $K\alpha$ radiation: $\lambda = 1.5418\ \mathring{A}$ and work power: 45 kV - 40 mA. The sample was prepared by covering a glass (approximately of 25 mm x 10 mm area) with a toluene solution of oleate-caped-Bi_2S_3 nanoparticles and allowing it to evaporate in air. The process was repeated three times.

XPS experiments were performed in a PHI 5500 Multitechnique System (from Physical Electronics) with a monochromatic X-ray source (Aluminium Kalfa line of 1486.6 eV energy and 350 W), placed perpendicular to the analyzer axis and calibrated using the $3d5/2$ line of Ag with a full width at half maximum (FWHM) of 0.8 eV. The analyzed area was a circle of 0.8 mm diameter, and the selected resolution for the spectra was 187.5 eV of Pass Energy and 0.8 eV step-1 for the general spectra and 23.5 eV of Pass Energy and 0.1 eV step-1 for the spectra of the Bi_2S_3.

UPS measurements were performed with a Phoibos 150 analyzer (SPECS GmbH) in ultra-high vacuum conditions (base pressure 1×10^{-10} mbar) using a monochromatic HeI UV source (21.2 1eV). Measurements of the position of the Fermi level

were done by applying an external -5 V electrical bias to the sample and monitored the cut-off region of the binding energy spectra. Then, the Fermi level was calculated as $E_F = 21.21\text{eV} - E_B - 5\text{eV}$.

Cyclic-voltammetry measurements were performed in 0.1 M tetrabutylammonium perchlorate in acetonitrile solution using a CH instruments electrochemical workstation system. We employed a standard three electrode electrochemical cell. We dispensed 5 μL of a 10 gL^{-1} polymer in chloroform solution onto a platinum working electrode and let the solvent evaporate. Silver/silver nitrate 0.1 M in acetonitrile reference and platinum wire counter electrodes were calibrated against ferrocene as an internal reference of the system (0.64 V vs Standard Hydrogen Electrode - SHE). The scan range was set to -2 to 2 V and scan speed was set to 0.1 V/s. Energy levels with respect to vacuum energy were calculated from the potential of the standard hydrogen electrode ($SHE = 4.44$ eV) [114].

A.2 Device fabrication

A.2.1 FET fabrication

A thin layer (≈ 60 nm) of bismuth sulfide nanocrystals or semiconducting polymer was deposited on top of thermally grown silica layer on a silicon substrate. Some of the materials were annealed as reported in literature. Then, source and drain silver (gold in the case of polymer FETs) electrodes were evaporated on top of the nanocrystal film through a shadow mask (purchased from Ossila) defining a channel of 10 μm long and 1 mm wide. Current-voltage characteristics were obtained in an Agilent B1500A semiconductor parameter analyzer. Carrier mobilities were calculated from the slope of the transconductance according to the following expression [21]:

$$\mu = \frac{L \frac{\partial I_{ds}}{\partial V_{gs}}}{W C_i V_{ds}} \tag{A.1}$$

Where L and W stand for the channel length and width, respectively, V_{ds} is the drain-source voltage applied and C_i is the capacitance per unit area of the insulator (17 nFcm^{-2} [62]).

A.2.2 Solar cell fabrication

Unless otherwise stated ITO-coated glass substrates were first washed in acetone for 10 minutes followed by 10 minutes bath in ethanol, both under strong

sonication. The substrates were then rinsed with abundant DI water and dried with nitrogen.

Hybrid bilayer heterojunction

A layer of Bi_2S_3 NCs in toluene at a concentration of 20 mgmL^{-1} is spincasted on top of ITO-coated glass at 2000 rpm. The original insulating capping ligand (oleic acid) was replaced by a shorter bidentate molecule (1,2-Ethanedithiol also referred as EDT) via the layer-by-layer (LBL) fashion, using a 2% vol. solution in acetonitrile. Then, the unreacted ligands were removed with a flush of acetonitrile. Finally, the un-exchanged nanocrystals were removed using a toluene flush. This processes yielded an approximately 20 nm thick film. The desired film thickness was achieved via subsequent repetitions of the LBL process. Next, a P3HT solution in 1,2-Dichlorobenzene at 50 mgmL^{-1} was deposited on top of the NCs, also by spincoating. The devices were then annealed at 100°C for 15 minutes and the metal electrode (typically silver or molybdenum oxide/silver) was thermally evaporated.

Hybrid bulk heterojunction

Electron transport layers were made either of Bi_2S_3 NCs or ZnO. The former were grown using the aforementioned layer-by-layer fashion. ZnO films were obtained through a sol-gel method. Briefly, 1 g of zinc acetate dihydrate was dispersed in 10 mL of methoxyethanol and 254 μL of ethanolamine. The solution was left under vigorous stirring for at least 4 hours. Then, the solution was dispensed onto ITO-coated substrates and spincasted at 3000 rpm and annealed for 30 minutes at 200°C. This process was done twice in total to achieve a thickness of $\approx$ 50 nm. Bi_2S_3 and P3HT ($M_W = 22000$) were mixed in solution at a concentration of 50 gL^{-1} from individual chloroform solutions and spin-cast at 3000 rpm. The ligand exchange process consisted in a bath of EDT (1% vol.) in ACN for 10 minutes. The substrates were then rinsed in a one-to-one mixture of ACN and ethyl acetate, dried under nitrogen and annealed in air at 110°C for 7 minutes. On some samples, a second layer of Bi_2S_3:P3HT was spin-cast while spinning the substrate, followed by additional 10 minute EDT 1% in ACN bath, rinsing in a 1:1 mixture of ACN and ethyl acetate and 110°C annealing steps (7 minutes). In order to preserve the annealed underlying film, the second active layer was dispensed from a chloroform solution onto a spinning substrate. Next, a drop of P3HT solution in 1,2-dichlorobenzene (DCB) at a concentration of 50 gL^{-1} was deposited onto the spinning (3000 rpm) substrate as the HTL, followed by a last annealing step at 110°C for 7 minutes. Finally, the MoO_3 (15 nm) and Ag (150 nm) electrodes were thermally evaporated in a Kurt J. Lesker Nano36 system.

Hybrid bulk heterojunction based on P3HT-SH

The device structure was ITO/ZnO/BHJ/P3HT/MoO3/Ag, where BHJ is a mixture of Bi_2S_3 nanocrystals and the polymers. We mixed a 50 gL^{-1} chloroform solution regular P3HT with a 50 gL^{-1} solution of thiol-functionalized block copolymer in the same solvent (chloroform), in the desired ratio. The resulting solution was mixed with a 50 gL^{-1} chloroform solution of Bi_2S_3 and stirred overnight. The final mixture was spincasted on top of the ZnO electron transport layer, fabricated using the same sol-gel method discussed above. The active layer was ligand-exchanged in an EDT bath (1% vol.) in acetonitrile for 10 minutes, rinsed in acetonitrile and annealed at 110°C for 7 minutes. Then, a second active layer was spin-cast while spinning the substrate, followed by additional 10 minute EDT 1% in ACN bath, rinsing in ACN and 110°C annealing steps (7 minutes). To complete the device, a thin layer of regioregular P3HT from dichlorobenzene solution was spincasted on top of the active layer as a hole transport layer (HTL) and the top electrode was thermally evaporated.

All-inorganic bulk heterojunctions

Substrates were then dipped in a 0.2 M solution of ethanedithiol (EDT) and (3-mercaptopropyl)methyldimethoxysilane mixed at a ratio of 1 : 1 in toluene for 12 hours to improve adhesion of the nanocrystal layers on the substrates. Oleic acid capped PbS nanocrystals were first ligand-exchanged with oleylamine. PbS stock solution was then prepared at a concentration of 30 gL^{-1} in toluene, Bi_2S_3 stock solution at a concentration of 25 gL^{-1} in toluene, and blends of PbS and Bi_2S_3 were prepared by mixing them at different weight ratios while maintaining a final concentration of 25 gL^{-1} in toluene. Film deposition and ligand exchange were carried out inside a fume hood using a layer-by-layer technique. One drop of nanocrystal was spin-cast at 2000 rpm for 30 s. The film was then treated with two drops of 2% (v/v in acetonitrile) EDT, two drops of acetonitrile and two drops of toluene at the same rotating speed. The sequence was repeated to achieve the desired film thickness. PbS, Bi_2S_3 and EDT solution were spin-cast by passing them through a 0.2 μm filter, but the blend solutions were cast without filtration. The as-synthesized films were kept in vacuum for 48 hours and annealed at 80°C for 10 min inside a glovebox. Metal deposition was carried out on a Kurt J. Lesker Nano 36 system.

A.3 Device characterization

A.3.1 Transient photoluminescence

We employed one layer of bismuth sulfide spincasted onto 200 μm thick glass cover slips and EDT ligand exchanged following the typical device fabrication procedure. Samples are illuminated with 50 ps pulsed laser light at 532 nm, 50 MHz repetition rate and 6 μW of average power. The pump laser is focused at the sample back face through a $100x$ microscope oil immersion objective with 1.46 numerical aperture. The light emitted from the samples is collected via the same microscope objective through dichroic and highpass filters which ensure a detection window of $550 - 1100$ nm and a better than 10^{12} suppression of the pump laser. A confocal technique is used to direct the emitted light from spots of 1.5 μm diameter to the avalanche photodiode. The fluorescence decay profile is reconstructed by time-correlated single-photon counting with an $\approx$ 100 ps response time.

A.3.2 Photoluminescence quenching

Solid-state photoluminescence quenching measurements were performed in a Horiba Jovin-Yvon fluorolog system using an integrating sphere. The samples were illuminated with a 450 nm monochromatic light source. The emission of the samples was normalized to their absorbance at 450 nm, measured using a Cary 5000 UV-VIS-NIR spectrophotometer.

A.3.3 Transient absorption spectroscopy

Transient Absorption Spectroscopy (TAS) measurements were performed by exciting the sample films, under a dynamic nitrogen atmosphere, with the output from an optical parametric oscillator (Oppolette) pumped by the Nd:YAG laser. The pulse widths of the excitations were 20 ns. The excitation wavelengths used were either 700 nm to excite exclusively the Bi_2S_3 nanocrystals or 510 nm to excite both the Bi_2S_3 and the polymer with a frequency of 20 Hz. The laser intensities used were 10 or 13.7 μJcm^{-2}, respectively to keep the approximate number of excitation photons the same for all measurements. All readings were normalized to the samples absorption at the excitation wavelengths. A 100 W quartz halogen lamp (Bentham, IL 1) with a stabilized power supply (Bentham, 605) was used as a probe light source, with a probe wavelength of 1000 nm used. The probe light passing through the sample film was detected with a silicon photodiode (Hamamatsu Photonics, S1722-01). The signal from the photodiode was amplified before passing through electronic band-pass filters

(Costronics Electronics). The amplified signal was collected with a digital oscilloscope (Tektronics, TDS220), which was synchronized with a trigger signal from the pump laser pulse from a photodiode (Thorlabs Inc., DET210). To reduce stray light, scattered light, and sample emission, two monochromators and appropriate optical cut-off filters were placed before and after the sample.

A.3.4 Transient opencircuit voltage

Transient open-circuit voltage measurements were performed via amplitude modulation of a Newport LQA635-08C 635 nm laser, using an Agilent 33220A waveform generator. The time profile was recorded in a Tektronix TDS2024B digital oscilloscope. The very initial slopes of the decays were fit with first order polynomial curves. Finally the carrier lifetimes (τ) were calculated according to the expression:

$$\tau = -\frac{kT}{q}\frac{1}{\frac{dV_{oc}}{dt}} \tag{A.2}$$

Where k is the Boltzman constant, q is the electron charge and T is the room temperature.

A.3.5 Solar cell characterization

Current-voltage characteristics were obtained using a Keithley 2400 source measuring unit under dark and simulated AM1.5 solar conditions (Newport 96000).

External quantum efficiency (EQE) measurements were obtained using a Newport Cornerstone 260 monochromator and a Keithley 2400 source measuring unit providing shortcircuit conditions.

Internal quantum efficiency was calculated from the sample absorption (obtained with a Cary 5000 UV-VIS-NIR spectrophotometer with an integrating sphere) and the calculated EQE.

Shortcircuit current density and open circuit voltage dependence with incident power density measurements were taken using a Keithley 2400 source measuring unit and a Newport LQA635-08C 635 nm laser.

Appendix B

Characterization of the semiconducting polymers

B.1 P3HT

Poly(3-hexylthiophene) or P3HT is considered as the reference polymer in this thesis since it has been the main semiconducting polymer employed in the organic photovoltaic research.

Absorption of regioregular P3HT ($M_W = 22000$) purchased from Rieke Metals is presented in Figure B.1(a). From the optical absorption we calculate an optical bandgap of 1.9 eV. We determine the HOMO level of P3HT (≈ 5.28 eV) through cyclic-voltammetry measurements as shown in Figure B.1(b).

Hole mobility was determined from FET measurements as shown in Figure B.2.

B.2 PTB7

Absorption of poly[[4,8-bis[(2-ethylhexyl)oxy]benzo[1,2-b:4,5-b0]dithiophene-2,6-diyl][3-fluoro-2-[(2-ethylhexyl)carbonyl]- thieno[3,4-b]thiophenediyl]] (PTB7) purchased from 1-Material is presented in Figure B.3(a). From the optical absorption we calculate an optical bandgap of 1.6 eV. We determine the HOMO level of PTB7 (≈ 5.37 eV) through cyclic-voltammetry measurements as shown in Figure B.3(b).

Hole mobility was determined from FET measurements as presented in Figure B.4.

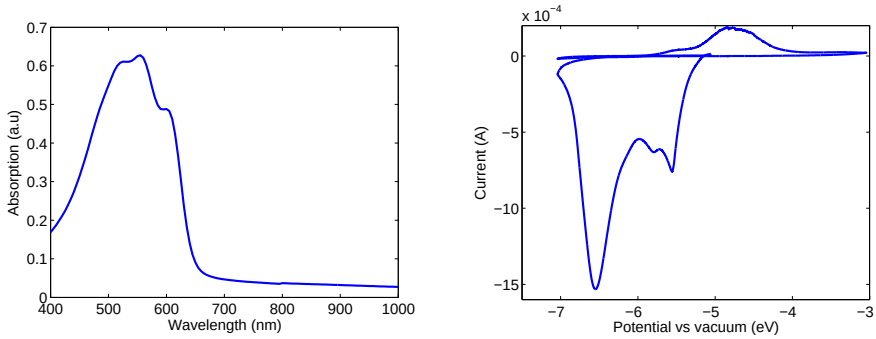

(a) (b)

Figure B.1: Energetic levels of P3HT. (a) Optical absorption of P3HT films (b) Determination of the highest occupied molecular orbital energy level of P3HT films

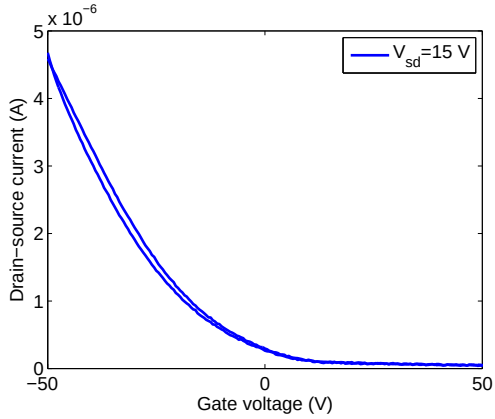

Figure B.2: P3HT field effect transistors transconductance measurements.

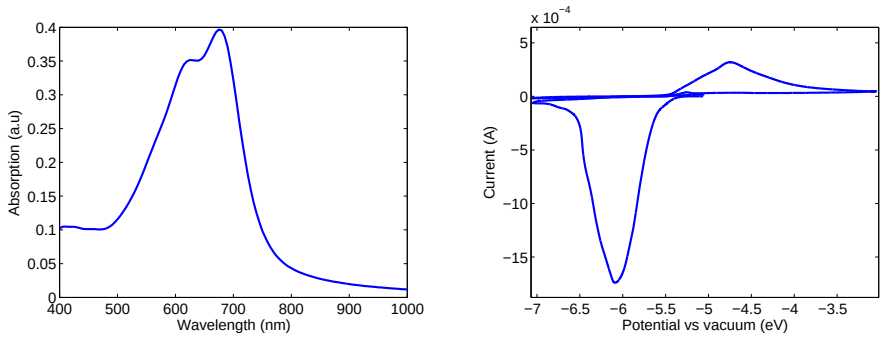

(a) (b)

Figure B.3: Energetic levels of PTB7. (a) Optical absorption of PTB7 films (b) Determination of the highest occupied molecular orbital energy level of PTB7 films

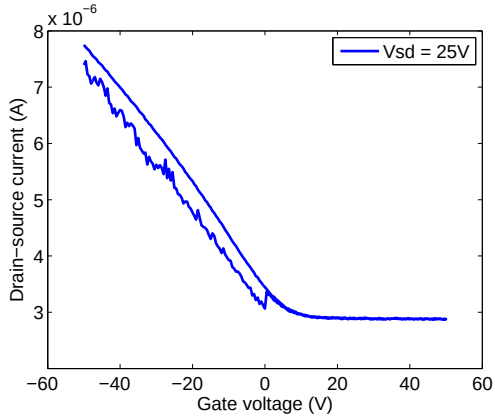

Figure B.4: PTB7 field effect transistors transconductance measurements.

B.3 PCDTBT

Absorption of Poly[N-9-heptadecanyl-2,7-carbazole-alt-5,5-(4,7-di-2-thienyl-2,1,3-benzothiadiazole)] (PCDTBT) purchased from Ossila is presented in Figure B.5(a). From the optical absorption we calculate an optical bandgap of 1.9 eV. We determine the HOMO level of PCDTBT ($\approx$ 5.47 eV) through cyclic-voltammetry measurements as shown in Figure B.5(b).

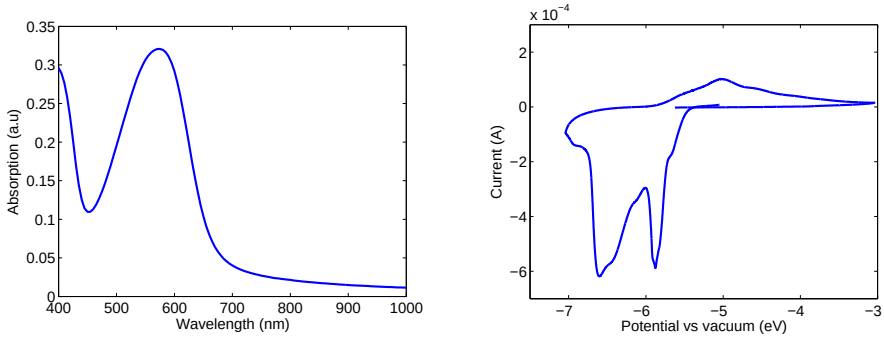

(a) (b)

Figure B.5: Energetic levels of PCDTBT. (a) Optical absorption of PCDTBT films (b) Determination of the highest occupied molecular orbital energy level of PCDTBT films

We attempted to determined hole mobility from FET measurements. However, as shown in Figure B.8, the measured drain-source currents (I_{ds}) could not be distinguished from the leakage currents (I_{gs}) which inhibits the calculation of the hole mobility from the device transconductance.

B.4 PCPDTBT

Absorption of poly[2,6-(4,4-bis-(2-ethylhexyl)-4H-cyclopenta[2,1-b;3,4-b']dithiophene)-alt-4,7-(2,1,3-benzothiadiazole)] (PCPDTBT) purchased from 1-Material is presented in Figure B.7(a). From the optical absorption we calculate an optical bandgap of 1.45 eV. We determine the HOMO level of PCPDTBT ($\approx$ 5.56 eV) through cyclic-voltammetry measurements as shown in Figure B.7(b).

Hole mobility was determined from FET measurements as presented in Figure B.8.

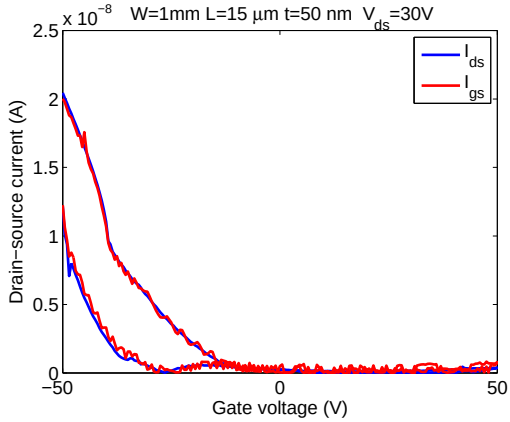

Figure B.6: PCDTBT field effect transistors transconductance measurements.

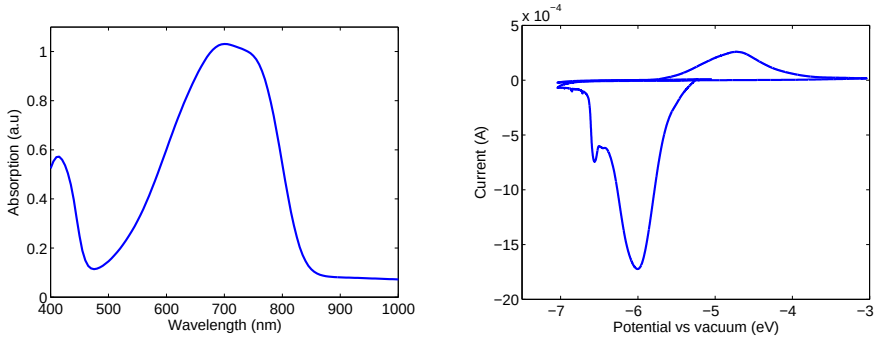

(a) (b)

Figure B.7: Energetic levels of PCPDTBT. (a) Optical absorption of PCPDTBT films (b) Determination of the highest occupied molecular orbital energy level of PCPDTBT films

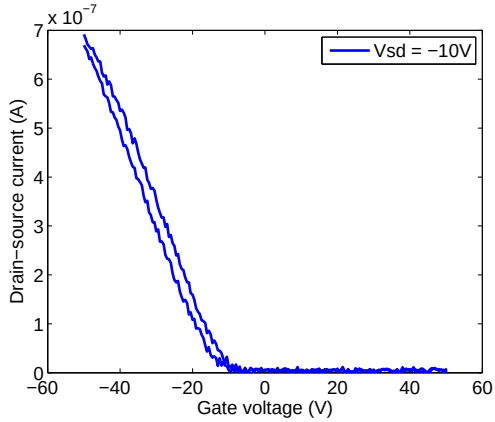

Figure B.8: PCPDTBT field effect transistors transconductance measurements.

B.5 PBDTTT-C

Absorption of poly[(4,8-bis-(2-ethylhexyloxy)-benzo[1,2-b;4,5-b']dithiophene)-2,6-diyl-alt-(4-(2-ethylhexanoyl)-thieno[3,4-b]thiopene)-2,6-diyl] (PBDTTT-C) is presented in Figure B.9(a), revealing an optical bandgap of $\approx$ 1.6 eV. We determine the HOMO level of ($\approx$ 5.66 eV) through cyclic-voltammetry measurements as shown in Figure B.9(b).

Hole mobility was determined from FET measurements as presented in Figure B.10.

B.6 PBDTTPD

Absorption of poly(di(2-ethyl-hexyloxy)benzo[1,2-b:4,5-b]dithiophene-co-octylthieno[3,4-c]pyrrole-4,6-dione) (PBDTTPD) purchased from 1-Material is presented in Figure B.11(a). From the optical absorption we calculate an optical bandgap of 1.7 eV, slightly smaller compared to literature values [69]. We determine the HOMO level of PBDTTPD ($\approx$ 5.75 eV) through cyclic-voltammetry measurements as shown in Figure B.11(b).

Hole mobility was determined from FET measurements as presented in Figure B.12.

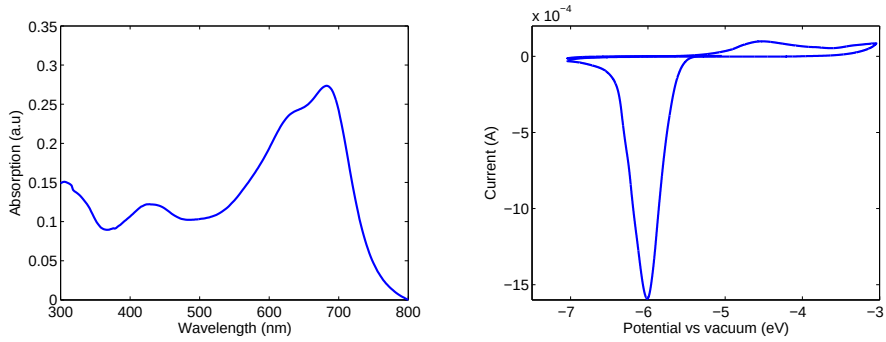

(a) (b)

Figure B.9: Energetic levels of PBDTTT-C. (a) Optical absorption of PBDTTT-C films (b) Determination of the highest occupied molecular orbital energy level of PBDTTT-C films.

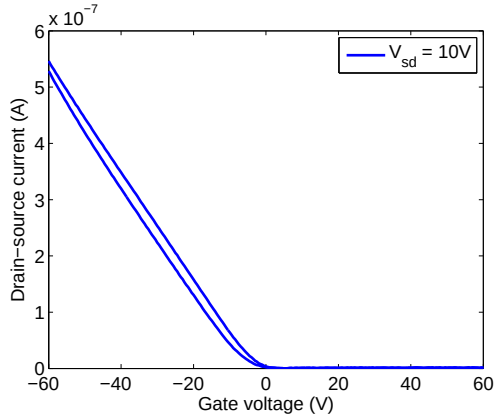

Figure B.10: PBDTTT-C field effect transistors transconductance measurements.

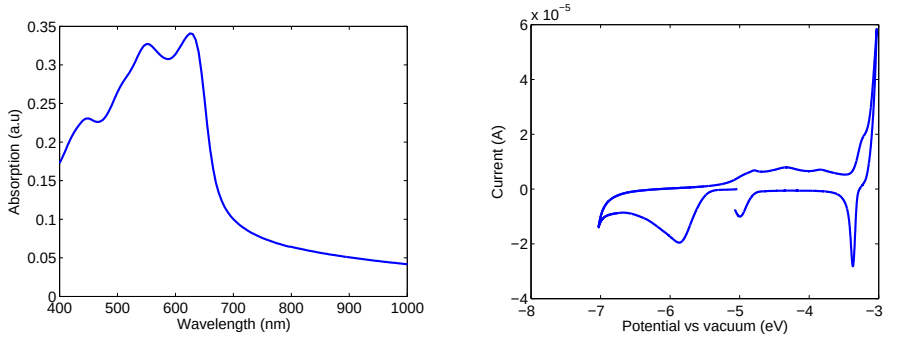

(a) (b)

Figure B.11: Energetic levels of PBDTTPD. (a) Optical absorption of PBDTTPD films (b) Determination of the highest occupied molecular orbital energy level of PBDTTPD films

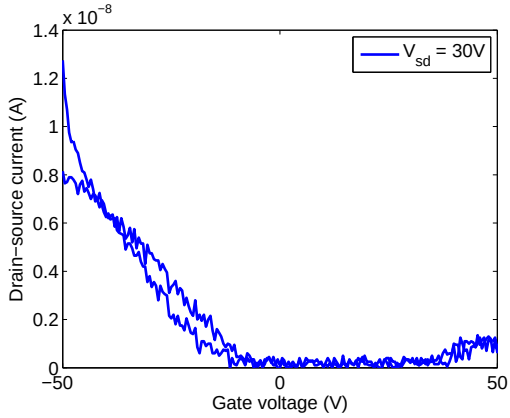

Figure B.12: PBDTTPD field effect transistors transconductance measurements.

Appendix C

Synthesis of the functionalized block copolymer

2-Bromo-3-hexyl-5-iodothiophene was used as received. 2-Bromo-3-hexyl-5-iodo(6-bromohexyl)thiophene was prepared following the previous reports [103]. The thiol-functionalized poly(3-alkylthiophene)-based diblock copolymer was synthesized as shown in Figure C.1. Polymer synthesis relies on the controlled synthesis of regioregular poly(3-alkylthiophene)s by Grignard metathesis (GRIM) method and quasi-living polymerization with Ni(dppp)Cl_2 based on the reports by McCullough et al. and Yokozawa et al [98, 99]. In the first step, the GRIM product of 2-bromo-5-iodo-3-hexylthiophene was polymerized with the Ni catalyst to obtain the P3HT living polymer. The GRIM product of 2-bromo-3-hexyl-5-iodo(6-bromohexyl)thiophene was subsequently added to the living polymer solution to extend the polymer chain by the chain-growth mechanism to form the block copolymer. The chain length in the diblock copolymer (m and n) were controlled by changing the monomer feed ratios.

After the addition of the second monomer, the peak shift to the high molecular weight without the change of the peak shape in the gel permeation chromatography (GPC) chart as shown in Figure C.2, indicating successful block copolymerization. The GPC analysis of all the polymers show that the M_n was around 20000 with a narrow polydispersity (M_w/M_n) of around 1.1. The ratio of 3-hexyl and 3-(6-bromohexyl) side chains in the copolymers were determined by ^{1}H NMR (Figure C.3). After the polymers were purified by washing with 5 M HCl solution [115] and Soxhlet extraction with methanol and hex-

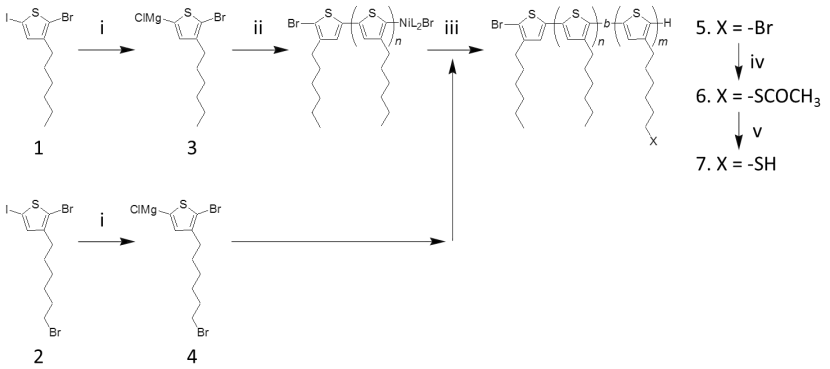

Figure C.1: Synthetic Route for Thiol-functionalized Diblock Copolymers. Reagents and conditions (i)THF, i-PrMgCl, 0°C; (ii)Ni(dppp)Cl2, 40°C; (iii)4, 40°C; (iv)THF, Potassium thioacetate, Reflux; (v)THF, Lithium aluminum hydride, 30°C.

ane, bromide groups in the side chain of the diblock copolymers were converted to thioester groups and subsequently to thiol groups by following the reported procedure [116]. The quantitative conversion was confirmed by the complete disappearance of the peak of the methylene proton peaks next to bromine at 3.42 ppm and the appearance of the methylene proton peaks next to thioester group and thiol group respectively at 2.32 ppm and 2.54 ppm, respectively, in ^{1}H NMR spectra (Figure C.3). P3HT-SH was obtained after the further purification with Soxhlet extraction with methanol and hexane.

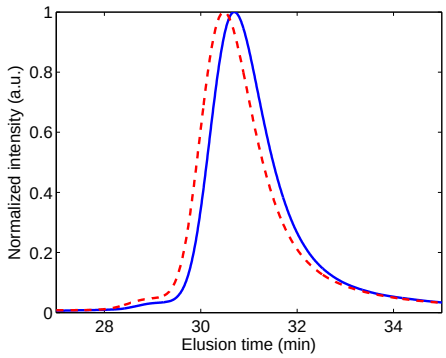

Figure C.2: GPC traces of bromide-functionalized P3HT (solid) and diblock copolymer 6% (dashed).

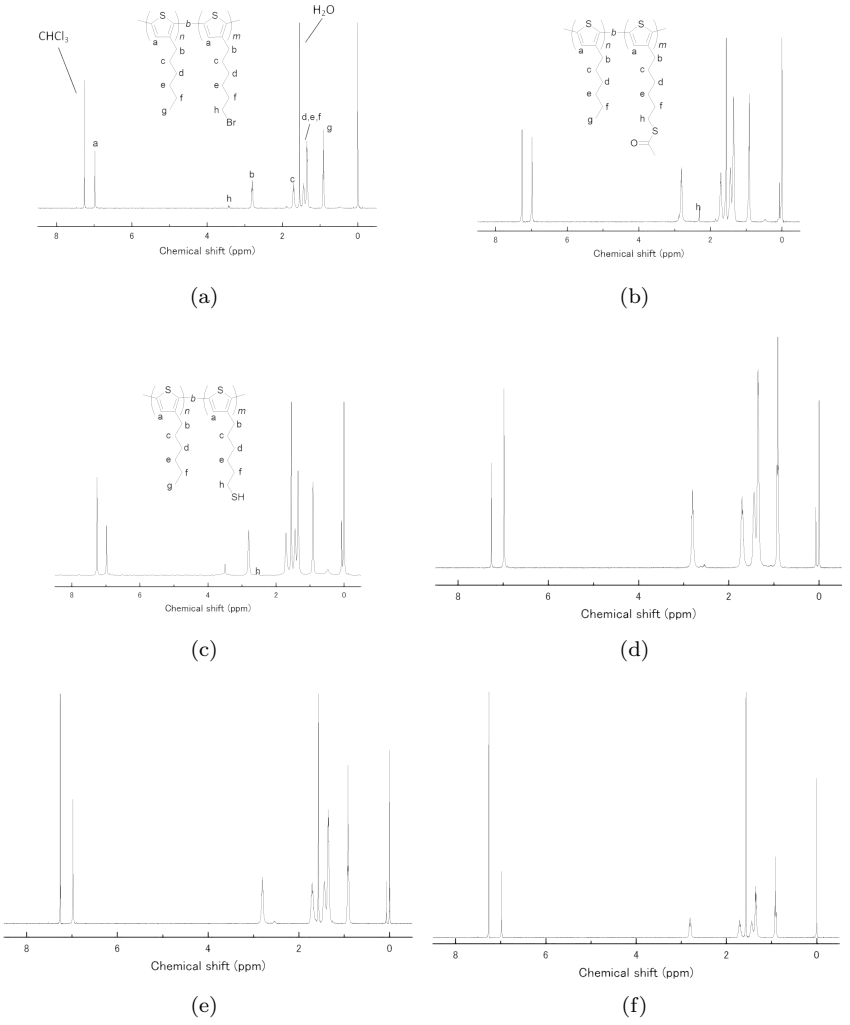

Figure C.3: ^{1}H NMR chart characterization of: (a) polymer 5 (6%) (b) polymer 6 (6%) (c) polymer 7 (6%) (d) diblock copolymer 7 (4%) (e) diblock copolymer 7 (1%) (f) diblock copolymer 7 ($< 1\%$).

Bibliography

[1] W. Hermann, "Quantifying global exergy resources," *Energy*, vol. 31, pp. 1685–1702, Sept. 2006.

[2] G. Legros, I. Havet, N. Bruce, and S. Bonjour, *The energy access situation in developing countries: a review focusing on the Least Developed Countries and Sub-Saharan Africa*. World Health Organization, 2009.

[3] L. Fraas and L. Partain, *Solar cells and their applications*. John Wiley\& Sons, 2010.

[4] S. Nathan, "Basic research needs for solar energy utilization," tech. rep., US Department of Energy, Washington DC, 2005.

[5] B. R. Saunders, "Hybrid polymer/nanoparticle solar cells: preparation, principles and challenges," *Journal of colloid and interface science*, vol. 369, pp. 1–15, Mar. 2012.

[6] A. Mayer, S. Scully, B. Hardin, M. Rowell, and M. D. McGehee, "Polymer-based solar cells," *Materials today*, vol. 10, no. 11, pp. 28–33, 2007.

[7] J. Nelson, *The Physics of Solar Cells*, vol. 50 of *Series on Properties of Semiconductor Materials*. Imperial College Press, 2003.

[8] M. A. Green, K. Emery, Y. Hishikawa, W. Warta, and E. D. Dunlop, "Solar cell efficiency tables (version 39)," *Progress in Photovoltaics: Research and Applications*, vol. 20, pp. 12–20, 2012.

[9] "The chart, Best Research-Cell Efficiencies, is reprinted with permission from the National Renewable Energy Laboratory (NREL), http://www.nrel.gov/ncpv/images/efficiency_chart.jpg, accessed March 28, 2014.,"

[10] D. Chapin, C. Fuller, and G. Pearson, "A New Silicon p-n Junction Photocell for Converting Solar Radiation into Electrical Power," *Journal of Applied Physics*, vol. 25, no. 5, p. 676, 2004.

[11] C. Wadia, A. P. Alivisatos, and D. M. Kammen, "Materials Availability Expands the Opportunity for Large-Scale Photovoltaics Deployment," *Environmental Science & Technology*, vol. 43, pp. 2072–2077, Mar. 2009.

[12] K. L. Chopra, P. D. Paulson, and V. Dutta, "Thin-film solar cells: an overview," *Progress in Photovoltaics: Research and Applications*, vol. 12, pp. 69–92, Mar. 2004.

[13] M. A. Green, "The future of crystalline silicon solar cells," *Progress in Photovoltaics: Research and Applications*, vol. 8, pp. 127–139, Jan. 2000.

[14] P. W. Blom, V. D. Mihailetchi, L. J. A. Koster, and D. Markov, "Device Physics of Polymer:Fullerene Bulk Heterojunction Solar Cells," *Advanced Materials*, vol. 19, pp. 1551–1566, June 2007.

[15] H. W. Hillhouse and M. C. Beard, "Solar cells from colloidal nanocrystals: Fundamentals, materials, devices, and economics," *Current Opinion in Colloid & Interface Science*, vol. 14, pp. 245–259, Aug. 2009.

[16] E. Bundgaard, O. Hagemann, M. Manceau, M. Jø rgensen, and F. C. Krebs, "Low Band Gap Polymers for Roll-to-Roll Coated Polymer Solar Cells," *Macromolecules*, vol. 43, pp. 8115–8120, Oct. 2010.

[17] P. Nicholson and F. Castro, "Organic photovoltaics: principles and techniques for nanometre scale characterization," *Nanotechnology*, vol. 21, p. 492001, 2010.

[18] J. Y. Kim, K. Lee, N. E. Coates, D. Moses, T.-Q. Nguyen, M. Dante, and A. J. Heeger, "Efficient tandem polymer solar cells fabricated by all-solution processing.," *Science*, vol. 317, pp. 222–225, July 2007.

[19] S. Park, A. Roy, S. Beaupré, S. Cho, N. E. Coates, J. Moon, D. Moses, M. Leclerc, K. Lee, and A. J. Heeger, "Bulk heterojunction solar cells with internal quantum efficiency approaching 100%," *Nature Photonics*, vol. 3, no. 5, pp. 297–302, 2009.

[20] C. J. Brabec, S. Gowrisanker, J. J. M. Halls, D. Laird, S. Jia, and S. P. Williams, "Polymer-fullerene bulk-heterojunction solar cells.," *Advanced Materials*, vol. 22, pp. 3839–3856, Sept. 2010.

[21] D. V. Talapin, J.-S. Lee, M. V. Kovalenko, and E. V. Shevchenko, "Prospects of colloidal nanocrystals for electronic and optoelectronic applications.," *Chemical reviews*, vol. 110, pp. 389–458, Jan. 2010.

[22] J. Tang, K. W. Temp, S. Hoogland, K. S. Jeong, H. Liu, L. Levina, M. Furukawa, X. Wang, R. Debnath, D. Cha, K. Chou, A. Fischer, A. Amassian,

J. B. Asbury, and E. H. Sargent, "Colloidal-quantum-dot photovoltaics using atomic-ligand passivation," *Nature materials*, no. September, pp. 1–7, 2011.

[23] E. Comission, "Second Regulatory Review on Nanomaterials," tech. rep., 2012.

[24] S. Dimas, "DIRECTIVE 2002/95/EC OF THE EUROPEAN PARLIAMENT AND OF THE COUNCIL of 27 January 2003 on the restriction of the use of certain hazardous substances in electrical and electronic equipment," Tech. Rep. 8, 2006.

[25] I. Kramer and E. H. Sargent, "Colloidal Quantum Dot Photovoltaics: A Path Forward.," *ACS nano*, vol. 5, p. 8506, Oct. 2011.

[26] M. Graetzel, R. a. J. Janssen, D. B. Mitzi, and E. H. Sargent, "Materials interface engineering for solution-processed photovoltaics," *Nature*, vol. 488, pp. 304–312, Aug. 2012.

[27] E. H. Sargent, "Colloidal quantum dot solar cells," *Nature Photonics*, vol. 6, no. March, pp. 133–135, 2012.

[28] J. Gao, J. M. Luther, O. E. Semonin, R. J. Ellingson, A. J. Nozik, and M. C. Beard, "Quantum dot size dependent J-V characteristics in heterojunction ZnO/PbS quantum dot solar cells.," *Nano letters*, vol. 11, pp. 1002–8, Mar. 2011.

[29] K. W. Johnston, A. G. Pattantyus-Abraham, J. P. Clifford, S. H. Myrskog, S. Hoogland, H. Shukla, E. J. D. Klem, L. Levina, and E. H. Sargent, "Efficient Schottky-quantum-dot photovoltaics: The roles of depletion, drift, and diffusion," *Applied Physics Letters*, vol. 92, no. 12, p. 122111, 2008.

[30] J. M. Luther, M. Law, M. C. Beard, Q. Song, M. O. Reese, R. J. Ellingson, and A. J. Nozik, "Schottky solar cells based on colloidal nanocrystal films.," *Nano letters*, vol. 8, pp. 3488–92, Oct. 2008.

[31] W. Ma, J. M. Luther, H. Zheng, Y. Wu, and A. P. Alivisatos, "Photovoltaic devices employing ternary PbSxSe1-x nanocrystals.," *Nano letters*, vol. 9, pp. 1699–703, Apr. 2009.

[32] A. G. Pattantyus-Abraham, I. J. Kramer, D. A. R. Barkhouse, X. Wang, G. Konstantatos, R. Debnath, L. Levina, I. Raabe, M. K. Nazeeruddin, M. Grätzel, and E. H. Sargent, "Depleted-heterojunction colloidal quantum dot solar cells.," *ACS nano*, vol. 4, pp. 3374–80, June 2010.

[33] B. Sun, A. T. Findikoglu, M. Sykora, D. J. Werder, and V. I. Klimov, "Hybrid photovoltaics based on semiconductor nanocrystals and amorphous silicon.," *Nano letters*, vol. 9, pp. 1235–41, Mar. 2009.

[34] Y. Wu, C. Wadia, W. Ma, B. Sadtler, and A. P. Alivisatos, "Synthesis and photovoltaic application of copper(I) sulfide nanocrystals.," *Nano letters*, vol. 8, pp. 2551–5, Aug. 2008.

[35] I. E. Anderson, A. J. Breeze, J. D. Olson, L. Yang, Y. Sahoo, and S. A. Carter, "All-inorganic spin-cast nanoparticle solar cells with nonselective electrodes," *Applied Physics Letters*, vol. 94, no. 6, p. 063101, 2009.

[36] C. Steinhagen, M. G. Panthani, V. Akhavan, B. Goodfellow, B. Koo, and B. A. Korgel, "Synthesis of Cu2ZnSnS4 nanocrystals for use in low-cost photovoltaics.," *Journal of the American Chemical Society*, vol. 131, pp. 12554–5, Sept. 2009.

[37] S. Günes, H. Neugebauer, N. S. Sariciftci, J. Roither, M. V. Kovalenko, G. Pillwein, and W. Heiss, "Hybrid Solar Cells Using HgTe Nanocrystals and Nanoporous TiO2 Electrodes," *Advanced Functional Materials*, vol. 16, pp. 1095–1099, May 2006.

[38] S. Gunes, K. P. Fritz, H. Neugebauer, N. S. Sariciftci, S. Kumar, and G. D. Scholes, "Hybrid solar cells using PbS nanoparticles," *Solar Energy Materials and Solar Cells*, vol. 91, pp. 420–423, Mar. 2007.

[39] D. M. N. M. Dissanayake, R. a. Hatton, T. Lutz, C. E. Giusca, R. J. Curry, and S. R. P. Silva, "A PbS nanocrystal-C60 photovoltaic device for infrared light harvesting," *Applied Physics Letters*, vol. 91, no. 13, p. 133506, 2007.

[40] N. C. Greenham, X. Peng, and A. P. Alivisatos, "Charge separation and transport in conjugated-polymer/semiconductor-nanocrystal composites studied by photoluminescence quenching and photoconductivity.," *Physical review. B, Condensed matter*, vol. 54, pp. 17628–17637, Dec. 1996.

[41] S. A. McDonald, G. Konstantatos, S. Zhang, P. W. Cyr, E. J. D. Klem, L. Levina, and E. H. Sargent, "Solution-processed PbS quantum dot infrared photodetectors and photovoltaics.," *Nature materials*, vol. 4, pp. 138–42, Feb. 2005.

[42] D. Cui, J. Xu, T. Zhu, G. Paradee, S. Ashok, and M. Gerhold, "Harvest of near infrared light in PbSe nanocrystal-polymer hybrid photovoltaic cells," *Applied Physics Letters*, vol. 88, no. 18, p. 183111, 2006.

[43] B. Sun, E. Marx, and N. C. Greenham, "Photovoltaic Devices Using Blends of Branched CdSe Nanoparticles and Conjugated Polymers," *Nano Letters*, vol. 3, pp. 961–963, July 2003.

[44] L. Wang, Y. Liu, and X. Jiang, "Enhancement of photovoltaic characteristics using a suitable solvent in hybrid polymer/multiarmed CdS nanorods solar cells," *The Journal of Physical Chemistry C*, vol. 111, pp. 9538–9542, July 2007.

[45] W. J. E. Beek, M. M. Wienk, and R. A. J. Janssen, "Hybrid polymer solar cells based on zinc oxide," *Journal of Materials Chemistry*, vol. 15, no. 29, p. 2985, 2005.

[46] S. D. Oosterhout, M. M. Wienk, S. S. van Bavel, R. Thiedmann, L. J. A. Koster, J. Gilot, J. Loos, V. Schmidt, and R. a. J. Janssen, "The effect of three-dimensional morphology on the efficiency of hybrid polymer solar cells.," *Nature materials*, vol. 8, pp. 818–824, Oct. 2009.

[47] Y.-Y. Lin, T.-H. Chu, S.-S. Li, C.-H. Chuang, C.-H. Chang, W.-F. Su, C.-P. Chang, M.-W. Chu, and C.-W. Chen, "Interfacial nanostructuring on the performance of polymer/TiO2 nanorod bulk heterojunction solar cells.," *Journal of the American Chemical Society*, vol. 131, pp. 3644–9, Mar. 2009.

[48] K. Noone, E. Strein, N. Anderson, P. Wu, S. Jenekhe, and D. Ginger, "Broadband Absorbing Bulk Heterojunction Photovoltaics Using Low-Bandgap Solution-Processed Quantum Dots," *Nano letters*, vol. 10, pp. 2635–2639, June 2010.

[49] Y.-Y. Lin, D.-Y. Wang, H.-C. Yen, H.-L. Chen, C.-C. Chen, C.-M. Chen, C.-Y. Tang, and C.-W. Chen, "Extended red light harvesting in a poly(3-hexylthiophene)/iron disulfide nanocrystal hybrid solar cell," *Nanotechnology*, vol. 20, p. 405207, Oct. 2009.

[50] K. M. Coakley and M. D. McGehee, "Conjugated Polymer Photovoltaic Cells," *Chemistry of Materials*, vol. 16, pp. 4533–4542, Nov. 2004.

[51] A. Mihi, F. J. Beck, T. Lasanta, A. K. Rath, and G. Konstantatos, "Imprinted electrodes for enhanced light trapping in solution processed solar cells.," *Advanced Materials*, vol. 26, pp. 443–8, Jan. 2014.

[52] B. D. Yuhas and P. Yang, "Nanowire-based all-oxide solar cells.," *Journal of the American Chemical Society*, vol. 131, pp. 3756–61, Mar. 2009.

[53] O. Madelung, *Semiconductors: data handbook*. Springer Verlag, 2004.

[54] D. J. Riley, J. P. Waggett, and K. G. U. Wijayantha, "Colloidal bismuth sulfide nanoparticles: a photoelectrochemical study of the relationship between bandgap and particle size," *Journal of Materials Chemistry*, vol. 14, no. 4, p. 704, 2004.

[55] R. Suarez, P. K. Nair, and P. V. Kamat, "Photoelectrochemical Behavior of Bi 2 S 3 Nanoclusters and Nanostructured Thin Films," *Langmuir*, vol. 14, pp. 3236–3241, June 1998.

[56] G. Konstantatos, L. Levina, J. Tang, and E. H. Sargent, "Sensitive solution-processed Bi2S3 nanocrystalline photodetectors," *Nano letters*, vol. 8, pp. 4002–6, Nov. 2008.

[57] A. K. Rath, M. Bernechea, L. Martinez, and G. Konstantatos, "Solution-Processed Heterojunction Solar Cells Based on p-type PbS Quantum Dots and n-type Bi2S3 Nanocrystals," *Advanced Materials*, vol. 23, pp. 3712–3717, July 2011.

[58] J. Tang, L. Brzozowski, D. A. R. Barkhouse, X. Wang, R. Debnath, R. Wolowiec, E. Palmiano, L. Levina, A. G. Pattantyus-Abraham, D. Jamakosmanovic, and E. H. Sargent, "Quantum dot photovoltaics in the extreme quantum confinement regime: the surface-chemical origins of exceptional air- and light-stability," *ACS nano*, vol. 4, pp. 869–78, Feb. 2010.

[59] A. H. Ip, S. M. Thon, S. Hoogland, O. Voznyy, D. Zhitomirsky, R. Debnath, L. Levina, L. R. Rollny, G. H. Carey, A. Fischer, K. W. Kemp, I. J. Kramer, Z. Ning, A. J. Labelle, K. W. Chou, A. Amassian, and E. H. Sargent, "Hybrid passivated colloidal quantum dot solids," *Nature Nanotechnology*, pp. 1–6, July 2012.

[60] D. Zhitomirsky, M. Furukawa, J. Tang, P. Stadler, S. Hoogland, O. Voznyy, H. Liu, and E. H. Sargent, "N-Type Colloidal-Quantum-Dot Solids for Photovoltaics," *Advanced Materials*, vol. 24, pp. 6181–6185, Sept. 2012.

[61] D. A. R. Barkhouse, A. G. Pattantyus-Abraham, L. Levina, and E. H. Sargent, "Thiols passivate recombination centers in colloidal quantum dots leading to enhanced photovoltaic device efficiency.," *ACS nano*, vol. 2, pp. 2356–2362, Nov. 2008.

[62] M. S. Kang, A. Sahu, C. D. Frisbie, and D. J. Norris, "Influence of Silver Doping on Electron Transport in Thin Films of PbSe Nanocrystals," *Advanced Materials*, vol. 25, pp. 725–31, Feb. 2013.

[63] Y. Yi, J. E. Lyon, M. M. Beerbom, and R. Schlaf, "Characterization of indium tin oxide surfaces and interfaces using low intensity x-ray photoemission spectroscopy," *Journal of Applied Physics*, vol. 100, no. 9, p. 093719, 2006.

[64] A. K. Rath, M. Bernechea, L. Martinez, F. P. G. de Arquer, J. Osmond, and G. Konstantatos, "Solution-processed inorganic bulk nanoheterojunctions and their application to solar cells," *Nature Photonics*, vol. 6, no. August, pp. 529–534, 2012.

[65] G. Konstantatos and E. H. Sargent, "Nanostructured materials for photon detection," *Nature nanotechnology*, pp. 1–10, May 2010.

[66] B. R. Saunders and M. L. Turner, "Nanoparticle-polymer photovoltaic cells," *Advances in colloid and interface science*, vol. 138, pp. 1–23, Apr. 2008.

[67] G. Yu, J. Gao, J. Hummelen, F. Wudl, and A. J. Heeger, "Polymer photovoltaic cells: enhanced efficiencies via a network of internal donor-acceptor heterojunctions," *Science*, vol. 270, no. 5243, p. 1789, 1995.

[68] C. Winder and N. S. Sariciftci, "Low bandgap polymers for photon harvesting in bulk heterojunction solar cells," *Journal of Materials Chemistry*, vol. 14, no. 7, p. 1077, 2004.

[69] J. Hou, H.-Y. Chen, S. Zhang, R. I. Chen, Y. Yang, Y. Wu, and G. Li, "Synthesis of a low band gap polymer and its application in highly efficient polymer solar cells," *Journal of the American Chemical Society*, vol. 131, pp. 15586–7, Nov. 2009.

[70] D. H. Wang, K. H. Park, J. H. Seo, J. Seifter, J. H. Jeon, J. K. Kim, J. H. Park, O. O. Park, and A. J. Heeger, "Enhanced Power Conversion Efficiency in PCDTBT/PC70BM Bulk Heterojunction Photovoltaic Devices with Embedded Silver Nanoparticle Clusters," *Advanced Energy Materials*, vol. 1, pp. 766–770, Oct. 2011.

[71] S. Fabiano, Z. Chen, S. Vahedi, A. Facchetti, B. Pignataro, and M. a. Loi, "Role of photoactive layer morphology in high fill factor all-polymer bulk heterojunction solar cells," *Journal of Materials Chemistry*, vol. 21, no. 16, p. 5891, 2011.

[72] A. J. Moulé, L. Chang, C. Thambidurai, R. Vidu, and P. Stroeve, "Hybrid solar cells: basic principles and the role of ligands," *Journal of Materials Chemistry*, vol. 22, pp. 2351–2368, 2012.

[73] W. U. Huynh, J. J. Dittmer, and A. P. Alivisatos, "Hybrid nanorod-polymer solar cells," *Science*, vol. 295, pp. 2425–7, Mar. 2002.

[74] D. Milliron, I. Gur, and A. P. Alivisatos, "Hybrid organic-nanocrystal solar cells," *MRS bulletin*, vol. 30, no. 1, pp. 41–44, 2005.

[75] S. Ren, L.-Y. Chang, S.-K. Lim, J. Zhao, M. Smith, N. Zhao, V. Bulovic, M. G. Bawendi, and S. Gradecak, "Inorganic-Organic Hybrid Solar Cell: Bridging Quantum Dots to Conjugated Polymer Nanowires," *Nano letters*, vol. 11, pp. 3998–4002, Sept. 2011.

[76] R. Steim, F. R. Kogler, and C. J. Brabec, "Interface materials for organic solar cells," *Journal of Materials Chemistry*, vol. 20, no. 13, p. 2499, 2010.

[77] J. Seo, M. Cho, D. Lee, A. N. Cartwright, and P. N. Prasad, "Efficient heterojunction photovoltaic cell utilizing nanocomposites of lead sulfide nanocrystals and a low-bandgap polymer," *Advanced Materials*, vol. 23, pp. 3984–3988, July 2011.

[78] Q. Guo, H. W. Hillhouse, and R. Agrawal, "Synthesis of Cu2ZnSnS4 nanocrystal ink and its use for solar cells," *Journal of the American Chemical Society*, vol. 131, pp. 11672–3, Aug. 2009.

[79] L.-I. Hung, C.-K. Tsung, W. Huang, and P. Yang, "Room-temperature formation of hollow Cu(2)O nanoparticles.," *Advanced Materials*, vol. 22, pp. 1910–14, May 2010.

[80] J.-F. Lin, G.-Y. Tu, C.-C. Ho, C.-Y. Chang, W.-C. Yen, S.-H. Hsu, Y.-F. Chen, and W.-F. Su, "Molecular structure effect of pyridine-based surface ligand on the performance of P3HT:TiO2 hybrid solar cell.," *Applied materials & interfaces*, vol. 5, pp. 1009–16, Feb. 2013.

[81] A. C. Arango, L. R. Johnson, V. N. Bliznyuk, Z. Schlesinger, S. A. Carter, and H. H. Hörhold, "Efficient titanium oxide/conjugated polymer photovoltaics for solar energy conversion," *Advanced Materials*, vol. 12, no. 22, pp. 1689–1692, 2000.

[82] J. Liu, E. N. Kadnikova, Y. Liu, M. D. McGehee, and J. M. J. Fréchet, "Polythiophene containing thermally removable solubilizing groups enhances the interface and the performance of polymer-titania hybrid solar cells," *Journal of the American Chemical Society*, vol. 126, pp. 9486–9487, Aug. 2004.

[83] K. M. Coakley and M. D. McGehee, "Photovoltaic cells made from conjugated polymers infiltrated into mesoporous titania," *Applied Physics Letters*, vol. 83, no. 16, pp. 3380–3382, 2003.

[84] L. Baeten, B. Conings, H.-G. Boyen, J. D'Haen, A. Hardy, M. D'Olieslaeger, J. V. Manca, and M. K. Van Bael, "Towards Efficient

Hybrid Solar Cells Based on Fully Polymer Infiltrated ZnO Nanorod Arrays," *Advanced Materials*, vol. 23, pp. 2802–5, July 2011.

[85] V. D. Mihailetchi, J. Wildeman, and P. W. Blom, "Space-Charge Limited Photocurrent," *Physical Review Letters*, vol. 94, pp. 1–4, Apr. 2005.

[86] M. M. Mandoc, W. Veurman, L. J. A. Koster, B. de Boer, and P. W. Blom, "Origin of the Reduced Fill Factor and Photocurrent in MDMO-PPV:PCNEPV All-Polymer Solar Cells," *Advanced Functional Materials*, vol. 17, pp. 2167–2173, Sept. 2007.

[87] Y. Liu, M. Gibbs, J. Puthussery, S. Gaik, R. Ihly, H. W. Hillhouse, and M. Law, "Dependence of carrier mobility on nanocrystal size and ligand length in PbSe nanocrystal solids," *Nano letters*, vol. 10, pp. 1960–1969, Apr. 2010.

[88] C. J. Brabec, A. Cravino, D. Meissner, N. S. Sariciftci, T. Fromherz, M. T. Rispens, L. Sanchez, and J. Hummelen, "Origin of the Open Circuit Voltage of Plastic Solar Cells," *Advanced Functional Materials*, vol. 11, pp. 374–380, Oct. 2001.

[89] Y. Liang, Z. Xu, J. Xia, S.-T. Tsai, Y. Wu, G. Li, C. Ray, and L. Yu, "For the bright future-bulk heterojunction polymer solar cells with power conversion efficiency of 7.4%," *Advanced Materials*, vol. 22, pp. E135–8, May 2010.

[90] D. H. Wang, J. S. Moon, J. Seifter, J. Jo, J. H. Park, O. O. Park, and A. J. Heeger, "Sequential Processing: Control of Nanomorphology in Bulk Heterojunction Solar Cells," *Nano letters*, July 2011.

[91] T. Wang, A. J. Pearson, A. D. F. Dunbar, P. a. Staniec, D. C. Watters, H. Yi, A. J. Ryan, R. a. L. Jones, A. Iraqi, and D. G. Lidzey, "Correlating Structure with Function in Thermally Annealed PCDTBT:PC70BM Photovoltaic Blends," *Advanced Functional Materials*, vol. 22, pp. 1399–1408, Apr. 2012.

[92] S. Dayal, N. Kopidakis, D. C. Olson, D. S. Ginley, and G. Rumbles, "Photovoltaic devices with a low band gap polymer and CdSe nanostructures exceeding 3% efficiency," *Nano letters*, vol. 10, pp. 239–42, Jan. 2010.

[93] E. T. Hoke, K. Vandewal, J. a. Bartelt, W. R. Mateker, J. D. Douglas, R. Noriega, K. R. Graham, J. M. J. Fréchet, A. Salleo, and M. D. McGehee, "Recombination in Polymer:Fullerene Solar Cells with Open-Circuit Voltages Approaching and Exceeding 1.0 V," *Advanced Energy Materials*, vol. 3, pp. 220–230, Feb. 2013.

[94] K. M. Coakley, L. Yuxiang, C. Goh, and M. D. McGehee, "Ordered organic-inorganic bulk heterojunction photovoltaic cells," *MRS bulletin*, vol. 30, no. 1, pp. 37–40, 2005.

[95] J. Liu, T. Tanaka, K. Sivula, A. P. Alivisatos, and J. M. J. Fréchet, "Employing end-functional polythiophene to control the morphology of nanocrystal-polymer composites in hybrid solar cells," *Journal of the American Chemical Society*, vol. 126, pp. 6550–1, June 2004.

[96] S. D. Oosterhout, L. J. A. Koster, S. S. van Bavel, J. Loos, O. Stenzel, R. Thiedmann, V. Schmidt, B. Campo, T. J. Cleij, L. Lutzen, D. Vanderzande, M. M. Wienk, and R. a. J. Janssen, "Controlling the Morphology and Efficiency of Hybrid ZnO:Polythiophene Solar Cells Via Side Chain Functionalization," *Advanced Energy Materials*, vol. 1, pp. 90–96, Jan. 2011.

[97] L. Zhao and Z. Lin, "Crafting semiconductor organic-inorganic nanocomposites via placing conjugated polymers in intimate contact with nanocrystals for hybrid solar cells," *Advanced Materials*, vol. 24, pp. 4353–68, Aug. 2012.

[98] M. C. Iovu, E. E. Sheina, R. R. Gil, and R. D. McCullough, "Experimental Evidence for the Quasi-Living Nature of the Grignard Metathesis Method for the Synthesis of Regioregular Poly(3-alkylthiophenes)," *Macromolecules*, vol. 38, pp. 8649–8656, Oct. 2005.

[99] R. Miyakoshi, A. Yokoyama, and T. Yokozawa, "Catalyst-Transfer Polycondensation . Mechanism of Ni-Catalyzed Chain-Growth Polymerization Leading to Well-Defined Poly(3-hexylthiophene)," *Journal of the American Chemical Society*, vol. 127, no. 6, pp. 17542–17547, 2005.

[100] W. C. Tsoi, S. J. Spencer, L. Yang, A. M. Ballantyne, P. G. Nicholson, A. Turnbull, A. G. Shard, C. E. Murphy, D. D. C. Bradley, J. Nelson, and J.-S. Kim, "Effect of Crystallization on the Electronic Energy Levels and Thin Film Morphology of P3HT:PCBM Blends," *Macromolecules*, vol. 44, pp. 2944–2952, Apr. 2011.

[101] M. J. Greaney, S. Das, D. H. Webber, S. E. Bradforth, and R. L. Brutchey, "Improving open circuit potential in hybrid P3HT:CdSe bulk heterojunction solar cells via colloidal tert-butylthiol ligand exchange.," *ACS nano*, vol. 6, pp. 4222–30, May 2012.

[102] J. Veres, S. Ogier, G. Lloyd, and D. de Leeuw, "Gate Insulators in Organic Field-Effect Transistors," *Chemistry of Materials*, vol. 16, pp. 4543–4555, Nov. 2004.

[103] S. Miyanishi, Y. Zhang, K. Hashimoto, and K. Tajima, "Controlled Synthesis of Fullerene-Attached Poly(3-alkylthiophene)- Based Copolymers for Rational Morphological Design in Polymer Photovoltaic Devices," *Macromolecules*, vol. 45, pp. 6424–6437, 2012.

[104] M. a. Ruderer, S. Guo, R. Meier, H.-Y. Chiang, V. Körstgens, J. Wiedersich, J. Perlich, S. V. Roth, and P. Müller-Buschbaum, "Solvent-Induced Morphology in Polymer-Based Systems for Organic Photovoltaics," *Advanced Functional Materials*, pp. n/a–n/a, July 2011.

[105] G. Itskos, A. Othonos, T. Rauch, S. F. Tedde, O. Hayden, M. V. Kovalenko, W. Heiss, and S. a. Choulis, "Optical Properties of Organic Semiconductor Blends with Near-Infrared Quantum-Dot Sensitizers for Light Harvesting Applications," *Advanced Energy Materials*, pp. 802–812, June 2011.

[106] N. Bansal, F. T. F. O'Mahony, T. Lutz, and S. a. Haque, "Solution Processed Polymer-Inorganic Semiconductor Solar Cells Employing Sb2 S3 as a Light Harvesting and Electron Transporting Material," *Advanced Energy Materials*, vol. 3, pp. 986–990, Aug. 2013.

[107] M. Panthani, V. Akhavan, B. Goodfellow, J. Schmidtke, L. Dunn, A. Dodabalapur, P. Barbara, and B. A. Korgel, "Synthesis of CuInS2, CuInSe2, and Cu(InxGa1-x)Se2 (CIGS) Nanocrystal Inks for Printable Photovoltaics," *Journal of the American Chemical Society*, vol. 130, no. 49, pp. 16770–16777, 2008.

[108] W. Ma, S. L. Swisher, T. Ewers, J. Engel, V. E. Ferry, H. a. Atwater, and a. P. Alivisatos, "Photovoltaic Performance of Ultrasmall PbSe Quantum Dots.," *ACS nano*, Oct. 2011.

[109] P. Maraghechi, A. J. Labelle, A. R. Kirmani, X. Lan, M. M. Adachi, S. M. Thon, S. Hoogland, A. Lee, Z. Ning, A. Fischer, A. Amassian, and E. H. Sargent, "The donor-supply electrode enhances performance in colloidal quantum dot solar cells.," *ACS nano*, vol. 7, pp. 6111–6, July 2013.

[110] I. Gur, N. A. Fromer, M. L. Geier, and A. P. Alivisatos, "Air-stable all-inorganic nanocrystal solar cells processed from solution.," *Science*, vol. 310, pp. 462–5, Oct. 2005.

[111] X. Wang, G. I. Koleilat, J. Tang, H. Liu, I. J. Kramer, R. Debnath, L. Brzozowski, D. A. R. Barkhouse, L. Levina, S. Hoogland, and E. H. Sargent, "Tandem colloidal quantum dot solar cells employing a graded recombination layer," *Nature Photonics*, no. June, 2011.

[112] D. A. R. Barkhouse, R. Debnath, I. J. Kramer, D. Zhitomirsky, A. G. Pattantyus-Abraham, L. Levina, L. Etgar, M. Gratzel, and E. H. Sargent, "Depleted Bulk Heterojunction Colloidal Quantum Dot Photovoltaics.," *Advanced Materials*, pp. 1–5, May 2011.

[113] N. Zhao, T. P. Osedach, L.-Y. Chang, S. M. Geyer, D. Wanger, M. T. Binda, A. C. Arango, M. G. Bawendi, and V. Bulovic, "Colloidal PbS quantum dot solar cells with high fill factor.," *ACS nano*, vol. 4, pp. 3743–3752, July 2010.

[114] E. Kucur, J. Riegler, G. a. Urban, and T. Nann, "Determination of quantum confinement in CdSe nanocrystals by cyclic voltammetry," *The Journal of Chemical Physics*, vol. 119, no. 4, p. 2333, 2003.

[115] R. Miyakoshi, A. Yokoyama, and T. Yokozawa, "Synthesis of Poly(3-hexylthiophene) with a Narrower Polydispersity," *Macromolecular Rapid Communications*, vol. 25, pp. 1663–1666, Oct. 2004.

[116] L. Zhai, R. L. Pilston, K. L. Zaiger, K. K. Stokes, and R. D. McCullough, "A simple method to generate side-chain derivatives of regioregular polythiophene via the GRIM metathesis and post-polymerization functionalization," *Macromolecules*, vol. 36, pp. 61–64, 2003.